COSMIC RAY MUON RADIOGRAPHY

by

LARRY JOE SCHULTZ

A dissertation submitted in partial fulfillment of the
requirements for the degree of

DOCTOR OF PHILOSOPHY
in
ELECTRICAL AND COMPUTER ENGINEERING

Portland State University
2003

ACKNOWLEDGMENTS

This dissertation could not have been completed without the kind support of many people throughout my midlife return to graduate school. My first note of thanks goes to my brother Roger Schultz who beat me to the punch in returning for a PhD and in so doing gave me the confidence that I could do it too.

Doug Hall saw me wandering in the PCAT hallways at Portland State University and showed me what I needed to do to get started in graduate school. Doug provided lots of early guidance, a job, and some of the best teaching I ever experienced at a university level and I'm grateful for all of that.

George Lendaris inspired my interest in computational intelligence and provided me with the opportunity to get my feet wet in research. Although our research interests later diverged, George has remained a good friend and mentor and has strongly influenced my approach to problem solving.

I encountered a few big bumps in the road along my path, and there were moments when I doubted my ability to stay the course. Tad Shannon took the time to listen and always seemed to find the right words to restore my confidence. Tad also taught me a lot of mathematics and reviewed some of the mathematical developments in this dissertation. I'm thankful to Tad on several levels.

Kevin Vixie was instrumental in bringing me to Los Alamos National Laboratory and so enabled me to pursue this dissertation work. I am very appreciative of Kevin's selfless assistance.

Thanks of course go to my colleagues on Muon Radiography team at Los Alamos, both for their contributions to the work and for allowing me to pursue significant portions individually for my dissertation. Thanks to Andy Saunders, John Gomez, Margaret Teasdale, Jason Medina, Bill Priedhorsky, Konstantin Borozdin, Gary Hogan, and Richard Schirato. Special thanks to Gary Hogan for his assistance with data acquisition for the experiment. Tom Asaki provided an invaluable service in helping with coding for tracing of ray paths through pixels and voxels.

Thanks to my entire dissertation committee, and very special thanks go to my two major advisors on this project, Andy Fraser of PSU and Chris Morris of LANL. Both provided intellectual guidance without which the project would never have been finished. Thanks to Andy for his diligence in reviewing the details and guiding the development of the reconstruction work and for helping me navigate the bureaucratic maze. I am eternally grateful to Chris Morris for providing me with the opportunity to do this work, and for his unwavering advocacy throughout the effort.

Thanks to Los Alamos National Laboratory and the Department of Energy for providing me with monetary support during this work.

My parents, R.D. and Emma Schultz, have spent most of their working lives in support of public education at all levels. They passed their belief in the value of education on to me, and, more importantly, gave me their personal love and support

throughout my educational process and life in general. My father and mother in law, Bill and JoAnn McCool, have also been particularly interested in and supportive of my doctoral work and never once called me a deadbeat husband when their daughter was putting me through school!

And finally, my most significant thanks to wife, Robyn, and sons Connor and Caleb for their loving support and patience throughout the hours, days, weeks, and months of work required to get this done. They'll be happy to have Dad back, and Dad will be even happier to be back.

TABLE OF CONTENTS

Page

LIST OF TABLES

LIST OF FIGURES

CHAPTER 1
INTRODUCTION

1.1 Information from the Heavens

When cosmic rays strike the Earth's atmosphere, a cascade of many types of subatomic particles is created. By the time this shower of particles reaches the Earth's surface, it is comprised primarily of *muons*. Muons are charged particles, having about 200 times the mass of electrons (indeed, muons may be thought of as "heavy electrons," though they may be positively or negatively charged). The surface of the Earth is bombarded continuously by these muons at a rate of about 10,000 muons per minute per square meter [1]. Most cosmic ray muons have sufficient energy to penetrate meters of rock. One might think of this as "invisible rain," constantly showering down from the sky, passing unnoticed through objects and life forms into the ground, to be eventually absorbed by the Earth.

Are these cosmic ray muons of any practical use? They represent no substantial source of energy. They perform no usable "work" as they pass through objects. However, since muons are charged particles, they are easily detectable through means used by subatomic physicists for decades. Muons are detected by capturing and amplifying the small deposition of energy that occurs when they pass through instruments. The deposited energy is given up by the particle. Muons, then, are detectable and experience changes as they pass though material. Indeed, as will be

discussed later, other interactions occur as muons pass through matter, and the magnitudes of these changes are related to properties of the material itself.

Although cosmic ray muons were metaphorically referred to in terms of "rain," muons actually arrive not strictly from vertically overhead, but from angles covering the upper hemisphere (though preferentially from overhead, and quite sparsely from angles nearing horizontal). Since cosmic ray muons are detectable, carry information as they pass through material, and continuously bombard any position on the Earth's surface from many overhead directions, one might wonder: Could these cosmic ray muons be used as some sort of 3D probe? In other words, could one use the cosmic ray muon flux to probe an object of unknown structure / material composition to enhance our knowledge about that object, as illustrated in Figure 1.1?

Such a probe using cosmic ray muons would have some attractive features. Foremost would be that no additional radiological dose would be applied to the object. Whether or not we mine the information, the object will be illuminated with cosmic ray muons. This is a key advantage over x-ray radiography, for instance, wherein an object receives a radiological dose that must be carefully managed to avoid undesirable effects, particularly if the object is a living being. Of course a related additional attractive feature of using cosmic ray muons is that no manufactured radiographic source is required (in a sense, one gets "something for nothing"). Another potential feature of a cosmic ray muon probe is that, since muons are so highly penetrating, very thick, dense objects could be examined.

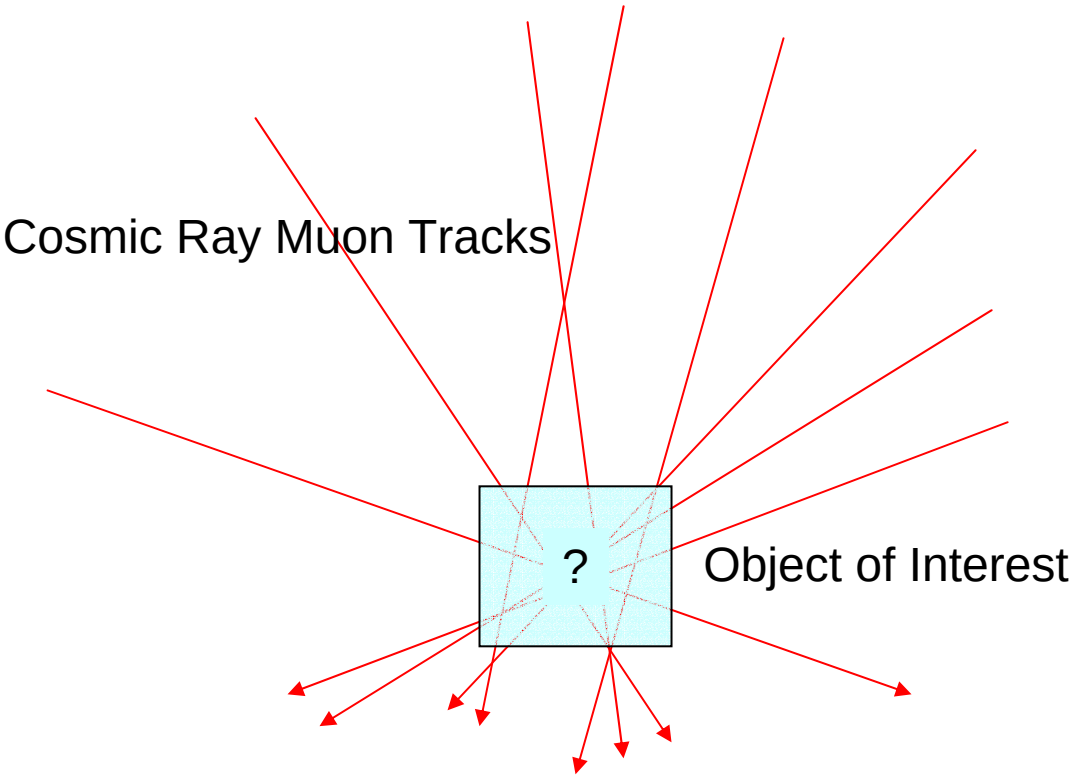

Figure 1.1 Illustration of cosmic ray muons passing through an object. Measuring changes induced in the muons during this passage could reveal information about the object.

1.2 A New Form of Radiography

In 2001 Christopher Morris and William Priedhorsky of Los Alamos National Laboratory (LANL) considered a novel form of radiography. Their idea was to make use of the multiple Coulomb scattering[1] experienced by cosmic ray muons passing through objects to segregate materials of high and low atomic density. Morris and Priedhorsky put together a small team of researchers at LANL, including the author. The goal of this team was to provide proof of principle for cosmic ray muon radiography. To achieve this goal the team outlined four primary objectives:

[1] Multiple Coulomb Scattering (MCS) is one of the interactions that occur when charged particles move through matter. MCS will be discussed in detail in Sections 2.2.3 and 3.2.

- Build a small prototype and gather experimental data.
- Implement a Monte Carlo simulation of the experiment.
- Develop an object reconstruction algorithm.
- Produce reconstructions of experimental data (to prove the concept) and simulated data (to validate understanding).

By 2003 these objectives were achieved, as documented in [2]. A new form of radiography was introduced – never before had radiographs of small objects been made using passive cosmic ray muons[2]. A significant amount of press attention followed, and cosmic ray muon radiography was featured in *Physics Today* [3], on National Public Radio [4], and several websites, including those of National Geographic [5], Science News [6], and the BBC.

1.3 The Author's Role and this Dissertation

Development of cosmic ray muon radiography continues. Though this development was and is the product of a team effort, some portions were the result of independent, individual work by the author. The author's intent to produce a doctoral dissertation was understood by the research team, so the following areas were left to the author to maintain intellectual integrity:

- Construction and execution of the experimental prototype.
- Development of a new 3D tomographic reconstruction algorithm based on the theory of multiple scattering.
- Development of mathematical framework whereby the process can be described.

[2] Imaging of large (mountain sized) objects using the differential attenuation of cosmic ray muons has been discussed in the literature, as will be detailed in Section 2.3.

This dissertation will be concerned primarily with those topics. Where supporting ideas or work are the products of the development team or individual collaborators these items will be credited by referencing publications of the team.

1.4 A Potential Application – Nuclear Contraband Detection

The major contributions of this dissertation will deal with the *methodological* aspects of cosmic ray muon radiography rather than applications. However, the LANL work was funded to address a special application, and proper perspective may be gained through introduction of that application.

The September, 2001 tragedy at the World Trade Center in New York dramatically heightened the nation's sensitivity to potential homeland threats. Undoubtedly the most frightening is the detonation of a nuclear device in a major city. The enormous consequence of such an event has motivated substantial effort into the development of strategies to prevent it. One such strategy is to improve the control of nuclear material at its source, and another is to increase the likelihood of detection of illegal transport of these materials at transportation checkpoints such as border crossings.

Weapons grade nuclear material is, of course, radioactive, but detection of the material via radiation detectors can be thwarted by a small amount of lead shielding [3]. Conventional x-rays are not sufficiently penetrating to reveal nuclear material within typical cargos without the use of very high energy rays that would pose health hazards [7]. Other potential detection methods exist, but none have the particular advantage of muon radiography: the lack of application of any artificial radiological dose to the subject. If proven feasible for this application, inspection of cars and

trucks could be performed without requiring operators and passengers to exit the vehicles.

1.5 Dissertation Outline

Chapter 2 presents background information on several pertinent topics. Cosmic ray muons, their formation in the atmosphere, and the muon flux at the Earth's surface are described. The physics of interaction of muons with material is summarized. Some relevant prior historical work is reviewed. Finally pertinent background on techniques for computed tomography is presented.

Details of our specific concept for cosmic ray muon radiography appear in Chapter 3. Multiple Coulomb scattering as an information source for radiography will be explored in more detail. The basic objective of Cosmic Ray Muon Radiography will be defined as the segregation of high, medium and low Z (atomic number) materials. The sensitivity of MCS to material Z will be established through some numerical examples.

In Chapter 4 the framework for tomographic reconstruction using the stochastic multiple scattering signal will be presented, contrasted with a standard tomographic framework for a deterministic information source. The first of two image reconstruction algorithms also appear in Chapter 4. The Point of Closest Approach (PoCA) algorithm was developed fairly early in this project as a means to produce reconstructions of experimental datasets, but the strengths and weaknesses of the algorithm will be first illustrated through simulated examples in Chapter 4. The experimental proof of principle will be discussed in Chapter 5, including reconstructions made using the PoCA algorithm.

In Chapter 6 a new tomographic algorithm, the Maximum Likelihood Scattering and Displacement (MLSD) Algorithm, will be presented. This algorithm is founded in traditional tomographic principles, but differs fundamentally from previous methods due to the stochastic nature of the cosmic ray muon radiography information source. The MLSD algorithm will be shown, via simulated results, to provide reconstructions quite superior to those obtainable with the PoCA algorithm.

The dissertation will conclude in Chapter 7 with a summary of the material presented. Supportive material will be delivered in several Appendices.

CHAPTER 2
BACKGROUND

This chapter introduces background information pertinent to the use of cosmic ray muons for radiography. Sections 2.1 introduces the muon, explains how these subatomic particles are created in the atmosphere from cosmic rays, and describes the flux of cosmic ray muons at the Earth's surface. Section 2.2 gives details on how muons interact when passing through material. This is followed by a review of some previous efforts to use cosmic ray muons as information probes in Section 2.3, and a discussion of some relevant research into radiography using other charged particles in Section 2.4. This chapter concludes in Section 2.5 with a review of the basics of computed tomography and a summary in Section 2.6.

2.1 Cosmic Rays & Muons

2.1.1 Primary Cosmic Rays and the Atmospheric Cascade

Although cosmic radiation is often thought to come from the sun, in truth cosmic radiation comes generally from outside the solar system [1]. Cosmic rays striking the Earth's atmosphere are hence composed primarily of stable particles and nuclei which survive the trip. When these "primary" cosmic rays strike the Earth's atmosphere, interactions take place which generate additional "secondary" particles. Interactions of these secondary particles create more particles, and a cascade of particles results.

It is beyond the scope of this document to dwell on the details of the nuclear physics involved in creating the secondary cosmic ray flux at the Earth's surface. However, the basics may be described in simple terms. An individual *proton* (p) or nucleus strikes the atmosphere and collisions with atmospheric nuclei release secondary particles known as *pions* (π). The primary proton loses energy via these collisions, but while it survives many pions may be produced. Pions may be positively or negatively charged or may be neutral. Charged pions decay quickly to like charged *muons* (μ). Neutral pions decay to gamma rays (γ), some of which produce electron (e^-) / positron (e^+) pairs which generally do not reach the surface. Muons lose energy as they pass through the atmosphere, and eventually decay to electrons or positrons, but most cosmic ray muons are sufficiently energetic to reach the surface. Figure 2.1a illustrates this cascade. Because muons do not interact hadronically and have a relatively longer lifetime than other charged particles generated in the cascade, they dominate the surface spectrum, as illustrated in Figure 2.1b. Muons have a rest mass of 105.7 MeV [1], about 200 times that of electrons, and are sometimes referred to as "heavy electrons." They have a mean life of 2.2 μs [1], and may be positively or negatively charged.

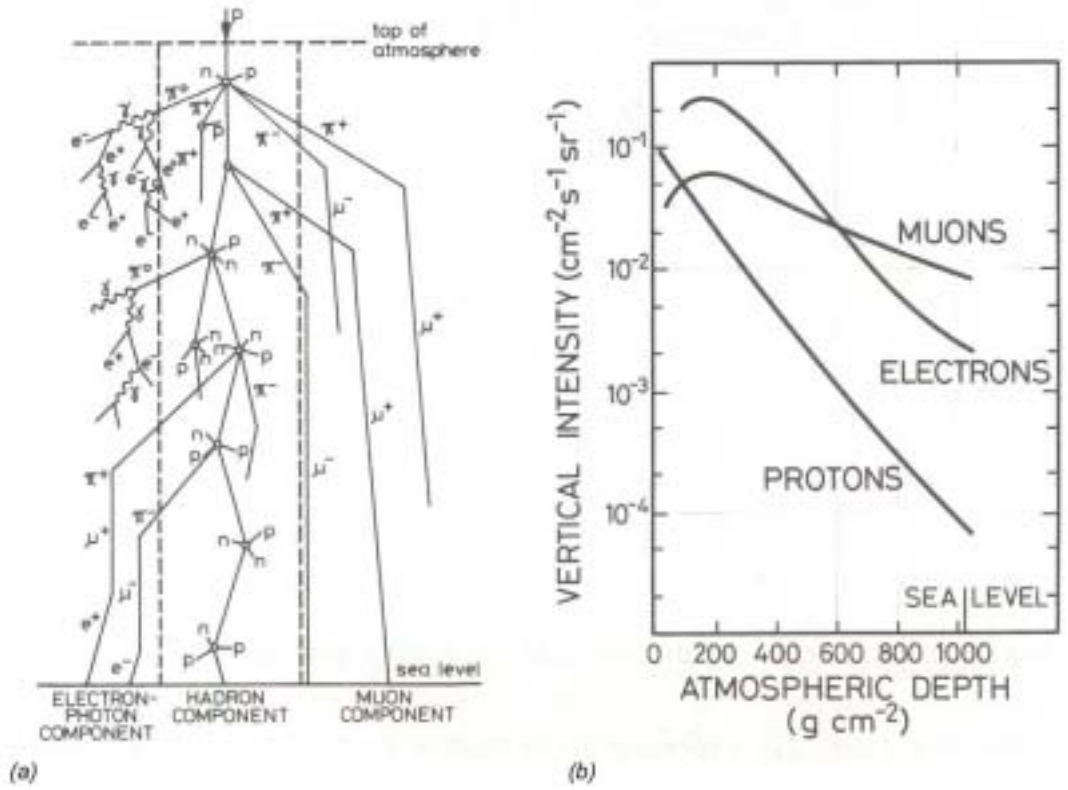

Figure 2.1 Illustration of the particle cascade produced in the atmosphere from a primary cosmic proton (a). Altitude variation of the main components in the cascade (b) (From [8], used with permission).

2.1.2 The Muon Spectrum at the Earth's Surface

Muons arrive at a point on the Earth's surface from angles spanning the upper hemisphere with a wide range of energies. The angle and energy distribution reflects a convolution of the production spectrum, energy loss in the atmosphere, and decay. The surface spectrum varies with altitude, geophysical location, and the level of solar activity (since solar activity can modulate the primary cosmic ray spectrum). Many researchers have experimentally documented the muon spectrum at various locations and altitudes and have modeled the production process ([9-13], for example).

Illustrative data taken from two experiments is shown in Figure 2.2, for arrival angles of near 0° and 75°. Analytical models such as that presented in [9], coupled

with such experimental data, have been used to develop "muon generators" for simulation purposes. Results from a model developed by Blanpied [14] are shown with the experimental data in Figure 2.2. More information about the Blanpied model may be found in Appendix A.

Experimentalists often refer to the following "rules of thumb" to describe the muon spectrum [1]:

- The energy (p) distribution is almost flat for energies below 1 GeV, and falls as $p^{-2.7}$ for energies above 10 GeV. The mean muon energy is 3-4 GeV.
- The flux is greatest at the zenith, and falls approximately as $\cos^2(\theta)$, where θ is plane angle from vertical.
- The overall muon rate is about 10,000 $m^{-2} \cdot min^{-1}$ for horizontal detectors, or about 1 particle through a fingernail sized area per minute.

It is important to note that the muon rate is low enough (about 160 Hz in a square meter detector) to enable single event processing, but will be shown to be high enough to provide information in a reasonable amount of time in a radiographic scenario.

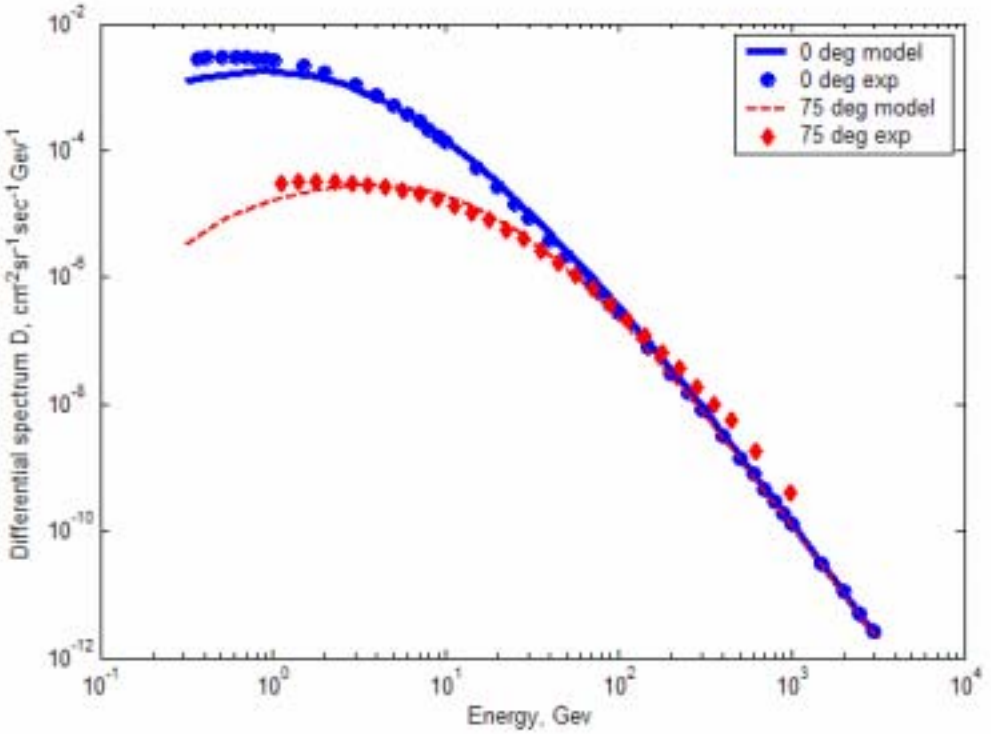

Figure 2.2 Experimental muon spectrum data for two arrival angles; 0° data taken from [11], 75 ° data from [10]. The model lines were generated from a model developed by Blanpied [14].

2.2 How Muons Interact with Matter

Muons in the .1-1000 GeV energy range interact with matter in two primary ways: energy loss through electromagnetic interaction with electrons resulting in ionization, and deflection via multiple Coulomb scattering from interactions with nuclei, as illustrated in Figure 2.3. Sufficient energy loss will cause a muon to stop, which is highlighted as a third "interaction". In the following three subsections each of these three interaction modes will be discussed.

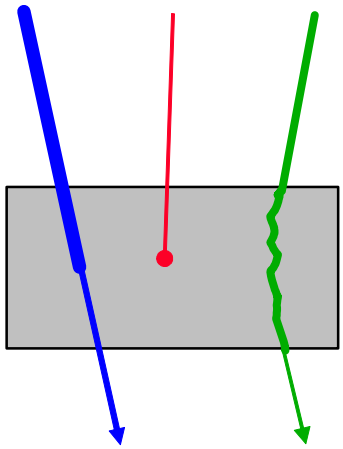

Figure 2.3 Muon interactions when passing through matter. Muons lose energy through ionization (left). If enough energy is lost, muons will stop (center). Muons are also deflected via multiple Coulomb scattering (right). These interactions are shown separately for clarity, although all three are applicable to any particle.

2.2.1 Energy Loss

As muons pass through material and collide with electrons, these electrons are (predominantly) ejected from the atom. The muon will lose energy equivalent to the ionization energy of the electrons with which it collides. For muons in the .1-1000 GeV energy range, about 2.2 MeV·of energy is lost per $g \cdot cm^{-2}$ of material traversed [1]. The energy loss of muons traversing 10 cm thicknesses of various materials is shown in Table 2.1.

Table 2.1 Approximate energy loss experienced by muons traversing 10 cm of various materials.

Material	Volume Density, $g \cdot cm^{-3}$ [1]	Areal Density of 10 cm depth, $g \cdot cm^{-2}$	Muon Energy Loss, MeV	% Energy Loss for 3 GeV Muon
Water	1.00	10.0	22.0	0.7%
Concrete	2.50	25.0	55.0	1.8%
Iron	7.87	78.7	173.1	5.8%
Lead	11.35	113.5	249.7	8.3%
Uranium	18.95	189.5	416.9	13.9%

Energy loss is a potential information source that could be tapped for radiography, since energy loss is proportional to the mass encountered by a particle traversing an object area. However, a means for the precise measurement of energy of incoming and outgoing particles would be required, and such a measurement may not be simply or economically obtained.

2.2.2 Range Out

If enough energy is lost through ionization, a muon will stop (range out) within the material. Precise calculation of the range of particles within materials involves integration of the energy loss relationship outside the energy range where the 2.2 MeV loss per $g \cdot cm^{-2}$ is appropriate, and the energy loss rate varies somewhat with material. However, we may approximate the range as the material depth at which all energy is lost, using the 2.2 $MeV \cdot cm^2 \cdot g^{-1}$ figure. Results are shown in Table 2.2 for the same materials as in Table 2.1, for various muon energies.

Table 2.2. Approximate range of muons in various materials.

Material	Volume Density, $g \cdot cm^{-3}$ [1]	Range (m) of Muons with Energy		
		0.3 GeV	3 GeV	30 GeV
H2O	1.00	1.4	13.6	136.4
Concrete	2.50	0.5	5.5	54.5
Iron	7.87	0.2	1.7	17.3
Lead	11.35	0.1	1.2	12.0
Uranium	18.95	0.1	0.7	7.2

Interesting to note is that muons at the mean energy (~3 GeV) will penetrate about a meter of even very dense materials, and high energy muons will penetrate tens of meters of rock or metal. Because the energy spectrum of cosmic ray muons is continuous and the average range is long, differential attenuation can be used to

radiograph large objects. Indeed previous researchers have performed attenuation radiography of large objects using cosmic ray muons (see Section 2.3). If the objective is to radiograph small objects, however, very few muons will range out regardless of material composition. For instance, of the 10 cm cubes discussed in the previous section, only the uranium cube would stop muons with 0.3 GeV energy, and the mean energy of cosmic ray muons is ten times that. Hence differential attenuation is not an appropriate information source for small objects.

2.2.3 Multiple Coulomb Scattering (MCS)

A muon (or any charged particle) passing through a material is deflected by many small angle scatters off of the nuclei of the material. As illustrated two dimensionally in Figure 2.4, a particle traverses the material in a stochastic path due to these multiple scatters. The particle emerges from the material at an aggregate scattered angle θ and displaced from the un-scattered exit point by a distance x. The angular scattering distribution may be approximated as Gaussian[3],

$$f_\theta(\theta) \cong \frac{1}{\sqrt{2\pi}\sigma_\theta} \exp\left(-\frac{\theta^2}{2\sigma_\theta^{\,2}}\right) \tag{2.1}$$

with zero mean and a standard deviation given by [15]:

$$\sigma_\theta \cong \frac{15}{\beta c p}\sqrt{\frac{L}{L_{rad}}} \tag{2.2}$$

where p and βc, are the momentum (in MeV/c) and velocity of the incident particle, L is the depth of the material, and L_{rad} is the radiation length of the material.

[3] The theory of MCS and a discussion of the Gaussian approximation appear in Section 3.2.

Radiation length is a characteristic amount of matter for electromagnetic interactions, and generally decreases with increasing material Z number. Table 2.3 shows how the width of the scattering distribution changes for muons passing through 10 cm of the Table 2.1 materials.

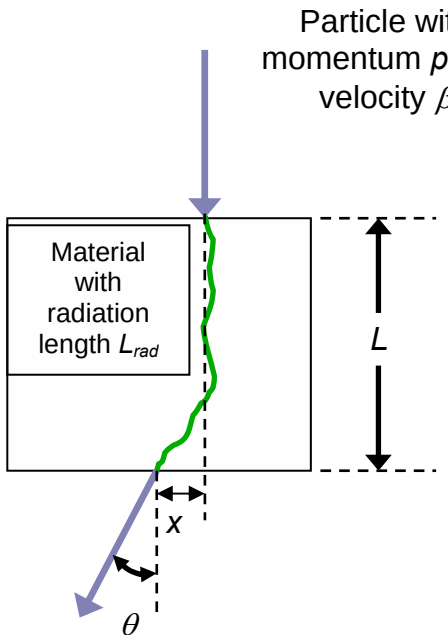

Figure 2.4 Multiple Coulomb scattering of a charged particle through material. The magnitude of scattering is exaggerated for illustrative purposes.

Table 2.3 Approximate multiple scattering for muons passing through 10 cm of various materials.

Material	Radiation Length, cm [1]	RMS Scattering (milliradians) expected for Muons with Energy:		
		0.3 GeV	3 GeV	30 GeV
Water	36.1	26.3	2.6	0.3
Concrete	10.7	48.3	4.8	0.5
Iron	1.76	119.2	11.9	1.2
Lead	0.56	211.3	21.1	2.1
Uranium	0.32	279.5	28.0	2.8

MCS represents an information source that is almost as sensitive to material Z as energy loss. Moreover, the measurement of muon scattering with milliradians

precision (by measuring particle position to millimeter level precision) is much more easily accomplished than measurement of particle energy to a few percent (requiring the generation of magnetic fields for spectroscopy). It is the MCS signal that is used for cosmic ray muon radiography herein, as will be described in Chapter 3.

2.3 Previous Work on Cosmic Ray Muon Radiography

Several researchers have investigated the use of cosmic ray differential attenuation or range radiography for large archaeological or geological objects. E. P. George made the first such effort in 1955 [16]. George measured the depth of rock above an underground tunnel by making use of the attenuation of the cosmic ray flux. He measured the cosmic ray flux inside the tunnel and the incident flux outside the tunnel and inferred the rock depth from the ratio of these signals. Luis Alvarez followed George's work with his radiography of the Pyramid of Chepren at Giza, Egypt in the late 1960's [17]. The Pyramids of Cheops (Chepren's father) and Sneferu (his grandfather) were known to contain interior chambers at similar locations. It had been speculated that Chepren's Pyramid might also contain such interior chambers, but they had not been discovered. Alvarez and his colleagues sought to locate (or disprove the existence of) these chambers by measuring the differential attenuation of the cosmic ray flux through Chepren's Pyramid. Alvarez and his colleagues placed muon counters in an existing underground chamber beneath the pyramids. As they measured the count rate at various angles, they experienced higher count rates when pointing at the faces of the pyramid than when pointing at the corners since the path length of cosmic rays passing through the corners was longer. The position of their underground chamber was not centered beneath the pyramid, and they were also able

to see count rate differences when pointing at opposite faces that were proportional to that deviation from center position. Armed with this confirmation of their method, they searched for hidden chambers and concluded that there were none.

In subsequent years other researchers have followed Alvarez and used cosmic ray attenuation to make measurements on large objects. Minato [18] produced a rough radiograph of the Higashi-Honganji Temple gate in Nagoya, Japan, using a simple hand held muon counter to measure flux attenuation. Nagamine [19] measured the internal structure of Mt. Tsukaba and Mt. Asama using cosmic ray attenuation with the goal of volcanic eruption prediction. In this case large angle (nearly horizontal) muons were required, since detectors were located 2 km to the side of the volcanoes, rather than beneath them, of course.

These interesting experiments, and others like them, relied on attenuation of the cosmic ray muon flux passing through meters of dense material. The MCS based radiography described herein, applied to much smaller, less dense objects, is fundamentally different, as will be seen.

A recent novel use of cosmic ray muons has been described by Frlez, et. al [20]. Their objective was to map the efficiency of cesium iodide crystals used for calorimetry. Cosmic ray muons were used as a freely available probe to measure the efficiency of the crystals. Muon detectors were arranged above and below a chamber containing several of the CsI crystals, and rays were tracked through the chambers / crystals. For cosmic rays passing through a crystal, the path length and resultant expected energy deposition were calculated. Hence, the response of the CsI crystals to

that energy deposition could be analyzed. Though this application was quite different from that discussed herein, the particle detection and data acquisition system used in this effort was very similar to the experimental prototype that will be discussed in Chapter 5.

In summary, cosmic ray muons have been used in the past as radiographic probes, but no previous attempt has been made to use the multiple scattering of cosmic ray muons through material as an information source.

2.4 Previous Work on Charged Particle Radiography

Multiple scattering of charged particles as a radiographic information source has been proven through *proton radiography* (pRAD) [21]. pRAD was invented at Los Alamos National Laboratory in 1995 and is currently used routinely for radiography of moderately dense objects that are difficult to image with x-rays. pRAD is performed using an 800 MeV energy proton beam from a linear accelerator. A schematic is shown in Figure 2.5.

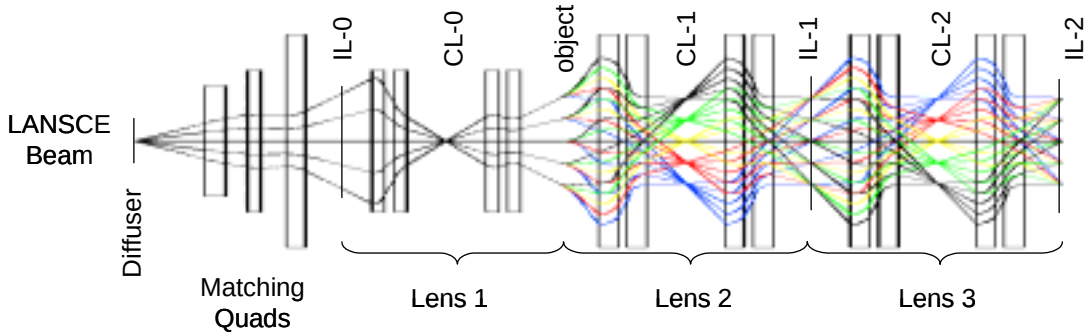

Figure 2.5 Schematic of proton radiography beam line (courtesy Los Alamos National Laboratory, used with permission).

Simply put, pRAD works by illuminating an object (labeled object in Figure 2.5) with a proton beam, producing multiple scattering. The angular distribution of the

proton beam exiting the object is then locally (spatially) correlated with the projected density of the material through which the beam passed. A clever arrangement of magnetic lenses transforms particle angle to radial position at the collimator (CL-1) location. At the collimator location, particles with large scattering angle are attenuated. For example, the black and blue rays might be removed. Another magnetic lens re-transforms the particles back to the spatial coordinates at the image plane (IL-1). So at the image plane, areas where the object induced high scattering are less populated with protons due to the collimation. A proton to light converter and CCD cameras produce an image. The pRAD system is often used to image dynamic events, with multiple images taken via proton pulses spaced closely in time. Additional collimator (CL-2) and imaging stations (IL-2) downstream provide for more image frames in such a dynamic sequence or for enhanced information if a different angle cut is used in the second collimator. Sample pRAD images are shown in Figure 2.6. pRAD imaging is based on large number statistics rather than the analysis of single events, and relies on a linear accelerator rather than a passive source. However, the pRAD method is pertinent to the consideration of cosmic ray muon radiography in that it provides proof of the feasibility of multiple scattering as a radiographic information source.

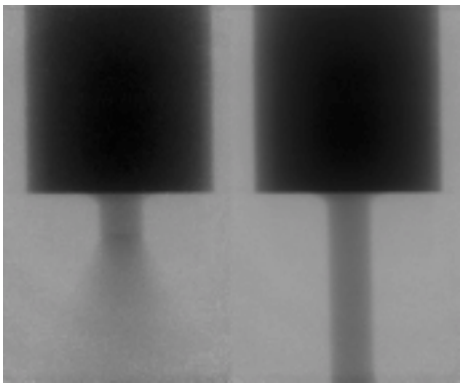

Figure 2.6 Sample images created via multiple scattering proton radiography (pRAD) (courtesy Los Alamos National Laboratory, used with permission). The darker areas represent higher Z material.

Charpak, et al. [22] used *nuclear (hadronic) scattering* of protons passing through material as an information source for radiography. They used protons generated by an accelerator and detected particles scattered via hadronic interactions. By tracing incoming and outgoing trajectories to an intersection point they identified the point of scatter within an object volume, and used the information gathered from many scattered particles to reconstruct object density. Muons have no hadronic interaction, so this work is not directly pertinent to cosmic ray muon radiography. However, one of the image reconstruction algorithms that will be presented later (PoCA) uses a ray tracing method that is quite similar to that used by Charpak.

2.5 Overview of Computed Tomography

Tomography refers to the reconstruction of an image or object from projections taken from many different directions. Tomographic reconstruction and the associated signal processing is an area of active research, primarily in the fields of electrical engineering and mathematics. The mathematics of this reconstruction process were analyzed early in the 20th century by Radon, as outlined in the historical review in

[23]. Widespread interest in tomographic imaging was spawned much later after the invention of the computed tomography (CT) x-ray scanner by Hounsfield [24], for which he received a Nobel Prize. Since then the techniques for CT have been continuously evolved, taking advantage of the rapid advances in computing power over the last three decades. A variety of information sources have been used for CT, including x-ray attenuation, reflection of radar pulses, gamma ray emission, ultrasound, and nuclear magnetic resonance. Tomographic techniques have been used to reconstruct 3-dimensional objects from 2-dimensional proton radiography projections (see section 2.4) [25].

It is not necessary to cover herein the array of CT techniques and applications, many of which are highly specialized. There are, however, two major families of techniques for reconstruction from projections: transform methods and algebraic methods. The highlights of these two families will be discussed in the next two subsections.

2.5.1 Transform-based CT

Transform based methods are used in the bulk of CT applications. Unfortunately, it will be seen that transform methods are inappropriate for the research described herein. However, the frequency domain interpretation of projection data allows for intuitive understanding of the reconstruction process and difficulties that can occur when data is limited, as is the case with cosmic ray muon radiography. It is therefore instructive to outline the basics of transform based CT (summarized from a presentation in [23]).

Referring to Figure 2.7(a), one may mathematically express a projection through line integrals. Let $f(x,y)$ represent some measurable function, characteristic of the object, which varies spatially (the tendency to attenuate x-rays, for example). Passing a parallel beam of rays through the object, oriented at angle θ, creates a projection $P_\theta(t)$, where the dimension t may be described via the equation:

$$t = x\cos\theta + y\sin\theta \tag{2.3}$$

The projection may be expressed by the integration (known as the *Radon Transform*):

$$P_\theta(t) = \int_{-\infty}^{\infty}\int_{-\infty}^{\infty} f(x,y)\delta(x\cos\theta + y\sin\theta - t)dxdy \tag{2.4}$$

The reconstruction problem is established by creating a number of projections, rotating through various angles as shown in Figure 2.7(b), and seeking to reconstruct $f(x,y)$ from those projections.

It is in the frequency domain that the nature of sampling the image via projections becomes clear. First define the 2-dimensional Fourier transform of the object function:

$$F(u,v) = \int_{-\infty}^{\infty}\int_{-\infty}^{\infty} f(x,y)e^{-j2\pi(ux+vy)}dxdy \tag{2.5}$$

The one-dimensional Fourier transform of a projection is:

$$S_\theta(w) = \int_{-\infty}^{\infty} P_\theta(t)e^{-j2\pi wt}dt \tag{2.6}$$

The *Fourier Slice Theorem* allows interpretation of the projections in the frequency domain. To illustrate the theorem, consider the Fourier transform of the object along a line in the frequency domain where $v = 0$:

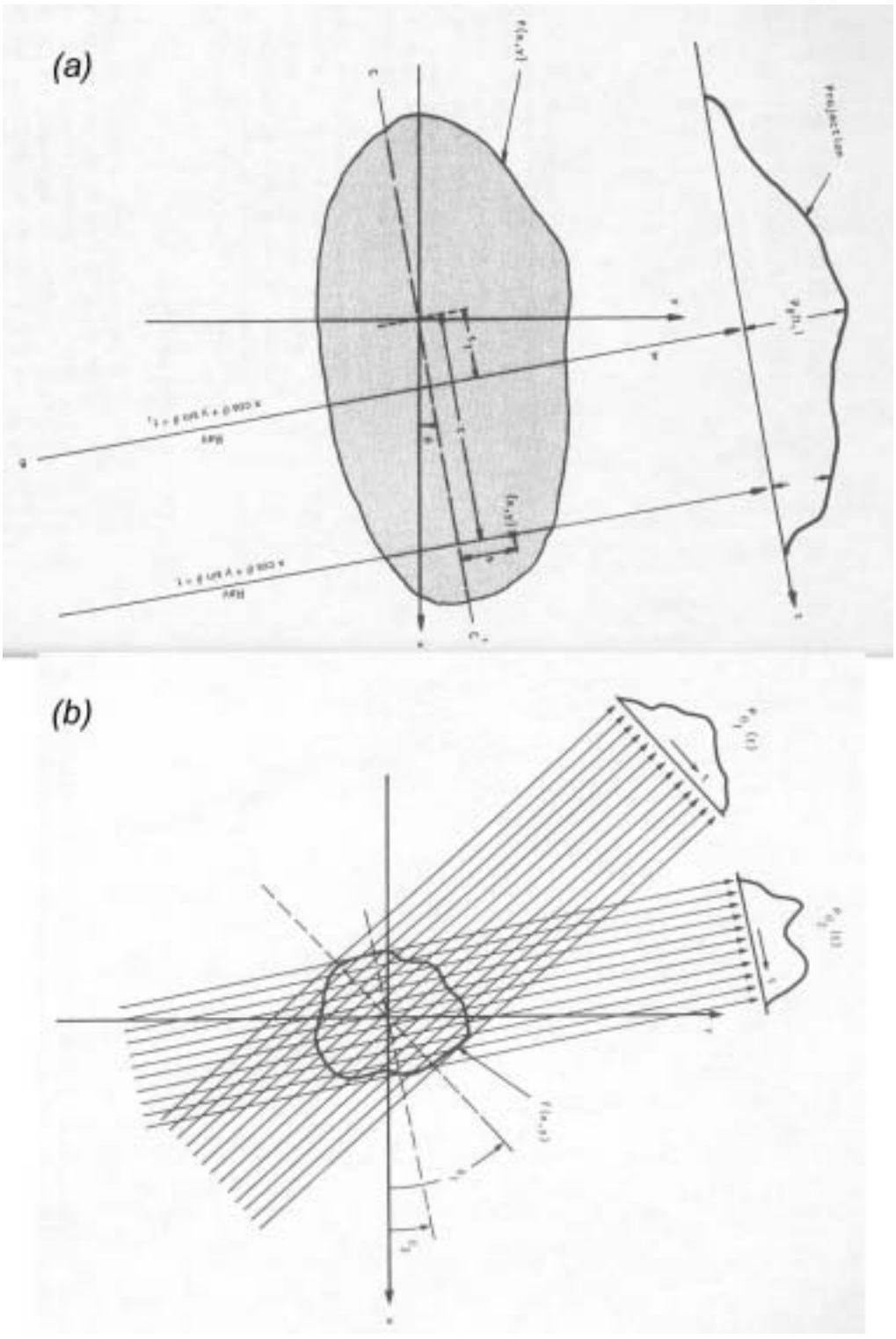

Figure 2.7 Illustration of projections in CT. An object and its projection at angle θ (b), and multiple projections at different angles (from [23], used with permission).

$$F(u,0)=\int_{-\infty}^{\infty}\int_{-\infty}^{\infty}f(x,y)e^{-j2\pi ux}dxdy=\int_{-\infty}^{\infty}\left[\int_{-\infty}^{\infty}f(x,y)dy\right]e^{-j2\pi ux}dx \tag{2.7}$$

Now, writing the equation for the projection when $\theta=0$:

$$P_{\theta=0}(t)=\int_{-\infty}^{\infty}\int_{-\infty}^{\infty}f(x,y)\delta(x-t)dxdy=\int_{-\infty}^{\infty}f(x,y)dy \tag{2.8}$$

Note that the term in brackets in Eq. (2.7) is just the projection defined in Eq. (2.8). Substituting the result of Eq. (2.8) into Eq. (2.7):

$$F(u,0)=\int_{-\infty}^{\infty}P_{\theta=0}(x)e^{-j2\pi ux}dx \tag{2.9}$$

Eq. (2.9) may be recognized as the one-dimensional Fourier transform of the projection $P_{\theta=0}$, therefore:

$$F(u,0)=S_{\theta=0}(u) \tag{2.10}$$

This result is independent of the specific angle θ, and leads to the Fourier Slice Theorem, which is illustrated in Figure 2.8(a) and (b), and may be stated as:

> The Fourier transform of a parallel projection of an image $f(x,y)$ taken at angle θ gives a slice of the two-dimensional transform, $F(u,v)$, subtending an angle θ with the u-axis. In other words, the Fourier transform of $P_\theta(t)$ gives the values of $F(u,v)$ along the line BB in Figure 2.8(b).

Therefore, one may interpret multiple projections at different angles as providing sampling of the frequency domain representation of the object, as illustrated in Figure 2.8(c), where the dots show sampled points obtained when using an FFT and finite data.

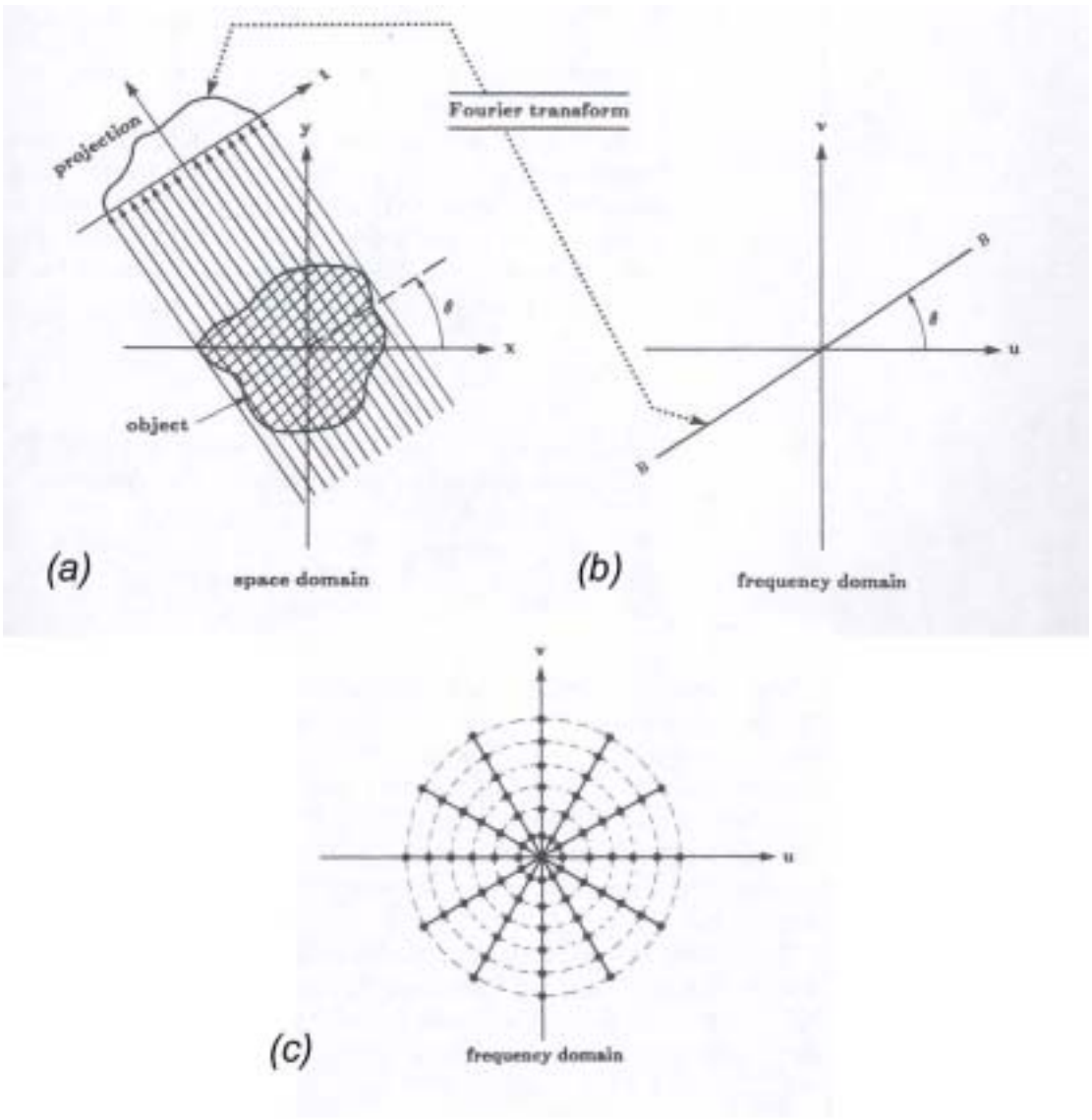

Figure 2.8 Illustration of how projections may be interpreted in the frequency domain. A projection of an object at angle θ in the space domain (a), when Fourier transformed, gives a slice of the two-dimensional transform of the object at an angle θ (b). The FFT of multiple projections represents samples of the object FFT as shown in (c) (from [23], used with permission).

It may be seen from Figure 2.8(c) that, the farther from the center, the sparser the density of the sampled points. In reconstructing the object from projections, this implies that there will be more error in the high frequency content of the image than in

the low frequency content. The fewer the number of projections, the less accurate the fine detail in the reconstruction. Or imagine that the projection set contained no projections from angles near horizontal (θ nearing $\pm 90°$). In this case ambiguity will exist in the vertical structure of the reconstruction. Insufficient number of samples in each projection, or an insufficient number of projections can also lead to artifacts from aliasing due to under sampling.

The basic transform based reconstruction algorithm used in most straight ray tomographic applications is known as *filtered backprojection*. Making use of the Fourier Slice Theorem, the general algorithm is:

1. Measure the projections.
2. Transform the projections.
3. Apply a filter to the transforms of the projections to properly interpolate them in the frequency domain.
4. Compute the inverse transform of the filtered projections.
5. Sum over the image plane all the inverse transformed filtered projections to obtain the reconstruction.

Again, the lack of an evenly spaced set of projections prohibits the use of the filtered backprojection algorithm or other transform based methods for cosmic ray muon radiography. The next section presents a method better suited to serve as a foundation for the work that will be presented herein.

2.5.2 Algebraic-based CT

The filtered backprojection algorithm presented in the previous section is simple, efficient, and works well under certain conditions. However, projections evenly spaced over at least 180° are generally required. Ray paths must be predominantly straight – significant bending due to refraction, for example, will cause

problems. In some cases (as in the research presented herein) there is no notion of a projection at all. For such applications, *algebraic based CT* may provide acceptable reconstructions.

Algebraic methods consist of expressing the unknown object in terms of a finite set of parameters, and posing the reconstruction problem as a set of algebraic equations in terms of those parameters and the measured "projection" data. Then a solution for the parameters is sought. Following is a summary of the basics of Algebraic Reconstruction Techniques (ART), again following Kak and Slaney [23].

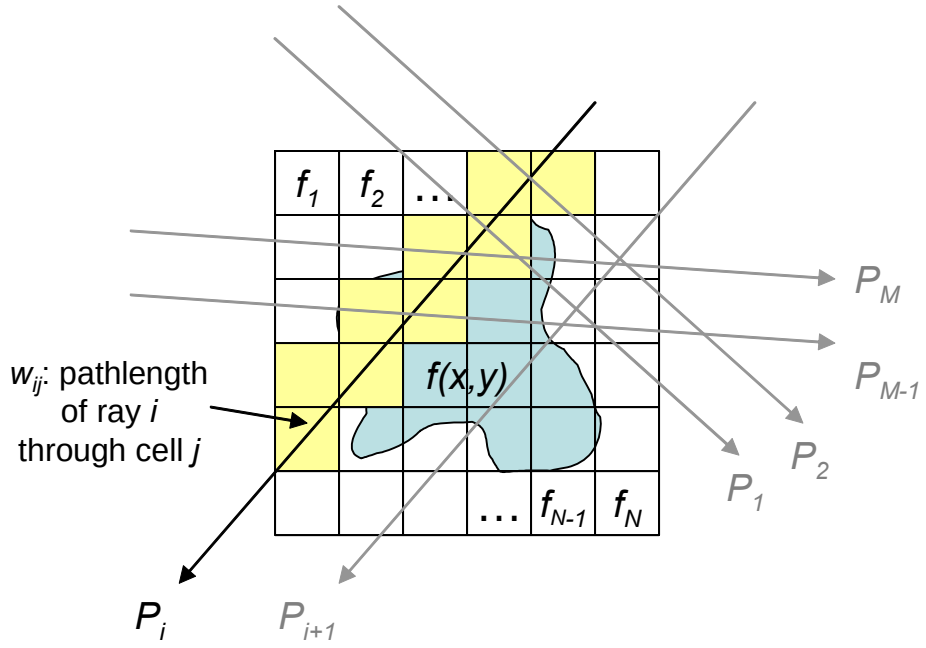

Figure 2.9 In Algebraic Reconstruction Techniques (ART), the object is broken into a discrete grid, and ray projections are modeled as weighted sums of cell values.

Begin by superimposing a square grid over the object, as shown in Figure 2.9 for a two dimensional case. Assume that the function $f(x,y)$ is constant within each cell, and denote these discrete estimates as $f_1, f_2, ..., f_N$. In Figure 2.9, a few rays are

shown passing through the object at different angles – assume that there are a total of M rays in the dataset. Here, the term *projection* refers to the line integral of a single ray in terms of the discrete version of the object. For a given ray, the projection may be expressed as:

$$P_i = \sum_{j=1}^{N} w_{ij} f_j \tag{2.11}$$

where the weight w_{ij} represents the normalized path length of the ray i through cell j. For simplicity assume that the rays are lines – if the rays had some finite width then the weights would become fractions of the cell areas. The aggregate dataset may be expressed through the matrix equation:

$$\mathbf{P} = \mathbf{W}\mathbf{f} \tag{2.12}$$

Eq. (2.12) is a set of linear equations and the typical set of numerical methods may be applied to seek a solution. However, some complicating factors exist:

1. The size of $\mathbf{W}$ can be enormous. If the object grid is 256 x 256, for example, and we have at least one ray per element, then the size of $\mathbf{W}$ is about 65,000 x 65,000. For three dimensional reconstruction, $\mathbf{W}$ is huge even for small sized problems.
2. The system is often underdetermined, i.e., $M < N$.
3. $\mathbf{W}$ may not be invertible, even if $M = N$.
4. The matrix $\mathbf{W}$, the vector $\mathbf{P}$, and the function $f(x, y)$ are typically nonnegative, so we desire a solution for $\mathbf{f}$ that has nonnegative elements.

Nevertheless, iterative numerical techniques may be applied to search for a solution to Eq. (2.12). One such method, the original ART algorithm, was developed in the 1970's by Gordon [26]. The algorithm starts with an initial guess for $\mathbf{f}$; call it $\mathbf{f}^{(0)}$. This estimate will be iteratively adjusted – at iteration k the guess will be

termed $\mathbf{f}^{(k)}$. Consider a particular measured projection P_i, and define Q_i, the expected projection given the guess $\mathbf{f}^{(k)}$, as:

$$Q_i^{(k)} = \mathbf{W_i f^{(k)}} \tag{2.13}$$

where $\mathbf{W_i}$ is the i^{th} row of the weight matrix $\mathbf{W}$. To enforce consistency between $\mathbf{P}$ and $\mathbf{Q}$, an adjustment could be made to obtain $\mathbf{f}^{(k+1)}$ as follows:

$$\mathbf{f}^{(k+1)} = \mathbf{f}^{(k)} + \frac{P_i - Q_i^{(k)}}{\mathbf{W_i^T W_i}} \mathbf{W_i^T} \tag{2.14}$$

In other words, take the difference between the measured projection for a ray and the projection that would result from our estimate, normalize that difference using the norm of that ray's weight vector, then weight the correction across elements of $\mathbf{f}$ by that ray's weight vector.

The update equation in the original form of ART [26] was simplified from Eq. (2.14) by replacing the element in the weight matrix by 0's and 1's, depending on whether the centers of image cells were within each finite width ray. A positivity constraint was also imposed, resulting in:

$$\mathbf{f}^{(k+1)} = \max\left(0, \mathbf{f}^{(k)} + \frac{P_i - Q_i^{(k)}}{N_i}\right) \tag{2.15}$$

where N_i is the number image cells with non-zero weights for the i^{th} ray, and the correction is applied only to those image cells.

A plethora of refinements and application specific revisions were proposed by Gordon, and many more have been made to ART over the years. One particular variation, sometimes called "ART with a Damping Factor," addresses the lack of

convergence of ART when noise is present in the projection data by introducing a "damping factor:"

$$\mathbf{f}^{(k+1)} = \max\left(0, \mathbf{f}^{(k)} + \Delta \frac{P_i - Q_i^{(k)}}{N_i}\right) \tag{2.16}$$

where the damping factor, $0 < \Delta < 1$, can be adjusted to achieve convergence. This version of ART may be seen as quite similar to the LMS algorithm for tuning adaptive filters developed by Widrow [27], and more generally known as *stochastic gradient descent* [28]. We may therefore view algebraic reconstruction techniques as a special form of gradient descent optimization.

In summary, algebraic reconstruction techniques provide a framework for creating tomographic reconstructions when data do not conform to the requirements of transform based techniques. It has been shown that ART is closely related to gradient descent optimization of a linear system, and so exists within a much larger general framework. The maximum likelihood reconstruction algorithm that is presented in Chapter 6 is built upon that framework.

2.6 Summary

This chapter summarized some background information important in the development of cosmic ray muon radiography. The technique is possible, of course, due to the presence on the Earth's surface of a "shower" of cosmic ray muons from the heavens. The creation mechanism was reviewed, and some details describing the flux of cosmic ray muons at the surface were presented. Three major interaction modes occurring when muons pass through material were described. One of those modes, *range out*, has been used in all past efforts to interrogate objects using cosmic ray

muons. A few of the most important of these efforts were described. A second interaction mode, *multiple Coulomb scattering*, forms the information source for the new form of radiography described herein. A prior demonstration of multiple scattering radiography, proton radiography (pRAD), was described. pRAD, wherein images are formed based on the multiple scattering of protons from a beam formed by a linear accelerator, was the inspiration for cosmic ray muon radiography. Finally, an important part of cosmic ray muon radiography is to form 3D images from information gathered by interrogating muons. Therefore, the basics of computerized tomography were outlined.

CHAPTER 3
CONCEPT AND PRELIMINARY CALCULATIONS

In this chapter the concept for cosmic ray muon radiography will be outlined. A general description of the basic concept will first be first provided in Section 3.1. Following in Section 3.2 will be an analysis of the sensitivity of multiple Coulomb scattering (MCS) to material Z number. In this discussion the problem context for muon radiography will be introduced, that being the segregation of low, medium and high Z materials from one another in modest exposure times. In Section 3.3 the feasibility of solving that problem with muon radiography will be examined via a series of simulated analyses of such material segregation with minute order exposure times. The issue of momentum spread will be addressed, and a new concept for the use of MCS to measure of muon momentum will be introduced and analyzed. Section 3.4 summarizes these discussions.

3.1 The Cosmic Ray Muon Radiography Concept

Section 2.1 described the cosmic ray cascade that results in a sea level muon flux of approximately 10,000 $m^{-2} \cdot min^{-1}$. Section 2.2 discussed how muons interact with matter and introduced multiple Coulomb scattering (MCS) as an information source pertaining to the material through which the muons pass. Section 2.4 referenced proton radiography, which provides a prior demonstration of the feasibility of using multiple scattering of charged particles for radiography. Finally, Section 2.5 reviewed how object structure may be reconstructed from the information provided by

interrogating rays through tomographic methods. This section describes a concept for building on this body of information to radiograph and reconstruct objects via the information carried by the multiple scattering of cosmic ray muons.

The concept is illustrated in Figure 3.1. Muon detectors are located above and below a target volume wherein objects of interest are located. Individual muons are tracked into and out of the object volume. This is possible due to the low event rate (about 160 Hz per square meter of detector area). Two position sensitive detectors are located above the object volume, and two below. Each detector measures particle position in two orthogonal coordinates. Via the pair of detectors above the object volume the angle of the incoming track may be calculated. Muons pass through the object volume, and those that pass through dense objects are scattered more than those that pass through less dense objects. Rays that do not pass through objects are not scattered (except through the detectors, which are designed to scatter the particles very little). Scattered muon tracks are measured by the bottom pair of detectors. The bend angle of each track is computed. As many rays pass through the object volume from different angles and positions, an aggregate dataset is created. Tomographic reconstruction techniques may then be applied to this dataset to reconstruct the structure of objects within the object volume in terms of their tendency to scatter muons.

The next section examines the relationship between materials and muon scattering in more detail, and further defines the material identification problem context.

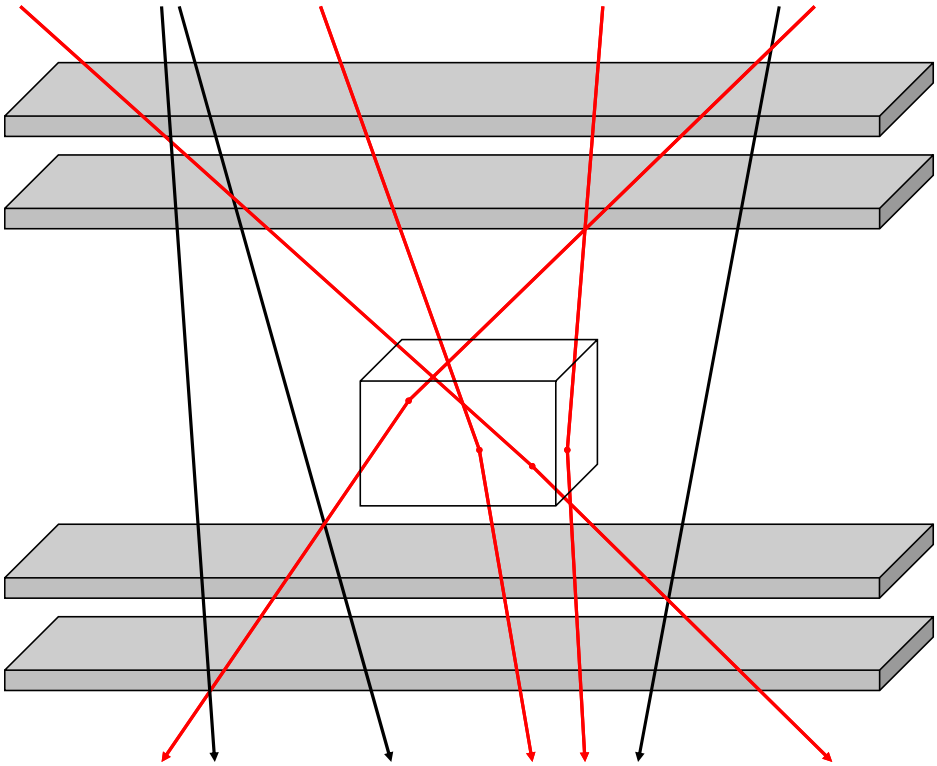

Figure 3.1 The cosmic ray muon radiography concept.

3.2 Using MCS to Segregate High, Medium and Low Z Materials

As described in Section 2.2.3, a charged particle such as a muon, when passing through material, will be scattered from its straight path by multiple electromagnetic interactions with the nuclei of material. The path of an example muon is illustrated in Figure 3.2. Upon exiting the material, the new track of the muon may be described by the projected scattering angles θ_x, θ_y and displacements Δx, Δy where all of these values are expressed relative to the orientation and position of the incident muon. It is intuitively clear that high density / high atomic weight materials wherein interactions with nuclei are more probable might tend to produce a higher degree of muon scattering than lower density, lower atomic weight materials. A theory of multiple

scattering which relates interaction probability to scattering was introduced by Moliere [29] and has since been expanded and refined by others [30, 31]. Moliere's results may not be presented concisely, but it turns out that a simple Gaussian approximation works well for the central 98% of the scattering distribution [32]. For one of the projected scattering angles, θ_x:

$$f_{\theta_x}(\theta_x) \cong \frac{1}{\sqrt{2\pi}\sigma_\theta} \exp\left(-\frac{\theta_x^2}{2\sigma_\theta{}^2}\right) \tag{3.1}$$

The other projected scattering angle, θ_y, is independent from but identically distributed to θ_x [1]. The standard deviation of both distributions may be expressed approximately in terms of material properties [15]:

$$\sigma_\theta \cong \frac{15}{p}\sqrt{\frac{L}{L_{rad}}} \tag{3.2}$$

where p is the particle momentum in MeV/c, L is the depth of the material, and L_{rad} is the radiation length of the material [substitution of the velocity $\beta c \cong 1$ for muons has been made in Eq. (2.2) to arrive at Eq. (3.2).

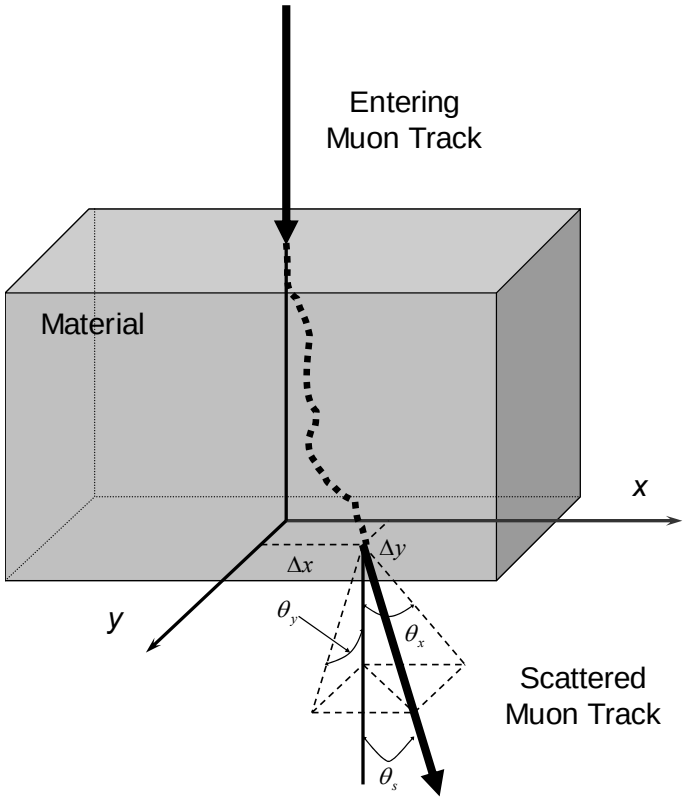

Figure 3.2 Multiple scattering in two dimensions

Radiation length, L_{rad}, is a characteristic amount of matter for electromagnetic interactions. Formally, it is the mean material depth at which a high-energy electron will lose all but $1/e$ of its energy when passing through that material [1]. Radiation length may be expressed as a pure depth (e.g., in cm) or as an areal density (e.g., in $g \cdot cm^{-2}$). When expressed as an areal density, radiation length falls monotonically with increasing material Z (atomic number), as shown in Figure 3.3. When expressed as a depth, volume density, hence the normal state (solid, liquid, gas) of the material affects the number. Radiation length in cm is still strongly a function of material Z, though not as cleanly as the areal density form.

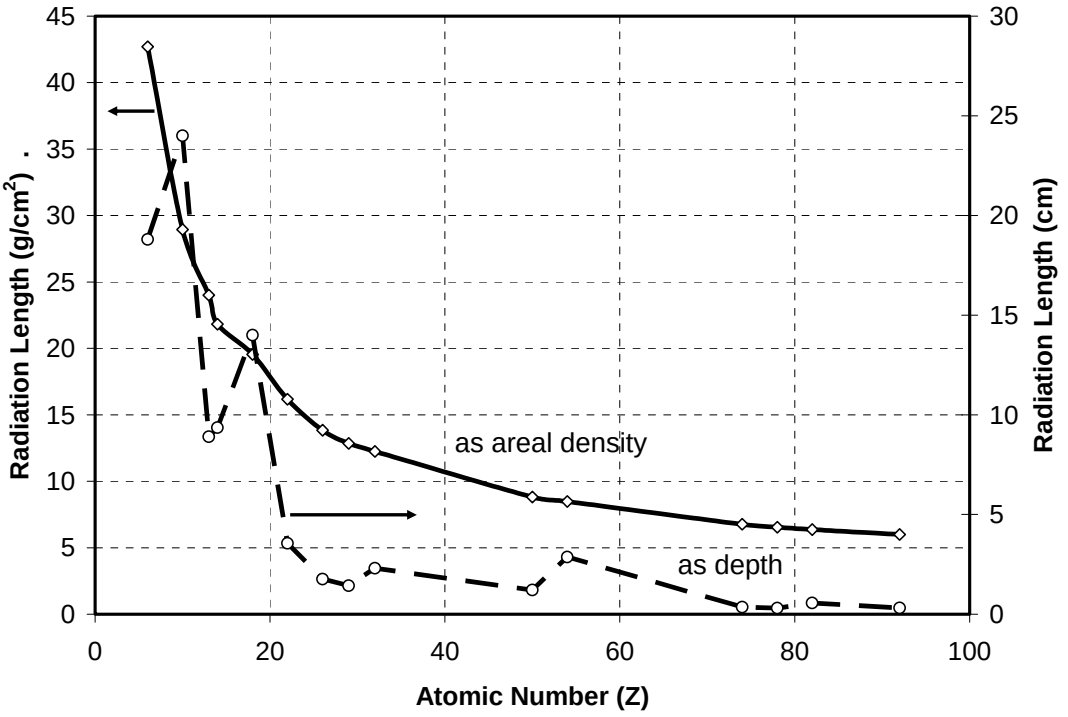

Figure 3.3 Radiation length as a function of material Z.

It is clear from Eq. (3.2) that a large depth of a lower Z (higher L_{rad}) material may produce equivalent scattering to that produced by a higher Z (lower L_{rad}) material. Scattering is also influenced by particle momentum. To identify material it is necessary to normalize for these two effects. Establishing a nominal muon momentum p_0 and squaring both sides of Eq. (3.2):

$$\sigma_{\theta 0}^2 \cong \left(\frac{15}{p_0}\right)^2 \frac{L}{L_{rad}} = \left[\left(\frac{15}{p_0}\right)^2 \frac{1}{L_{rad}}\right] L \tag{3.3}$$

The *scattering density* of a material with radiation length L_{rad} is herein defined as:

$$\lambda_{L_{rad}} \equiv \left(\frac{15}{p_0}\right)^2 \frac{1}{L_{rad}} = \frac{\sigma_{\theta 0}^2}{L} \tag{3.4}$$

Scattering density therefore expresses the mean square scattering expected for nominal momenta muons passing through a unit depth of a material with radiation length L_{rad}.

Figure 3.4 displays the scattering densities of various common liquid or solid materials, making use of Eq. (3.4) and choosing $p_0 = 3\,\text{GeV}$. Though scattering does not increase monotonically with atomic number (tungsten scatters more than lead, for instance), there is a clear separation between the scattering induced by common low, medium, and high Z materials[4].

The problem context for cosmic ray muon radiography is therefore defined to be segregation of objects of low, medium, and high Z materials from one another. This task will be examined in more detail in the next few sections.

[4] There are materials that do not fall cleanly into one of these categories. For instance, silver (Z=47) is of higher Z than copper, but lower than lead. Centimeter depths of silver are arguably uncommon in trucks or shipping containers, for instance, but such potentially ambiguous materials may have to be considered in other problem contexts.

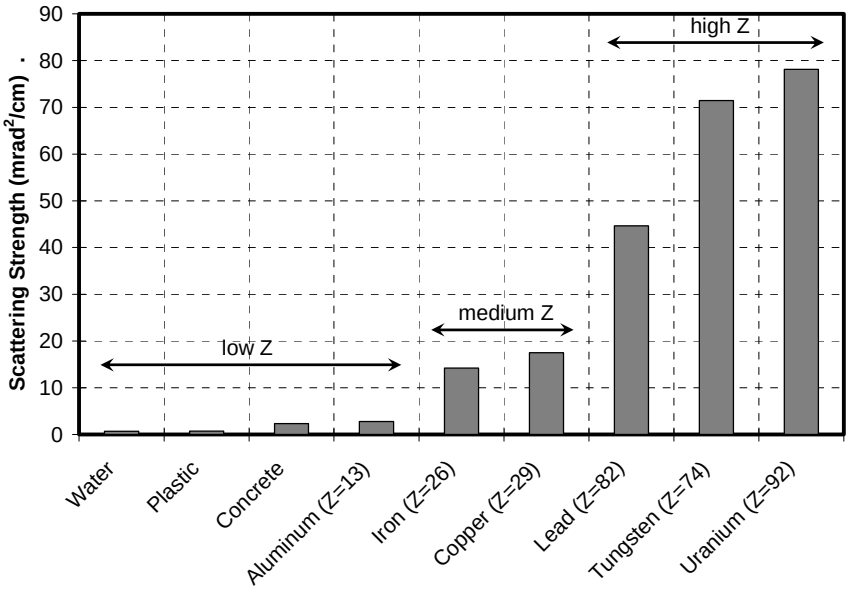

Figure 3.4 Scattering density [per Eq. (3.4)] of various materials.

3.3 Preliminary Calculations on Material Segregation

It has been claimed above that the scattered muons carry information that can allow segregation of high, medium, and low Z materials. It has also been claimed that the muons rate is low enough to allow individual particle detection and analysis. A logical question is: Can material segregation be made in a reasonable amount of time? This section addresses that question via simplified analytical and simulated analysis.

3.3.1 Material Discrimination with Monoenergetic Muons

Consider three cubes, 10 cm on a side, one formed of concrete (low Z), another of iron (medium Z), and a third of uranium (high Z). Cosmic ray muons pass through these blocks, and the scattering of the muons will be used to segregate them. The tracks of the muons are measured, and scattering angles in each of the two orthogonal coordinates are computed. These measurements θ_x and θ_y are samples from

independent, identically distributed random variables [1]. For simplicity, assume that scattering is normalized to account for different path lengths. Ignore the effect of muon energy spread for the time being and assume that all particles arrive at a nominal momentum of $p_0 = 3\,\mathrm{GeV}$. For each cube the scattering density $\lambda = \sigma_{\theta_0}^2 / L$ may be computed.

From the measurement of scattering of N muons, mean square scattering per unit depth is calculated for each cube. For a given cube, this calculation is an estimate of the variance of the underlying approximately Gaussian scattering distribution:

$$\hat{\lambda} = \frac{\hat{\sigma}_{\theta_0}^2}{L} = \frac{1}{2NL} \sum_{i=1}^{N} \left(\theta_x^2 + \theta_y^2 \right)_i \tag{3.5}$$

The random variable:

$$X \equiv \frac{2N\hat{\lambda}}{\lambda} \tag{3.6}$$

is distributed as a chi square distribution with $2N$ degrees of freedom [33]. The central 99% confidence bounds on each scattering density estimate may be expressed as:

$$\begin{aligned} \hat{\lambda}_{low} &= \lambda \frac{\chi_{2N}^{-1}(.005)}{2N} \\ \hat{\lambda}_{high} &= \lambda \frac{\chi_{2N}^{-1}(.995)}{2N} \end{aligned} \tag{3.7}$$

where $\chi_M^{-1}(\alpha)$ denotes the inverse chi squared c.d.f. with *M* degrees of freedom evaluated at probability α.

At the typical sea-level flux, about 100 cosmic ray muons pass through these cubes per minute. So for each cube, in one typical minute, 200 measurements of scattering angle are obtained. Using Eqs. (3.2) and (3.5), Table 3.1 presents the confidence intervals expected in one minute of muon tracking. Clearly the three materials may be segregated in less than one minute.

Table 3.1 Confidence intervals on scattering density after one minute of tracking 3 Gev muons through 10 cm of various materials.

	Scattering Density, milliradians^2/cm		
Material	Lower CL	Actual	Upper CL
Concrete	1.8	2.3	3.0
Iron	10.8	14.2	18.1
Uranium	59.5	78.1	99.7

As verification, Eq. (3.2) was used to randomly generate scattering of 3 Gev muons through the three materials. 200 scattering measurements were generated at a time, $\hat{\lambda}$ estimates were calculated for each cube, and this experiment was repeated 5,000 times. Results are shown in Figure 3.5 with central 99% percentiles shown. These results verify those of Table 3.1 and illustrate the separability of these materials.

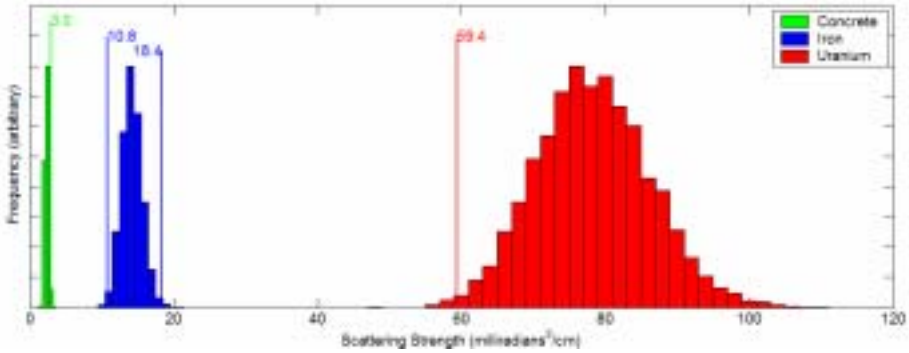

Figure 3.5 Discrimination of materials using scattering of 3 GeV momentum muons with ~1 minute of exposure (simulated results). Central 99% percentiles are shown.

Of course there are several additional factors to be considered that will decrease the margin of separability shown in Figure 3.5. Real detectors will exhibit measurement error and less than perfect efficiency in detecting muons and these practical considerations will widen the distributions shown in Figure 3.5. These baseline results are presented only to show rough feasibility which motivates more in depth study. The first complication that will be addressed in the next section is momentum spread.

3.3.2 Material Discrimination with Realistic Muon Momentum Spread

The arrival angle and momenta distribution of cosmic ray muons was discussed in Section 2.1.2. This distribution has been experimentally documented and has been modeled via a mixture of theoretical and empirical methods. One such model, developed by Gary Blanpied [14] is described in Appendix A. Code for the "generation" of simulated muons drawn from the documented arrival zenith angle (φ) and momenta (p) spectrum $f_{p,\varphi}(p,\varphi)$ was developed based on this model. Simulated results presented in this section were performed using muons drawn from the Blanpied Generator.

If muon momentum is not fixed, then the scattering of a particular muon becomes a function not only of the material through which it passed, but also of the momentum of that particular muon. Clearly the variance in muon to muon momentum will contribute to additional variance in the scattering signal over and above the counting statistics described in the previous section. Moreover, if absolute rather than purely relative material information is sought (i.e., in addition to segregating materials

of dissimilar Z, the absolute Z level (high, medium, low) of materials is required), then some means to normalize for momentum variation is desirable.

If an estimate of individual muon momentum is available, then one might compute scattering density by refining Eq. (3.5):

$$\hat{\lambda} = \frac{1}{2NL} \sum_{i=1}^{N} \left[\left(\theta_x^2 + \theta_y^2 \right)_i \left(\frac{\hat{p}_i}{p_0} \right)^2 \right] \tag{3.8}$$

where $\hat{p}_i$ is the estimate of the momentum of the i^{th} muon and p_0 is a nominal momentum (say 3 GeV, as in the previous section). The precision of this estimate is influenced by the precision of the momentum estimates. This will be addressed in detail in a subsequent section.

For the present, no knowledge of individual muon momenta will be assumed except that muon momentum is described by the empirically known distribution $f_p(p)$. Eq. (3.8) will be used, but $\hat{p}$ will be equal to a selected constant for all muons. The selection of the value for assumed momentum will be made such that the estimate $\hat{\lambda}$ is unbiased:

$$\begin{aligned} &\hat{p} = c, \\ &\therefore E\left[\hat{\lambda}(\hat{p})\right] = \lambda \end{aligned} \tag{3.9}$$

It will be shown that *c* can be computed as a function of moments of the distribution $f_p(p)$. In the following example *c* was simply empirically adjusted to satisfy Eq. (3.9)

Passage of simulated muons through the concrete, iron, and uranium cubes of the previous section was simulated. Once again muons were taken 200 at a time, and scattering density estimates $\hat{\lambda}$ were calculated via Eq. (3.8) with $\hat{p}$ adjusted to satisfy Eq. (3.9). The experiment was performed 5000 times to assess the variability in the estimates. Results are shown in Figure 3.6. The three materials are no longer distinguishable from one another with 99% confidence in this simulated one minute exposure, though almost distinguishable. Increasing exposure time to 2 minutes predictably improves separability as shown in Figure 3.7.

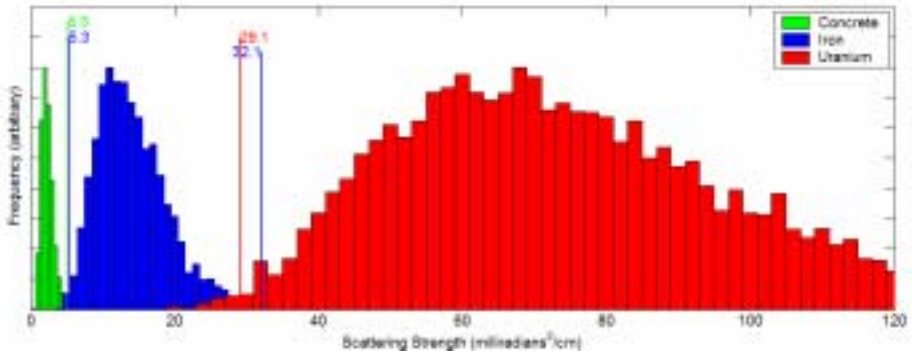

Figure 3.6 Discrimination of materials using scattering of muons with momenta drawn from a model of the cosmic ray spectrum; ~1 minute of exposure (simulated results). Central 99% percentiles are shown.

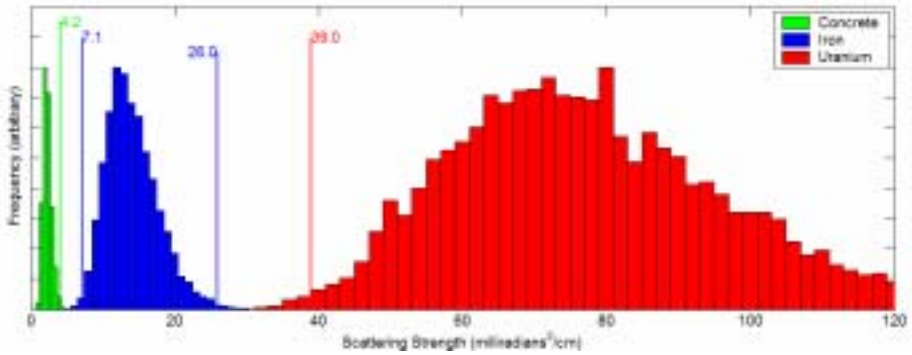

Figure 3.7 Improved discrimination of materials using 2 minutes of exposure to muons with momentum spread (simulated results). Central 99% percentiles are shown.

Additional factors not considered in this simple analysis will certainly be present in a real implementation and will increase required exposure time. However, these preliminary calculations indicate that material discrimination with minute-order exposure times might be reasonably expected. Moreover, measurement of muon momentum would improve matters. One particular means for momentum measurement will be introduced in the next subsection and examined in detail in a subsequent chapter.

3.3.3 Material Discrimination with Muon Momentum Spread and Momentum Measurement

The previous two subsections illustrated the importance of the cosmic ray muon momentum spread in the ability to segregate materials by Z. The results of Section 3.3.1 are not practically achievable but represent a theoretical bound. Those results can be approached by making use of muon momentum measurement.

Obtaining a precise measurement of particle momentum is expensive. The most common means is to create a magnetic field through which the charged particles pass [15]. The charged particles will be deflected by the field to a degree inversely proportional to momentum, and by measuring the curvature of the tracks momentum can be inferred. It is possible that such a scheme could be used for cosmic ray muon radiography, but some of the attractive features of the method would be sacrificed (e.g., freedom from a large, complex, energy expensive source). Furthermore, a much less precise measurement of momentum might provide acceptable results.

That muon momentum influences multiple scattering suggests the possibility of measuring momentum via multiple scattering. Inferring the momentum of muons

produced from a linear accelerator by measuring the displacement resulting from scattering was investigated in [34]. A setup for making such a measurement in the muon radiography context was independently proposed by the LANL team in [7], though the first detailed analysis appears herein.

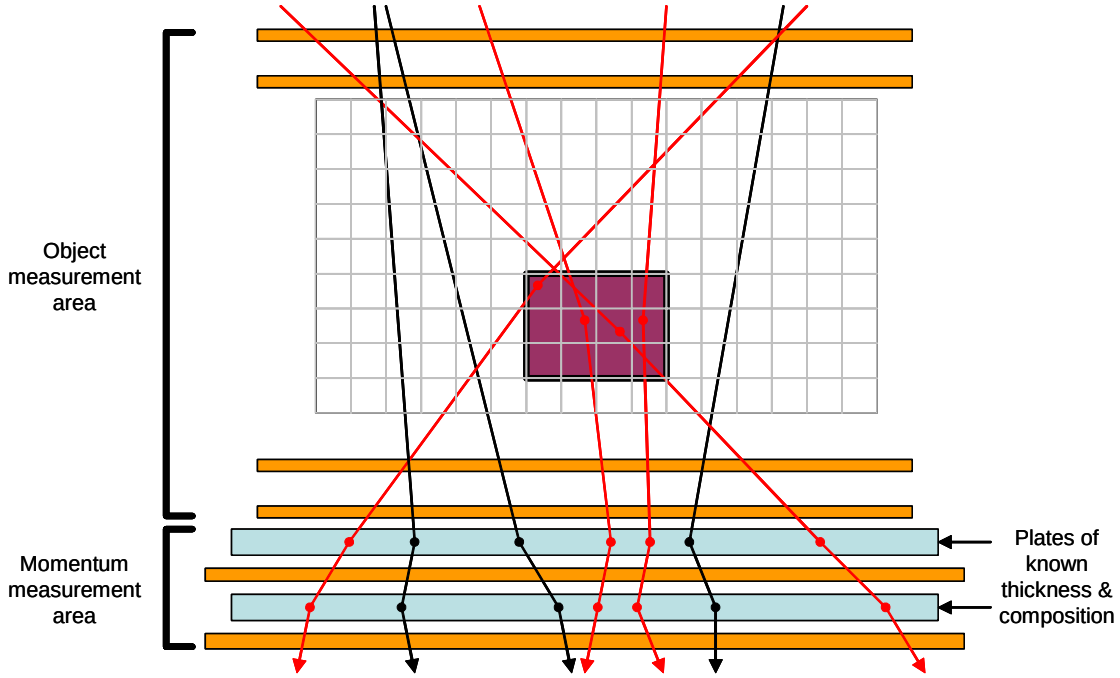

Figure 3.8 Illustration of muon momentum measurement via multiple scattering through layers of material of known thickness and composition.

The concept is illustrated in Figure 3.8. The upper portion of the diagram, labeled "object measurement area," is the same as was shown in Figure 3.1. Added below, and labeled "momentum measurement area." are additional detectors sandwiching plates of predetermined material and thickness such that $R \equiv \left(L/L_{rad}\right)_{plate}$ is identical and known for each plate. For each muon that passes through the instrument, two measurements of scattering (one in each orthogonal plane) may be

made for each such plate deployed. If M such measurements are made in the momentum measurement area, RMS scattering is calculated as:

$$s = \sqrt{\sum_{j=1}^{M} \frac{\theta_j^2}{M}} \tag{3.10}$$

Considering Eq. (3.2), a muon momentum estimate of the following form is proposed,

$$\hat{p} \equiv F_p(M) \frac{15}{s} \sqrt{R} \tag{3.11}$$

where $F_p(M)$ is an adjustment factor required to produce an unbiased momentum estimate. Using such a momentum estimate requires another adjustment factor $F_\lambda(M)$ to be introduced to ensure an unbiased scattering density estimate:

$$\hat{\lambda} = \frac{F_\lambda(M)}{2NL} \sum_{i=1}^{N} \left[\left(\theta_x^2 + \theta_y^2 \right)_i \left(\frac{\hat{p}_i}{p_0} \right)^2 \right] \tag{3.12}$$

Expressions for these adjustment factors can be analytically derived. That derivation and additional analysis of momentum measurement via scattering are discussed in Appendix B. For the moment, the analysis of the previous two sections will be extended to the case where muon momentum is measured via two plates $(M = 4)$.

Results for 5000 simulated trials of the same 100 muon (one minute) exposure of the three cubes are shown in Figure 3.8. Muons were drawn from the Blanpied generator. Momentum measurement allows once again for the discrimination of the three cubes at 99% confidence in one minute of exposure.

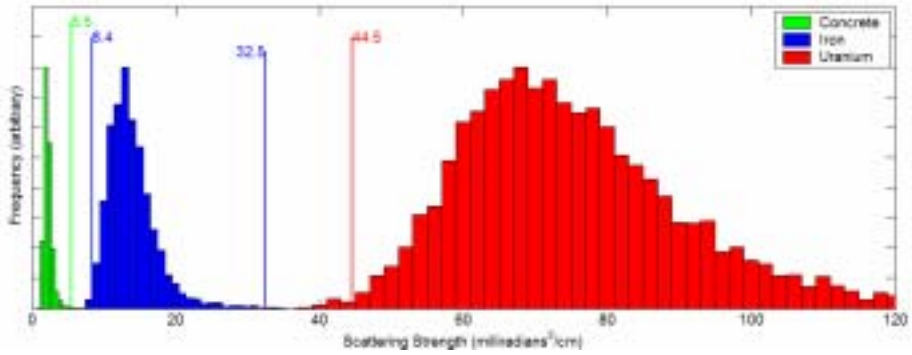

Figure 3.9 Discrimination of materials using scattering of muons with momentum measured via 2 plates in the setup of Figure 3.8; ~1 minute of exposure (simulated results). Central 99% percentiles are shown.

3.4 Summary

The purposes of this chapter were to outline the cosmic ray muon radiography concept, to introduce the problem context (discriminating between high, medium and low Z materials in minute order exposure times), and to provide supportive analysis indicating the likelihood of feasibility. In so doing the relationship between MCS and material Z was examined, and scattering density was defined as a characteristic parameter which might be used to segregate material. The effect of muon momentum spread was discussed, and a simple method for estimating muon momentum via MCS was presented. The material in this chapter sets the stage for what is to follow: experimental demonstration of cosmic ray muon radiography and presentation of new reconstruction algorithms.

CHAPTER 4
RECONSTRUCTON FRAMEWORK AND POCA ALGORITHM

In this chapter the tomographic reconstruction problem within the cosmic ray muon radiography context will be examined. In Section 4.1 the framework for algebraic tomographic reconstruction introduced in Section 2.5.2 will be reviewed and that framework will be extended for the multiple Coulomb scattering information source. Discussion of a full tomographic algorithm will be postponed until Chapter 6, but in Section 4.2 a heuristic algorithm, the Point of Closest Approach (PoCA) algorithm, will be presented and demonstrated. The PoCA algorithm was developed to provide a simple means of illustrating results of the experimental demonstration to appear in Chapter 5.

4.1 The Tomographic Reconstruction Framework

In Section 2.5 an overview of tomographic reconstruction was presented, where tomography refers to the reconstruction of an image or object from projections taken from many different directions. In this section the framework for tomographic reconstruction using multiple Coulomb scattering (MCS) will be established. Once again this discussion will be carried out from a 2D perspective for simplicity of presentation, and later extended to the 3D case.

4.1.1 Framework for the Traditional Case with a Deterministic Ray Signal

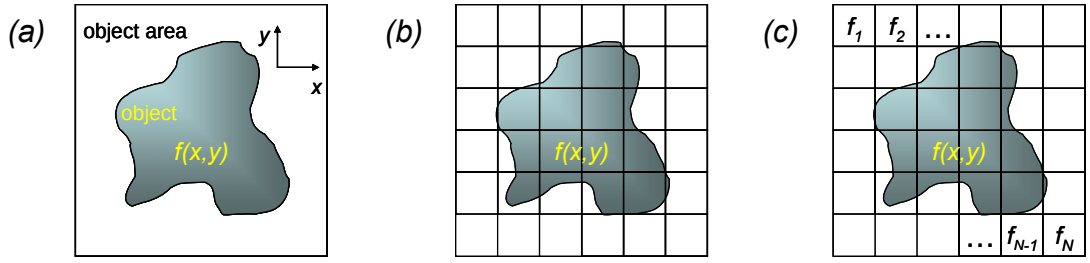

Figure 4.1 A 2D object possessing a continuous characteristic function (a), overlaying a discrete grid (b), and creating a discrete representation of the object characteristic function (c).

Figure 4.1(a) illustrates an object possessing some unknown characteristic function $f(x,y)$ contained within an object area. For traditional tomography the characteristic function $f(x,y)$ might represent the tendency to attenuate x-rays, for example. A uniform grid of pixels is overlaid over the object area in Figure 4.1(b), and a discrete model of the object is illustrated in Figure 4.1(c). A piecewise constant model of the continuous function $f(x,y)$ is adopted by assuming uniform values within each pixel, denoted by the values $f_1, f_2, ..., f_N$.

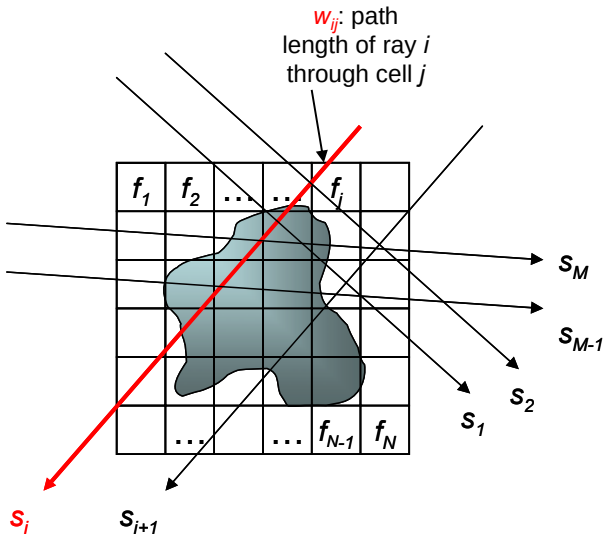

Figure 4.2 Sampling the object by passing interrogating rays through it.

In Figure 4.2 the passage of M interrogating rays through the object area is illustrated. Each ray samples the object characteristic function along the line through which it passes. For example, the i^{th} ray passes through the object area, and its path and the value, or signal, of its sampling, s_i are observed. The path of each ray is expressed by defining a set of weights that contain the path length of that ray through each of the N pixels. The relationship between a given ray's signal and the discrete model of the object characteristic function is defined by the following *raysum* expression:

$$s_i = \sum_{j=1}^{N} w_{ij} f_j \tag{4.1}$$

where w_{ij} represents the path length of the i^{th} ray through the j^{th} pixel.

In Eq. (4.1), the ray signal value s_i is measured and the weights w_{ij} are calculated. In the reconstruction problem the characteristic function values f_j are unknown and estimates $\hat{f}_j$ are sought. Considering all M rays, the aggregate dataset in terms of function estimates may be expressed via the matrix equation:

$$\mathbf{s} = \mathbf{W}\hat{\mathbf{f}} \tag{4.2}$$

Given the measured ray signal vector $\mathbf{s}$ and ray paths expressed via the matrix $\mathbf{W}$, a solution for the reconstructed characteristic function vector $\hat{\mathbf{f}}$ may be sought. The solution is limited by the adequacy of the sampling, or the rank of $\mathbf{W}$. If $\mathbf{W}$ is of less than full rank (i.e., the problem is under determined) then some constraint might be applied to the solution process. If the problem is over determined and noise exists in

the measured ray signals then a least squares approach might be used. A family of iterative solution techniques known as Algebraic Reconstruction Techniques (ART) were discussed in Section 2.5.2.

4.1.2 Framework for the Stochastic MCS Ray Signal

In the previous chapter the problem context for cosmic ray muon radiography was defined to be the segregation of low, medium and high Z materials based on the multiple scattering of muons passing through the material. In Section 3.2 MCS was discussed in detail and the Gaussian approximation of muon scattering in material was presented in Eqs. (3.1,2). The *scattering density* of a material was defined to be:

$$\lambda_{L_{rad}} \equiv \left(\frac{15}{p_0} \right)^2 \frac{1}{L_{rad}} \tag{4.3}$$

where p_0 is a nominal muon momentum and L_{rad} is material radiation length as described in Section 3.2. Scattering density expresses the mean square scattering expected for nominal muons passing through a unit depth of a material with radiation length L_{rad} and was shown to be a potentially effective information source for the segregation task. The variance of projected scattering of nominal muons through a finite depth L of a material of radiation length L_{rad} may be expressed as:

$$\sigma_\theta^2 = \lambda_{L_{rad}} L \tag{4.4}$$

As shown in Chapter 3, scattering density differs strongly between materials of different atomic number (Z). In the previous section a generic material characteristic function $f(x,y)$ was referred to and a reconstruction of a discrete version $\hat{\mathbf{f}}$ was sought. In this section the characteristic function will be taken to be $\lambda(x,y)$, and a

reconstruction of the discrete version $\hat{\boldsymbol{\lambda}}$ will be sought for the purpose of discriminating between materials of differing Z.

In the deterministic case of the previous section ray signals were directly related to the material characteristic function and ray path as expressed in Eq. (4.1). In the stochastic case this relationship is different. To illustrate the influence of scattering density on ray signal, consider Figure 4.3, wherein single and multiple rays corresponding to muons of nominal momentum p_0 are shown passing vertically through a depth L of a material with scattering density λ. The magnitude of the scattering angles shown in Figure 4.3 are greatly exaggerated for illustrative purposes.

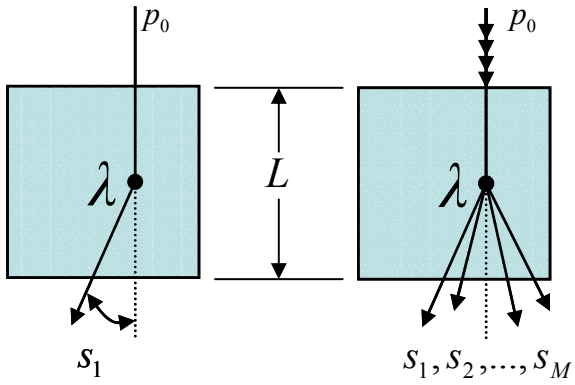

Figure 4.3 Multiple scattering produces a stochastic ray signal.

If the signal of a single ray is taken to be its scattering angle, then that signal is stochastic, and represents a sample of a random variable that is normally distributed with variance:

$$\sigma_s^2 = \lambda L \tag{4.5}$$

Therefore, to estimate the material characteristic function (scattering density) from ray signals in the stochastic case, a different formulation is necessary from that used in the deterministic case. In the simple case of Figure 4.3, if M rays pass through the

material along the same path, then an estimate of the scattering density may be formed as:

$$\hat{\lambda} = \frac{\hat{\sigma}_s^2}{L} = \frac{1}{L}\sum_{i=1}^{M}\frac{s_i^2}{M} \tag{4.6}$$

This form for estimating the scattering density of a homogenous piece of material was used for the examples of Chapter 3. It is important to note that **scattering density may be estimated as the mean square of the path length normalized ray signals**. Of course to duplicate the problem of the previous section the framework must incorporate the effect of a ray passing through multiple pixels representing material with different values of scattering density, and this will be addressed below. However, the Point of Closest Approach (PoCA) algorithm relies on a simplifying assumption and utilizes an estimate of the form of Eq. (4.6), as will be seen later.

It is also worth noting at this point that muons of varying momenta may be dealt with via the normalization procedures outlined in Sections 3.3.2 and 3.3.3. Finally, if rays passed through the material of Figure 4.3 not strictly vertically, but from many different directions such that path length was different for each ray, then Eq. (4.6) should be modified to:

$$\hat{\lambda} = \sum_{i=1}^{M}\frac{s_i^2}{ML_i} \tag{4.7}$$

where L_i is the path length of the i^{th} ray through the material.

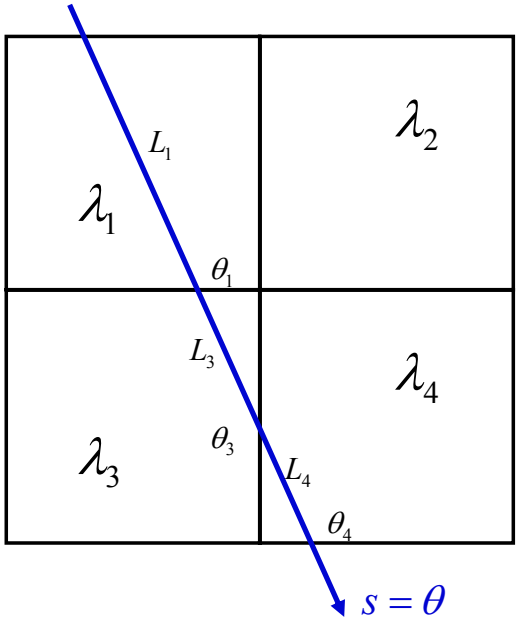

Figure 4.4 A small grid containing scattering density estimates with a single ray passing through.

Figure 4.4 illustrates a small grid wherein scattering density varies for each of the $N = 4$ pixels, denoted by λ_j for the scattering density value assigned to the j^{th} pixel. A ray passes through the grid and the ray signal, s, is taken to be the scattering angle, θ, of the ray, where scattering angle is assumed very small relative to cell size, so a straight ray is shown. Ray path lengths through pixels are denoted by L_j. The unobserved scatterings of the ray through each of the pixels (unobserved), are denoted by θ_j. Following Eq. (4.5), the variance of the individual scattering values are:

$$\sigma_{\theta_j}^2 = L_j \lambda_j \tag{4.8}$$

The ray signal may be expressed in terms of the individual pixel scattering values:

$$s = \theta = \sum_{j=1}^{N} \theta_j \tag{4.9}$$

Since the individual pixel scattering values are each independent of one another, the variance of the ray signal may be written as the sum of the pixel variances:

$$\sigma_s^2 = \sum_{j=1}^{N} \sigma_{\theta_j}^2 = \sum_{j=1}^{N} L_j \lambda_j \tag{4.10}$$

Eq. (4.10), for the stochastic signal, is of the same form as Eq. (4.1) for the deterministic signal. The difference is that Eq. (4.1) expressed the relationship between material characteristic function and a *ray signal value* itself, whereas Eq. (4.10) expresses the relationship between material and the *expected variance in a ray signal value*. To express, for the stochastic case, an expression for a full dataset analogous to Eq. (4.2), an expression relating measured ray signal values to the probability distribution determined by the scattering density vector and path length matrix is necessary. This topic will be addressed using a maximum likelihood method in Chapter 6.

The PoCA algorithm presented in the next section relies on a simplifying assumption to avoid the complexity of dealing with multiple different materials along a ray path.

4.2 The Point of Closest Approach (PoCA) Reconstruction Algorithm

A formalism for extending traditional tomographic methods to cosmic ray muon radiography using multiple scattering as an information source will be presented in Chapter 6. Prior to the development of that formalism a relatively simple, heuristic algorithm was developed to support the proof of principle effort. The Point of Closest Approach (PoCA) algorithm was developed as a joint effort of the Los Alamos National Laboratory development team. Results using an early version of the

algorithm appeared in [2], and the central concept of the method was introduced in [7]. A refined PoCA algorithm was developed by the author based on that work, was presented in [35], and is further detailed in this section.

4.2.1 Description of the 2D PoCA Algorithm

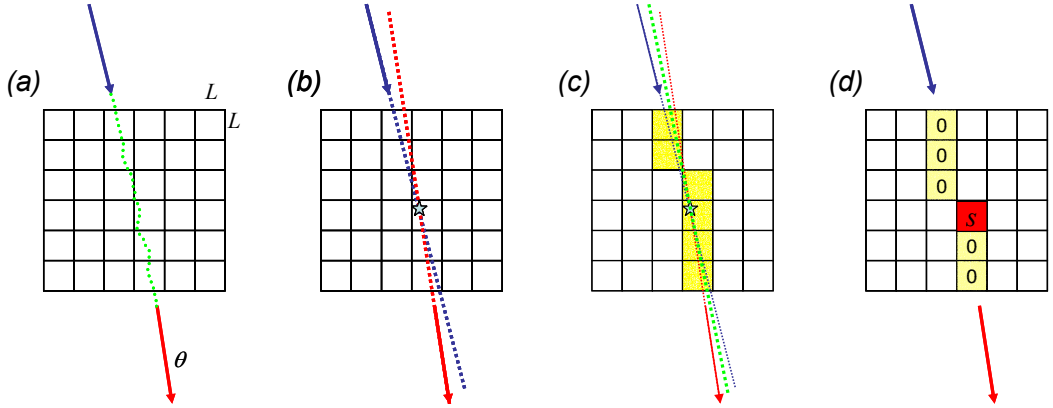

Figure 4.5 Illustration of the PoCA algorithm (see text).

The PoCA algorithm is illustrated in Fig. 4.5. It is shown in 2D for simplicity of presentation, though extension to 3D is straightforward. A muon takes a stochastic scattered path through the object area broken into LxL pixels (Figure 4.5(a)). The exact path is unknown, but the entering and exiting tracks are known, and the scattering angle $\theta = \theta_{out} - \theta_{in}$ may be calculated. Then the central assumption in the method is made, that being that the scattering occurred due to a single scattering event. The estimated point of scatter is located by extrapolating the incident and scattered tracks (Figure 4.5(b)) to their point of closest approach (in 2D the tracks must cross, but in 3D they may not). This ray tracing technique is similar to that used in a nuclear scattering reconstruction technique previously described in [22]. Since the scattering is of order ~milliradians and will be assumed geometrically insignificant relative to

the pixel size ($L \geq 1$ cm), the path may be approximated by a straight line that intersects the PoCA point and bisects the angle between the entry and exit rays (Figure 4.5(c)). Pixels through which that line passes will be taken as candidates for having influenced the ray. The information signal for the ray is simply taken to be the square of the ray's scattering angle:

$$s = \theta^2 \tag{4.11}$$

That signal is assigned to the pixel containing the point of closest approach, or simply the pixel containing the ray crossing point in 2D.

As M muons pass through the object volume, the scattering density vector is estimated by taking the mean of the contributions from all muons to each pixel and dividing by pixel dimension, as illustrated in Figure 4.6, where all operations are carried out element by element and only elements containing signal or zero are included in the cell means. This process may be seen as similar to the estimate of Eq. (4.6) for a single piece of material, where the PoCA process has assigned the signal of each ray to a single pixel. In other words, each pixel is filled with the mean square scattering per unit length of muons estimated to have been influenced by that pixel. The steps of the 2D PoCA algorithm are outlined below, where some items such as computing the estimated ray path may be accomplished in a straightforward manner and are not detailed.

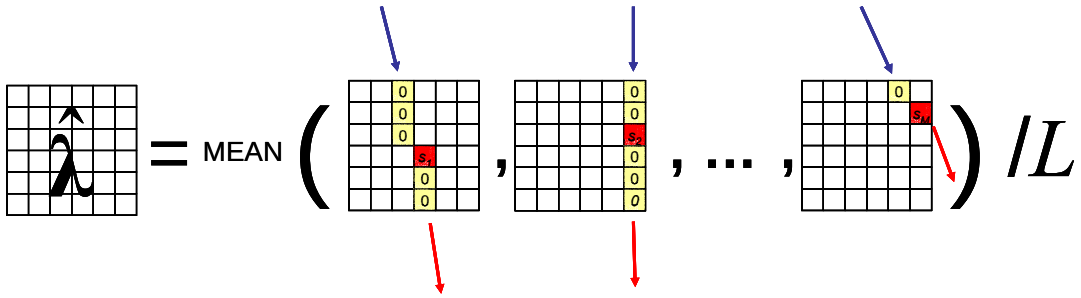

Figure 4.6 Illustration of how the PoCA algorithm is used to reconstruct object scattering density.

2D PoCA Algorithm

1. Establish an NxN grid of LxL sized pixels over the object area, and initialize NxN matrices $\mathbf{S}$, $\mathbf{I}$, and $\boldsymbol{\lambda}$. Establish a Cartesian coordinate system with x horizontal, y vertical. Measured data is $(x_{in}, y_{in}, \theta_{in}, x_{out}, y_{out}, \theta_{out})$ for each of M rays.
2. For $i := 1$ to M % loop over rays
   - 2.1. $(x_{in}, y_{in}, \theta_{in}, x_{out}, y_{out}, \theta_{out}) := (x_{in}, y_{in}, \theta_{in}, x_{out}, y_{out}, \theta_{out})_i$ % Get ray data
   - 2.2. $s := (\theta_{out} - \theta_{in})^2$ % Compute ray signal
   - 2.3. $p_{poca} := poca(x_{in}, y_{in}, \theta_{in}, x_{out}, y_{out}, \theta_{out})$ % Compute the index of the PoCA pixel.
   - 2.4. $\mathbf{p}_{\mathbf{ray}} := raypixels(x_{in}, y_{in}, \theta_{in}, x_{out}, y_{out}, \theta_{out})$ % Compute the estimated list of pixels through which the ray passes.
   - 2.5. $\mathbf{S}(p_{poca}) := \mathbf{S}(p_{poca}) + s$ % Add ray signal to PoCA pixel:
   - 2.6. $\mathbf{I}(\mathbf{p}_{\mathbf{ray}}) := \mathbf{I}(\mathbf{p}_{\mathbf{ray}}) + 1$ % Increment counter for all pixels along path:
3. Next i
4. For $j := 1$ to N^2
   - 4.1. $\boldsymbol{\lambda}(j) := \mathbf{S}(j)/\mathbf{I}(j)/L$ % Compute scattering density estimate
5. Next j

Reflection on the single scattering assumption suggests that the PoCA method should work best for volumes containing small, isolated objects for which that assumption is most valid. In the next section the performance of the algorithm will be investigated in simulated examples.

4.2.2 Simulation Platform for Testing of the 2D PoCA Algorithm

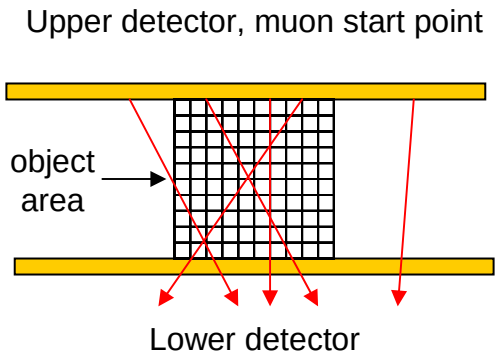

Figure 4.7 Setup for muon scattering simulation and PoCA reconstruction testing.

The PoCA reconstruction algorithm was tested through a simple simulation. The setup for the simulation is illustrated in Figure 4.7. Two "detectors" were implemented, each 300 cm wide and separated by 200 cm vertically. Muons with nominal momentum 3 GeV were emitted from the upper detector location with random starting position and angle uniformly distributed over $\pm\pi/4$ radians from vertical. This angular distribution did not accurately reproduce the cosmic ray muon angular spectrum, but did provide for preferentially vertical orientation. Muon positions and scattered angles were recorded at the bottom detector position. A 100 x 100 cm object area, broken into 10 cm square cells, was centered within the detectors. For these tests, material was placed in the object area with each 10 cm square cell capable of containing a different material, where material was represented by assigning particular scattering density value to elements. Material outside the object area was setup to contain air. For simulation of muon passage, the entire area between the detectors was further broken into 0.1 cm square sub-elements. Muons were tracked through these sub-elements along their path from upper to lower detectors.

For each horizontal layer of sub-elements, proceeding from top to bottom, the position of the muon at the midpoint of that sub-element layer was calculated, and the sub-element containing that point was identified. A random scattering angle was simulated, drawn from a normal distribution with zero mean and variance per Eq. (4.4), using the scattering density and estimated ray path-length for that sub-element. The track of the muon was altered by this computed scattering angle, and then the track was propagated to the next sub-element layer. Simulation proceeded until the track reached the bottom detector. The output of the simulation was the position and angle of muon tracks at the top and bottom detector locations. The accuracy of the simulation was verified by using geometrically simple objects and comparing simulated and theoretical scattering distributions for muons taking various paths through the simulated setup.

4.2.3 Numerical Tests of the 2D PoCA Algorithm

In Section 3.3 an analysis of the segregation of material via scattering density was presented. It was shown that uranium, iron, and concrete possess very different scattering densities from one another. In one minute of exposure about 100 muons will pass through each $(10\text{ cm})^3$ cube of material, and if muon momentum is known, the blocks are easily discriminated from one another via the information carried by the scattered muons. For the first example in this section the PoCA reconstruction method will be applied to a 2D simulation including three $(10\text{ cm})^2$ squares of uranium, iron, and concrete.

An illustration of the object setup is shown in Figure 4.8. The image color reflects object scattering density, where the value for the uranium cube on the left is

78 milliradians^2/cm, the center iron cube has a value of 14, and concrete cube on the right has scattering density of about 2. The remaining cells are filled with the scattering density of air which is about 8 x 10^{-4} milliradians^2/cm. For the simulation, 6000 muons with momentum 3 GeV were emitted from the upper detector, resulting in about 200 muons passing through each cell in the object area (though only 100 muons would pass through the cubes in a typical minute, the number of muons was doubled to achieve the 200 measurements that were used for Section 3.3.1 calculations).

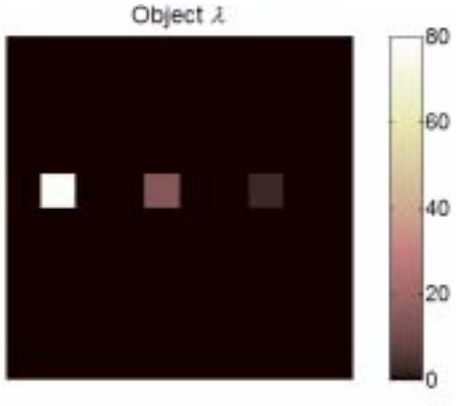

Figure 4.8 Object setup for test case #1. The image reflects object scattering density in milliradians^2/cm.

Results of application of the PoCA reconstruction algorithm to this test case are shown in Figure 4.9. In Figure 4.9(a) the reconstructed scattering density is illustrated to the same scale as the object illustration in Figure 4.8. Reconstructed scattering density values within the pixels containing the uranium, iron, and concrete blocks are about 88, 14, and 2 milliradians^2/cm, respectively. These values are within the confidence limits established in Section 3.3.1, and the blocks are clearly distinguishable from one another. In Figure 4.9(b) the color scale for the reconstruction is quantized to illustrate material classification, wherein a scattering

density of 30 or greater is classified as high Z material, medium Z material is indicated by a scattering density of $5 < \lambda \leq 30$, and low Z material by a scattering density of $.5 < \lambda \leq 5$.

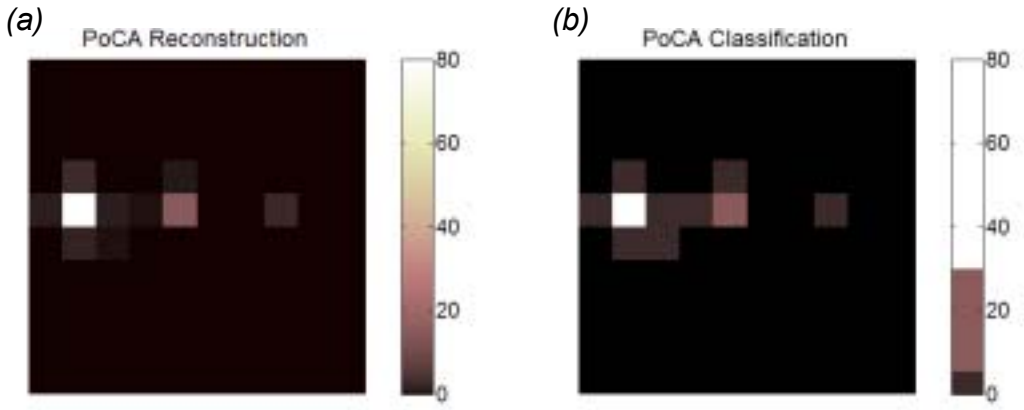

Figure 4.9 PoCA reconstruction of scattering density for test case #1 (a), and reconstructed object classification (b).

Though each block is correctly classified, there are areas around the iron and particularly uranium blocks wherein air has been erroneously classified as low Z material. The source of this blur lies is the localization of scattering to the point of closest approach (or, again, the crossing point of incoming and outgoing ray tracks in the 2D case). Figure 4.10(a) illustrates the some of the ray crossing locations computed for the reconstruction. Though most of these locations are within the pixels containing the three blocks, some of them are outside the blocks. This is due in part to scattering from the background air. However, since scattering does not occur at a point, but is distributed, the ray crossing point may be located outside the scattering material, as illustrated in Figure 4.10(b). Since the ray crossing point must be located along the path of the incoming ray, and muons arrive preferentially vertically, the blur will appear predominantly in the vertical direction. The effect is modest for this first

test case, and if the objective were to identify and locate high and medium Z objects within low Z surroundings, then this result is acceptable.

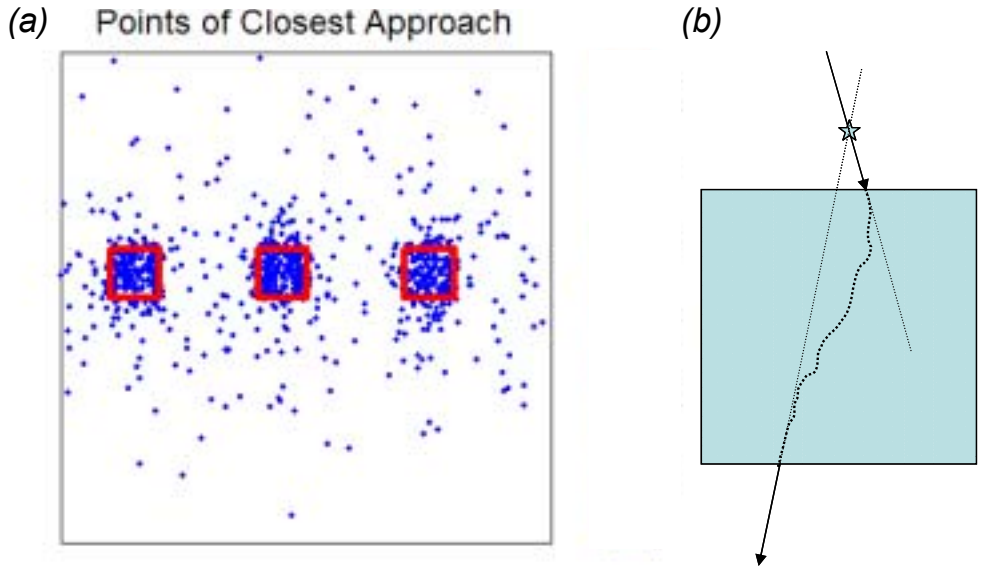

Figure 4.10 Ray crossing locations computed for the reconstruction of test case #1 (a), and illustration of how "erroneous" ray crossing location can occur.

There is another problem caused by the ray crossing or point of closest approach localization method. To illustrate the problem, a new test case was simulated with the three blocks oriented vertically instead of horizontally. The object setup, PoCA reconstruction, and PoCA classification are shown in Figure 4.11. Although the object reconstructed scattering densities for the objects are fairly accurate (84, 11, and 2 for uranium, iron, and concrete, respectively) significant blur between the objects is apparent, and more substantial material misclassification occurs. This blur is partially explained by effect noted above, but the more significant cause has to do with the passing of rays through multiple objects.

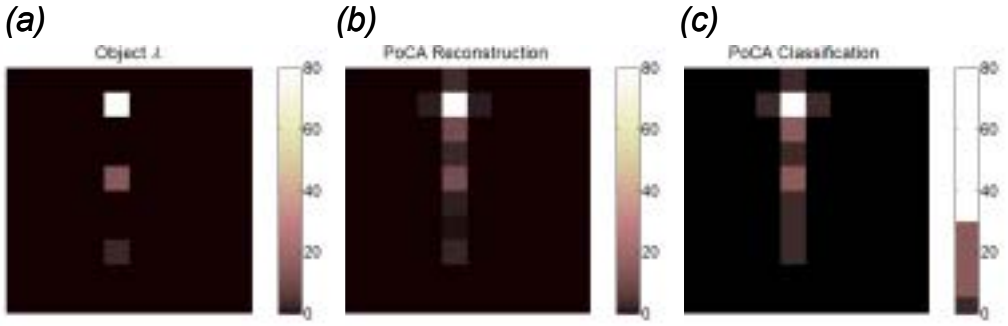

Figure 4.11 Test case #2 object setup (a), PoCA reconstruction (b), and PoCA classification (c).

If a ray passes through two separate pieces of identical material and scattering occurs in each piece, then the ray crossing point will tend to lie between the two objects. In Figure 4.12(a) the ray crossing locations for the test case #2 simulation are shown. The presence of ray crossing locations between the upper two blocks, in particular, is notable. Figure 4.12(b) illustrates the mechanism for erroneous localization of scattering. This effect was first pointed out by a LANL colleague [36].

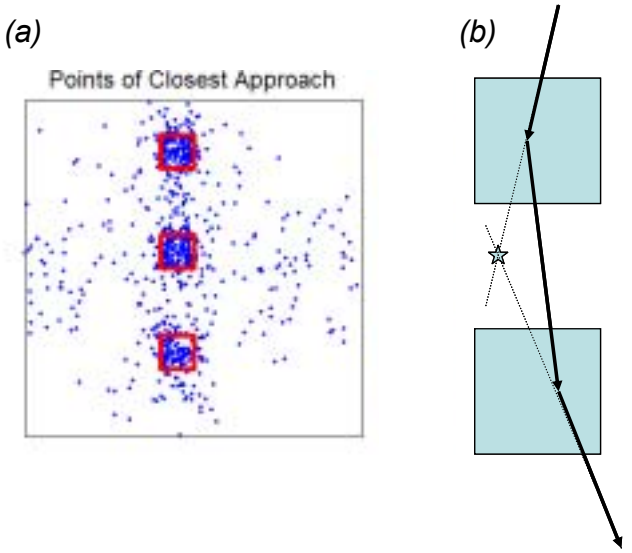

Figure 4.12 Ray crossing locations computed for the reconstruction of test case #2 (a), and illustration of mechanism for erroneous scattering localization.

A final problem with the PoCA method occurs for scenes with single objects sized much larger than the reconstruction cell size. For a ray passing through a segment of material, the mean location of the ray crossing point is the midpoint of the ray segment within the material. Therefore ray crossing points tend to clump towards the center of a large piece of material. Results for test case #3 are shown in Figure 4.13, wherein a single large block of iron was simulated. Cells near the center of the block were erroneously classified as high Z due to the clumping effect.

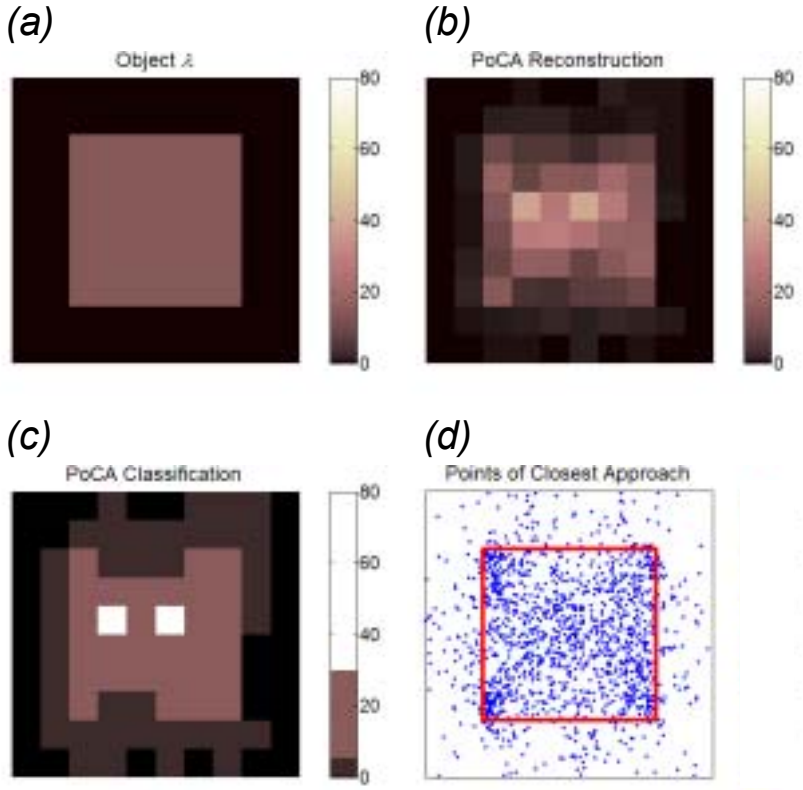

Figure 4.13 Test case #3 object setup (a), PoCA reconstruction (b), PoCA classification (c), and ray crossing locations (d).

4.2.4 Extending the PoCA algorithm to 3D

Extension of the 2D PoCA algorithm to 3D may accomplished in a straightforward manner. Reconstruction pixels become voxels, and an $NxNxN$ voxel

reconstruction volume is established. As discussed in Section 3.2 and illustrated in Figure 3.2, two independent, identically distributed measurements of scattering angle may be made for each ray by measuring scattering into two orthogonal planes (xz and yz, if z is the vertical dimension). The ray signal is therefore defined as:

$$s = \frac{1}{2}\left[\left(\theta_{out} - \theta_{in}\right)_x^2 + \left(\theta_{out} - \theta_{in}\right)_y^2\right] \tag{4.12}$$

Scattering localization is performed as in the 2D method, but the previous ray crossings now truly become points of closest approach, since two rays in 3D need not cross. The ray signal is assigned to the PoCA voxel and zeros to other voxels along the ray path. Estimated scattering density is computed as the mean signal assigned to each voxel. The 3D algorithm is detailed below.

3D PoCA Algorithm

1. Establish an $NxNxN$ grid of $LxLxL$ sized voxels over the object volume, and initialize $NxNxN$ matrices $\mathbf{S}$, $\mathbf{I}$, and $\boldsymbol{\lambda}$. Establish a Cartesian coordinate system in three dimensions with z vertical. Measured data is $\left(x, y, z, \theta_x, \theta_y\right)_{in}$ and $\left(x, y, z, \theta_x, \theta_y\right)_{out}$ for each of M rays.
2. For $i := 1$ to M % loop over rays
   - 2.1. $\left(\left(x, y, z, \theta_x, \theta_y\right)_{in}\right) := \left(\left(x, y, z, \theta_x, \theta_y\right)_{in}\right)_i$ % Get ray data
   - 2.2. $\left(\left(x, y, z, \theta_x, \theta_y\right)_{out}\right) := \left(\left(x, y, z, \theta_x, \theta_y\right)_{out}\right)_i$ % Get ray data
   - 2.3. $s := \left(\left(\theta_{out} - \theta_{in}\right)_x^2 + \left(\theta_{out} - \theta_{in}\right)_y^2\right)/2$ % Compute ray signal
   - 2.4. $v_{poca} := poca3d\left(\left(x, y, z, \theta_x, \theta_y\right)_{in}, \left(x, y, z, \theta_x, \theta_y\right)_{out}\right)$ % Compute the index of the PoCA voxel.
   - 2.5. $\mathbf{v}_{\mathbf{ray}} := raypixels3d\left(\left(x, y, z, \theta_x, \theta_y\right)_{in}, \left(x, y, z, \theta_x, \theta_y\right)_{out}\right)$ % Compute the estimated list of voxels through which the ray passes.
   - 2.6. $\mathbf{S}\left(v_{poca}\right) := \mathbf{S}\left(v_{poca}\right) + s$ % Add ray signal to PoCA voxel:
   - 2.7. $\mathbf{I}\left(\mathbf{v}_{\mathbf{ray}}\right) := \mathbf{I}\left(\mathbf{v}_{\mathbf{ray}}\right) + 1$ % Increment counter for all voxels along path:
3. Next i
4. For $j := 1$ to N^3
   - 4.1. $\boldsymbol{\lambda}(j) := \mathbf{S}(j)/\mathbf{I}(j)/L$ % Compute scattering density estimate

5. Next j

To test the 3D version of the PoCA algorithm the simulation described in Section 4.2.2 was expanded. The setup shown in Figure 4.7 was converted to 3D by adding a third dimension coming "out of the page." In the Cartesian coordinate system the vertical coordinate will be defined as z, increasing downward. An object volume sized at $(100\text{ cm})^3$ was implemented, broken into $(10\text{ cm})^3$ voxels. "Detectors" sized at $(300\text{ cm})^2$ were placed above and below the object volume (in z). Muons with nominal momentum 3 GeV were emitted from the upper detector location with random starting position uniformly covering the top detector area. Muon starting angles in the xz and yz planes were chosen to be uniformly distributed over $\pm\pi/4$ radians. Rays were propagated through the 3D volume by breaking the $(10\text{ cm})^3$ elements into $(.1\text{ cm})^3$ sub-elements and simulating ray scattering within each sub-element in a manner similar to that used for the 2D simulation. Given this geometry, 100,000 simulated muons were required to achieve about 100 muons traversing each $(10\text{ cm})^3$ element in the object volume.

As a numerical test of the 3D algorithm, three $(10\text{ cm})^3$ cubes of material were placed with the object volume. A uranium cube was placed at xyz position (45,45,45), an iron cube at position (75,15,75), and a concrete cube at position (15,75,15). Object locations, points of closest approach and a PoCA reconstruction are shown in Figure 4.14. The points of closest approach are concentrated at the object locations (the plane of PoCA locations outside the objects are due to rays which did not pass through any objects). The voxels containing the uranium, iron and concrete objects, with true

scattering densities of 78, 14, and 2, respectively, had reconstructed scattering densities of 82, 16, and 3, respectively. The signal from the uranium block was slightly distributed to surrounding voxels, causing them to be classified as low-Z although they contained only air. The same effect was noted in 2D test case #1 and the cause was discussed. This example confirms the ability of the PoCA algorithm to locate objects in three dimensions and to identify the Z-classification of those objects via reconstructed scattering density, though some blurring of object boundaries occurs.

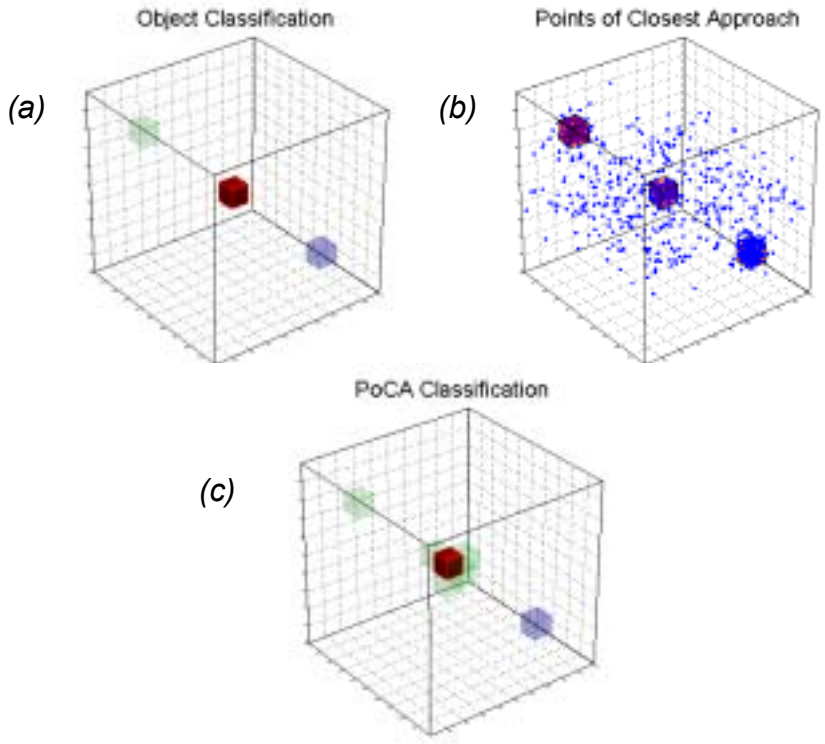

Figure 4.14 3D Test case #4 object classification (a), points of closest approach (b), and PoCA classification (c). Red (darkest) shading signifies high-Z material, blue (medium) shading medium-Z, and green (lightest) shading low-Z.

Of course in test case #4 there was little obstruction of any the objects by other objects. To show that object obstruction in 3D causes the same problems as were

apparent in the 2D case, the next test case involved significant object obstruction. 3D test case #5 is illustrated in Figure 4.15(a), wherein the single blocks of uranium, iron, and concrete were replace with 40 x 40 x 10 cm plates separated by 20 cm vertically. The PoCA points for many rays lie between the objects, as seen in Figure 4.15(b), and significant vertical blurring can be seen in the reconstruction in Figure 4.15(c). Elements between plates were misclassified as low, medium and even high-Z material, though the plates themselves were accurately classified.

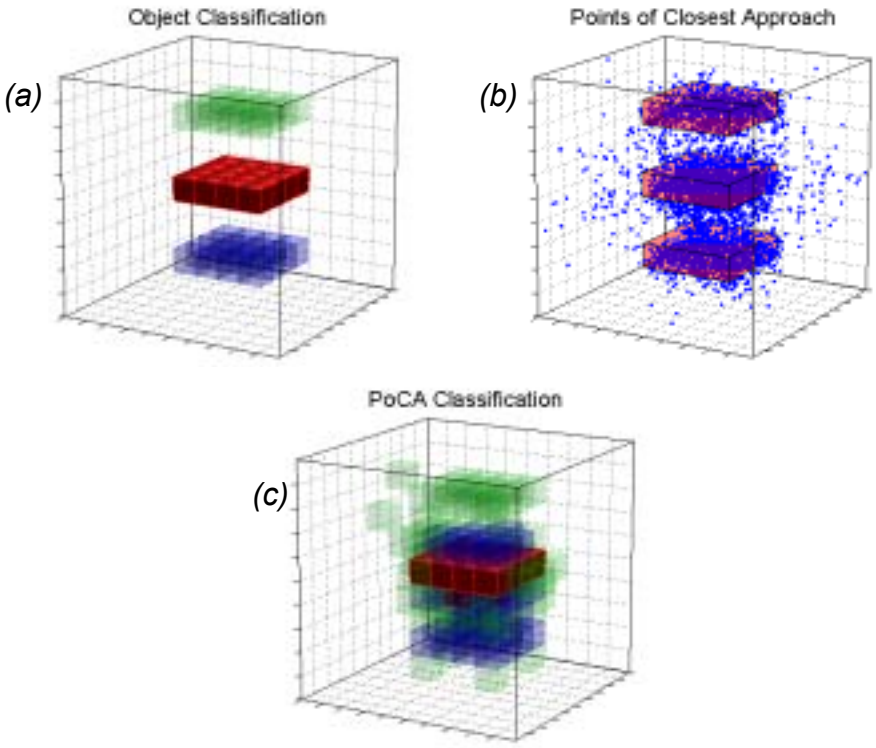

Figure 4.15 3D Test case #5 object classification (a), points of closest approach (b), and PoCA classification (c).

4.2.5 Summary of PoCA Results

In summary, the simulated results of the previous sections illustrate the facility of the PoCA algorithm in reconstructing the location and scattering density of small

isolated objects that are largely unobstructed by other objects. Reconstruction artifacts may be expected when object obstruction exists, where obstruction in the vertical direction is most problematic due to the nature of the cosmic ray flux. Inaccuracies are also seen for objects larger than the reconstruction cell size. These effects limit the application of the PoCA algorithm to scenarios wherein the point scattering assumption is most valid.

However, it is reiterated that the PoCA algorithm was developed as a simple method for reconstruction experimental data for proof of principle of the muon radiography concept in general. Results using the algorithm for this purpose will be discussed in the next chapter. It will also be seen in Chapter 6 that the PoCA algorithm provides a reasonable starting point for more advanced iterative reconstruction techniques.

CHAPTER 5
EXPERIMENTAL PROOF OF PRINCIPLE

The physics underlying cosmic ray muon radiography are well understood. The formation of cosmic ray muons in the atmosphere is based on well documented physics interactions [8]. Technology for the detection of muons has been available since the 1940's [37]. The cosmic ray muon flux at the Earth's surface has been measured by many researchers ([9-13], for example). In Chapter 3 the foundation for discriminating between high, medium and low Z objects by measuring the multiple scattering of muons passing through those objects was laid. Chapter 4 presented the Point of Closest Approach reconstruction algorithm, and suggested via simulated examples the feasibility of reconstructing both the position and scattering density of objects via cosmic ray muon radiography. Given this background it may be argued that cosmic ray muon radiography is quite likely to "work" for the material segregation task suggested herein.

However, it can also be argued that nothing is proven until it is proven experimentally[5]. Hence, an experimental proof of principle was viewed as essential to this effort. The topic of this chapter is the documentation of construction of a small prototype cosmic ray muon radiography prototype, and presentation of results that support the foundation established in Chapters 1-4. Very little funding was available

[5] One of the author's mentors once said, "You can show anything with computer generated cartoons."

for this effort, so the prototype was of small size and minimal functionality (for example, no momentum measurement was implemented). Almost all the components for the experiment were legacy equipment left over from previous experiments at Los Alamos National Laboratory.

5.1 Design of the Experimental Prototype

In Section 3.1 the general concept for cosmic ray muon radiography was presented, as illustrated in Figure 3.1. The minimal setup involves four horizontally oriented detectors, two located above an object volume to establish incoming muon tracks, and two located below to measure outgoing muon tracks. As discussed in Section 3.3.3, additional detectors, coupled with plates of material of known thickness, could be used to measure muon momentum and reduce exposure time required for material segregation. This feature was not implemented in the prototype due to the unavailability of a sufficient number of detectors. The discussion of Section 3.3.2 suggests that material segregation in the absence of muon momentum knowledge is still feasible, it will simply take longer.

Recent work by the PIBETA collaboration at the Paul Scherrer Institute [20] provided a model for the prototype presented herein. The PIBETA team used cosmic ray muons to perform quality control on cesium iodide crystals by tracking muons through the crystals and measuring energy deposition. Though their objectives were quite different from those of this dissertation, their experimental setup was similar to that required herein. Moreover, the PIBETA calorimetry device utilized muon detectors taken from an old spectrometer decommissioned from the Los Alamos Neutron Science Center (LANSCE), and almost identical detectors were available

from the same source for the muon radiography prototype. Indeed, the entire prototype was built using legacy equipment available from previous experiments at LANSCE.

Three major system components were required for the experimental prototype:

- Muon detectors (4x4)
- Front end electronics to capture detector signals.
- Data acquisition

Each of these components will be discussed in turn below.

5.1.1 Muon Detectors

Many different types of detectors can be used to detect charged particles such as muons [37]. Due to their availability, simplicity of readout and history of reliable performance, delay line readout multiple wire drift chambers were selected.

Wire chambers were pioneered by Charpak [38] in the late 1960's, and continue to be used in many applications today [37]. A cross section through a generic wire chamber is shown in Figure 5.1. Anode wires are stretched between two cathode plates and a voltage of a few kV is applied. The resultant field lines are shown. When an ionizing particle passes through the chamber ion pairs are created. The electrons produced drift toward the anode wires. As the electrons get very near the wires and the field strength increases, they are accelerated with sufficient energy to create additional ion pairs and an avalanche results (particularly when the chamber is filled with a counter gas mixture designed to promote ionization). The avalanche of electrons produces a negative pulse on the anode wire. In some wire chambers each anode wire is connected to an amplifier and pulse shaper. In its most primitive form

such a chamber can measure particle position to the spacing of the anode wires. By adding a fast triggering, but non position sensitive detector such as a scintillator and measuring the time between the scintillator signal and the wire chamber pulse, the distance between the particle and the wire can be inferred, improving position resolution. The careful reader might note that when a particle produces a signal on a wire, it is ambiguous which side of the wire the particle was on. This problem can be overcome by interspersing cathode wires between each anode wire and detecting the induced positive pulses on cathode wires to resolve the side to side ambiguity [39]. One may also simply stack two chambers atop one another, with anode wire positions offset by half the anode wire spacing. To measure particle position in two orthogonal coordinates a stack of chambers may be constructed with wire directions oriented in those orthogonal directions.

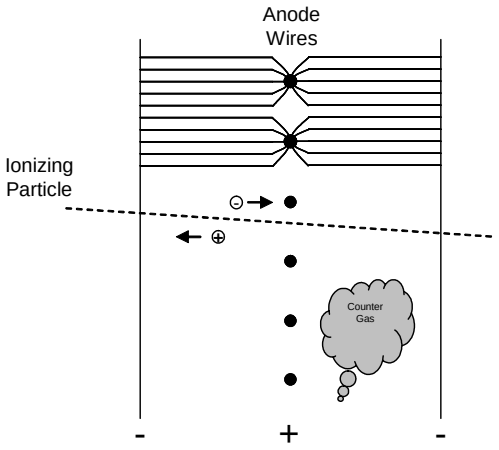

Figure 5.1 Cross-section of a generic multi-wire proportional chamber (from [37], used with permission).

The particular type of wire chamber used herein was a delay line readout chamber, described in detail in [40]. As shown in the schematic of Figure 5.2, the anode wires (20 μm gold plated tungsten) for a wire plane are all connected to a PCB

delay line which produced a signal delay of 2.5 ns·cm^{-1}. Cathode wires (76 μm gold plated, copper clad aluminum) are connected to a common grounded bus. When a pulse occurs on a particular anode wire, the pulse appears at differing times at two readout nodes. The difference between these times may be used to identify the particular anode wire, and the sum of the times (with respect to a prompt trigger from a scintillator detector or equivalent) may be used to measure drift time and infer distance from the wires. More details on the extraction of muon position from these chambers will appear in a later section. By stacking two wire planes atop one another with anode wire positions offset by 4 mm the left right ambiguity may be resolved. The chief advantage of the delay line readout is the reduction in the number of readout channels required (from ~72, the number of anode wires for the chambers used herein, to only two). A potential disadvantage is that only one event can be processed at a time. Indeed, multiple events occurring within about a hundred nanoseconds of one another will be confounded with one another. For this application, however, the event rate should be a few hundred Hz at most in about a square meter of detector area, so this limitation poses little difficulty.

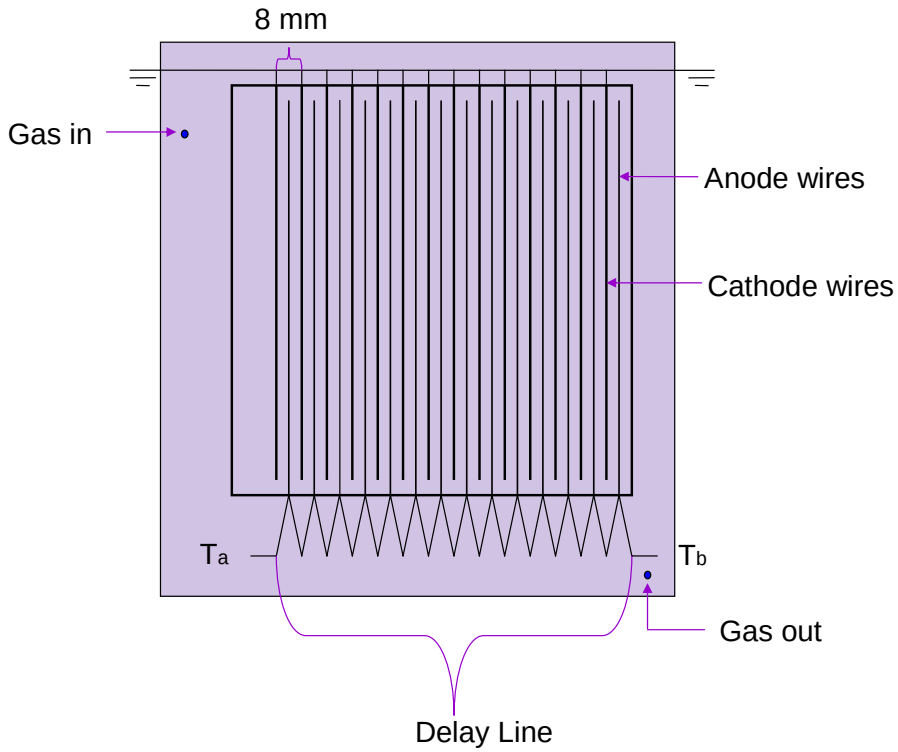

Figure 5.2 Schematic of a delay-line readout drift chamber wire plane.

Four wire planes were stacked, each separated by a ground plane of stretched 6.3 μm aluminized mylar. Two planes with staggered anode wire positions were placed above two more planes with orthogonal wire directions. These planes were enclosed by plates fitted with 51 μm mylar windows to provide for an air tight assembly while minimizing the aggregate scattering density of the chamber itself. Photographs of an individual wire plane and a chamber assembly are shown in Figure 5.3. Outer chamber plates were fitted with external electrical connectors to each plane and gas supply and exhaust ports. The sensitive inner area of the chambers was about $(60\ \text{cm})^2$.

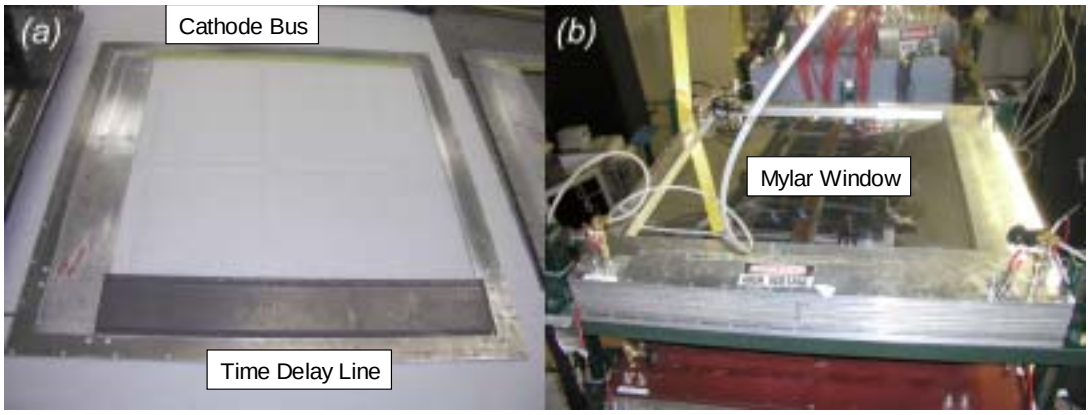

Figure 5.3 Photographs of a time delay line wire plane (a), and a chamber enclosure for such planes (b).

A gas supply system was constructed to flow a specific counter gas mixture through the wire chambers. A mixture of approximately 65% argon, 35% isobutane, and 0.1% isopropyl alcohol was used, duplicating the mixture reported in [20]. This particular gas mixture was empirically identified over years of operation of the chambers in the LANSCE spectrometer to provide semi-optimal signal gain while quenching potential sparking in the chambers and providing some tolerance to impurities in the gas [41]. Acceptable performance was obtained using this gas mixture (see below) and no alterations were made to the mixture in this experiment.

The four wire chambers were assembled into a stack as shown in Figure 5.4. The detectors (C1-C4) were separated by 27 cm vertically. An object platform constructed of plastic (L) was supported by two steel beams (B). Also shown is a tungsten block test object (W), one of the test scenes to be discussed in the results section. Not shown in the figure are two plastic scintillators (prompt, non-position sensitive detectors) placed below the bottom chamber, directly atop one another, to provide a trigger for the system (see Section 5.1.2.2).

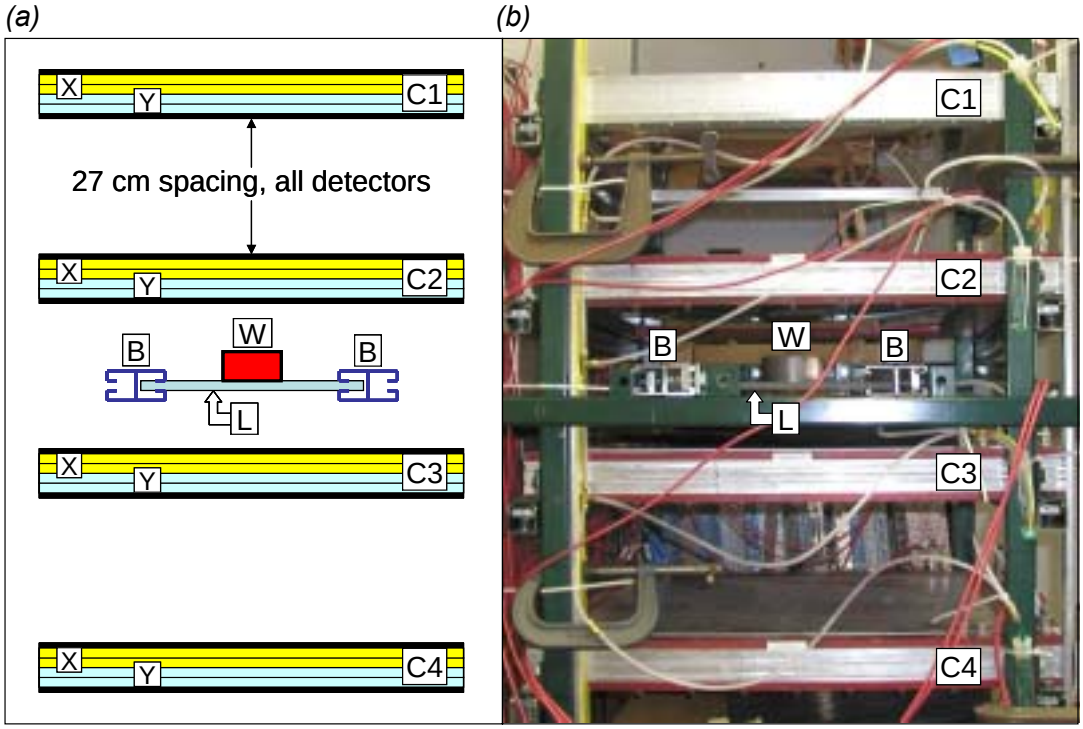

Figure 5.4 Schematic representation (a) and photograph (b) of detector positions and object area in the experimental prototype (see text for explanation of symbols).

Hereafter individual detector planes will be referred to via the following nomenclature. C1X1, for example, refers to the topmost plane measuring position in the X dimension in the topmost wire chamber, where X is the left-right dimension in Figure 5.4. The bottom plane measuring muon position in the Y dimension (into and out of the page in Figure 5.4) in the second from bottom wire chamber would be referred to as C3Y2. The scintillators will be referred to as S1 and S2. Setup and calibration of the detectors will be discussed in Section 5.2.2.

5.1.2 Front end electronics

5.1.2.1 Wire Chamber Signal Processing

With 4 wire chambers, each containing 4 planes with two readout channels on each plane, 32 data channels were required. Again, legacy equipment left over from

previous experiments at LANSCE was used to meet this need. A schematic of the components of signal processing electronics for each channel is shown in Figure 5.5. The signal from each end of each time delay line was fed into a preamp (Phillips Scientific 777 Octal Amplifier 2-50X), then to a leading edge discriminator (Ortec 934 Quad Constant Fraction Discriminator) which converted the analog pulse to a NIM (Nuclear Instrumentation Module) logic pulse. The use of a constant fraction discriminator (CFD) was required since the analog pulse height varied. When a pulse crosses a fixed threshold voltage, the CFD triggers at the point that that analog pulse reaches a specified fraction of full pulse height. This triggering method eliminates the timing walk that would occur with a fixed threshold discriminator. The discriminated NIM signal was delayed by 300 ns in time (to delay the signal sufficiently to allow triggering to occur; see the next section) and then fed into a NIM-ECL logic converter (LeCroy Model 4616 ECL-NIM-ECL Converter), and the ECL signal was finally fed into a CAMAC Crate holding a Time to Digital Converter (TDC) array. The TDC array consisted of LeCroy 4303 Time to FERA (Fast Encoding and Readout ADC) devices, LeCroy 4300 FERA 9-bit ADC's, and a LeCroy 4302 16KB Memory Module which held the data from all 32 channels. The TDC conversion was started with a trigger signal (see next section), and the time to arrival of all 32 channels was read, converted, and stored. The entire TDC array was held within a CAMAC 3988 GPIB Crate Controller which was periodically queried by the PC based data acquisition program (see Section 5.1.3).

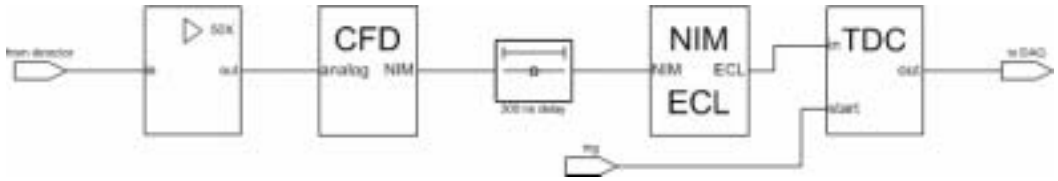

Figure 5.5 Signal flow diagram for muon detector signal processing.

5.1.2.2 Trigger Logic

A usable event occurs when a muon which passes through all four wire chambers and the scintillators which provide a prompt timing signal. To minimize the complexity of the logic the trigger signal was formed from coincidence of the amplified and discriminated signals of both scintillators S1 and S2 (the scintillators tended to be noisy, and using two reduced false triggering, particularly in chamber efficiency testing to be described in Section 5.2.1) and a signal from any plane in the topmost chamber and any plane in the bottommost chamber. The schematic of the trigger logic is shown in Figure 5.6. When a pulse occurs on any chamber plane anode wire a corresponding pulse is induced on the cathode bus for that plane. These cathode signals are much more prompt than the anode signals on the time delay lines, and are so more appropriate for use in the trigger. All of the cathode busses for the four planes in C1 were commonly connected, and this "wired OR" signal was amplified and discriminated with an output pulse width of about 200ns. The same was done for C4. The signal from S1 was amplified, discriminated with an output pulse width of about 200 ns, and then delayed by 64ns to ensure that the S1 signal arrived after the start of both chamber pulses. The S2 signal was amplified, discriminated with a narrow 20 ns output pulse width and then delayed by 80ns to ensure that the S2 signal was the last of the four signals in time. Then all four signals were fed into a

coincidence module which acted as an AND gate. Hence, the S2 signal was the actual prompt timing signal, and the other three signals essentially enabled the trigger. The 1 microsecond veto of subsequent triggers was used to give the TDC array sufficient time to process the delayed chamber signals before another trigger was allowed.

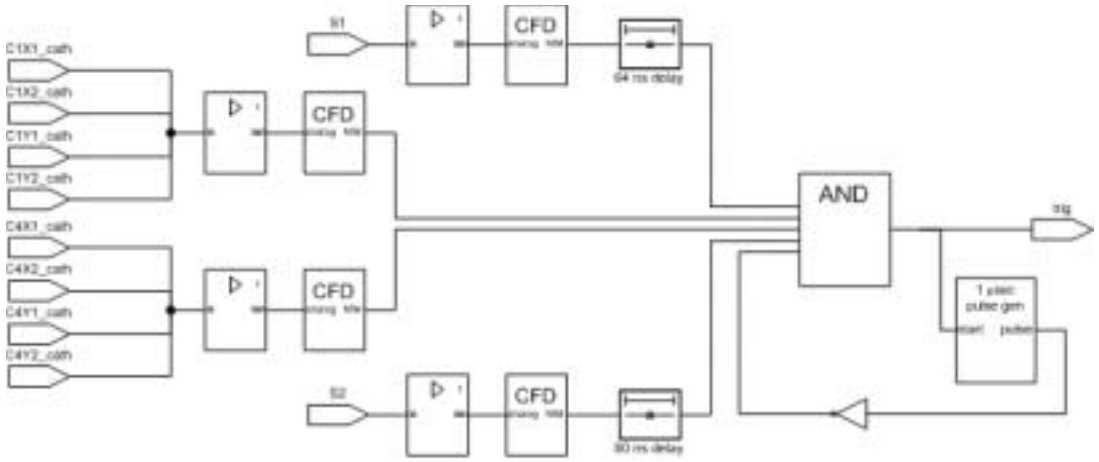

Figure 5.6 Schematic of trigger logic

5.1.2.3 Other Components

The electronics system for the prototype was rounded out with high voltage power supplies for both the wire chambers and scintillators. Various other components (logic gates, counters, timers) were used for setup and debug of the system. A photograph of the electronics racks showing major components is shown in Figure 5.7.

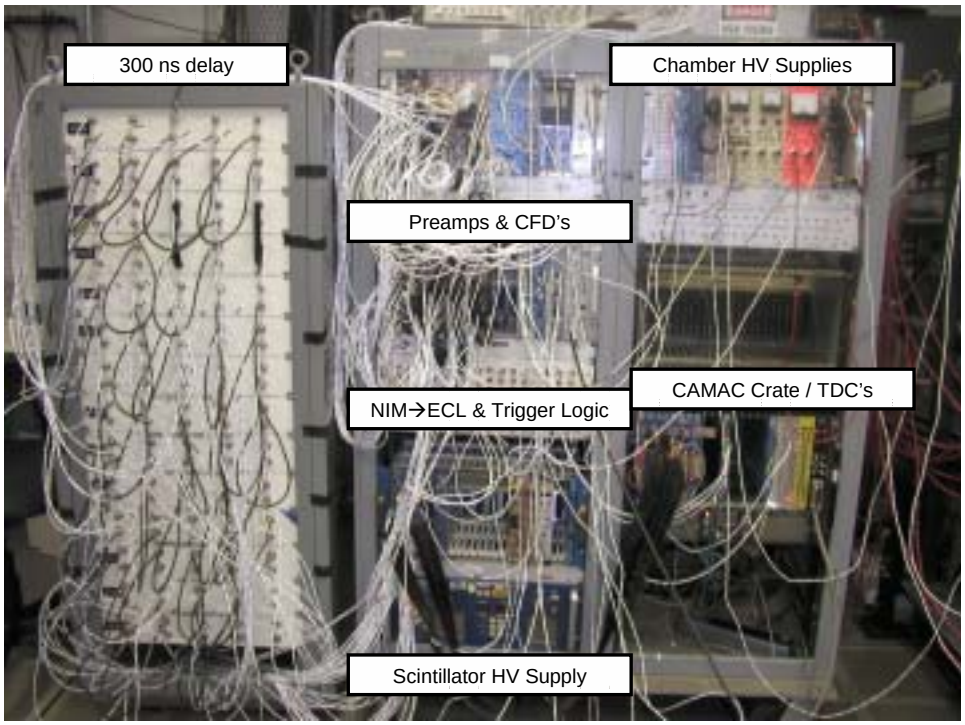

Figure 5.7 Photograph of front end electronics with major system components labeled.

5.1.3 Data Acquisition / Analysis

A PC based data acquisition program (PCDAQ) developed by Gary Hogan of Los Alamos National Lab was used to capture chamber time signals [42]. An earlier version of PCDAQ was used to gather data from the same chambers in their previous application in the LANSCE spectrometer, so the program was easily applied to the muon radiography prototype. The PCDAQ program actually performed the dual role of data acquisition and data analysis, capturing the signal arrival times from the TDC's, and then translating those signals into particle position at each chamber location. More will be said about PCDAQ in the next section. The final output of the program was a text file containing the X-Y positions of muon tracks at the Z

midpoints of each of the four wire chambers. This file was stored for input to reconstruction software.

5.2 Setup and Calibration

Several months of work were required to get the prototype operational. Much of this time was spent correcting subtle problems with the old wire chambers and in resolving signal integrity and timing issues with the electronics. It is not pertinent to dwell on the details of the debugging effort, but highlights of setup and calibration will be described in this section.

5.2.1 Wire Chamber HV Plateau and Efficiency Tests

The first step was to identify the proper operating voltage for the wire chambers. Below a certain plateau voltage, the signal obtained from a muon is roughly proportional to its energy (though not so reliably as to be useful for energy measurement). So as the voltage is reduced from the plateau voltage the level of energy of detectable muons also decreases. Above the plateau voltage the avalanche process within the chamber is at saturation, so signal is largely independent of muon energy. As voltage is raised much above the plateau voltage sparking can occur within the chamber. Power supply current limits prevent damage to the chamber when such sparking occurs, but the power supply trips and data taking is interrupted. The optimal chamber voltage is just above, but not too far above, the plateau voltage.

The plateau voltage can be identified by efficiency testing. To run a chamber efficiency curve, the scintillator pair was placed directly atop a wire chamber to be tested. A denominator signal was defined as the coincidence of signals from both

scintillators, and a numerator signal was defined as the coincidence of signals from both scintillators and the wire chamber:

$$Eff\% = \frac{S1 \bullet S2 \bullet C}{S1 \bullet S2} \times 100\% \tag{5.1}$$

A sample efficiency curve is shown in Figure 5.8, showing about 99% efficiency for a high voltage setting of 2075 V or greater. A high voltage setting of 2100 V was established for all wire planes, and measured efficiencies ranged from 96% to 99.8%.

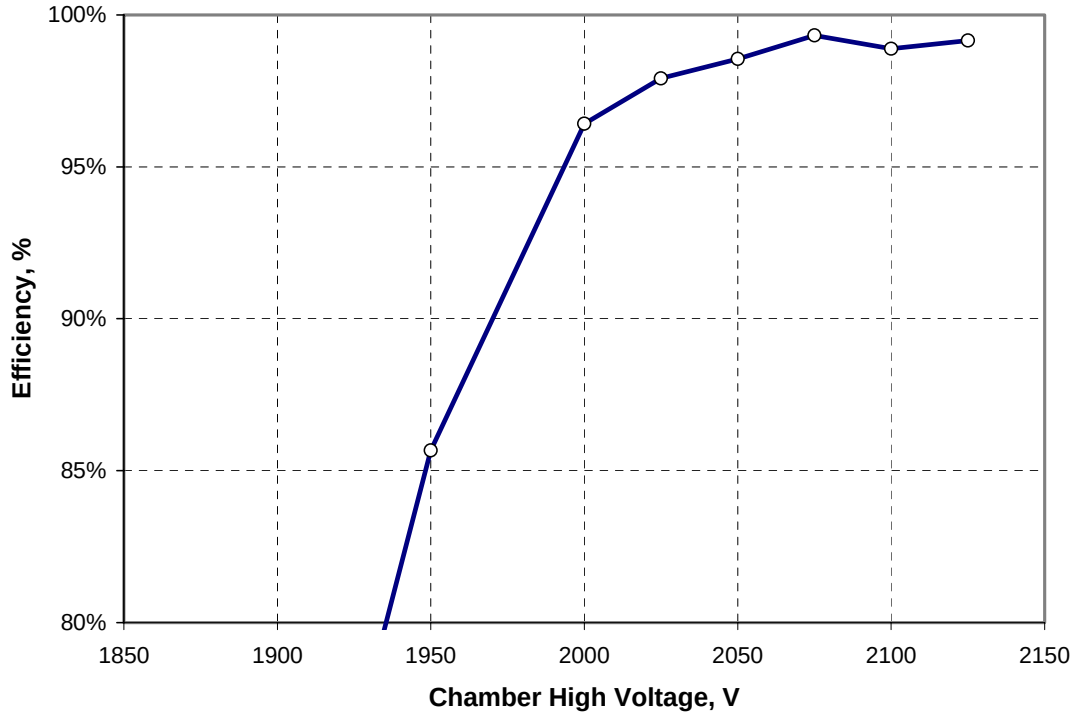

Figure 5.8 Sample Chamber Efficiency Curve

5.2.2 Calibration

To extract a muon position from the arrival time of signal from the two ends a wire plane delay line (call them T_a and T_b) three things must be determined. Upon which wire did the signal appear? This is a function of the difference in times,

$T_a - T_b$. How far away was the track from the wire? This is a function of the sum of times, $T_a + T_b$. Finally, on which side of the signaling wire was the particle? This identification is made by making use of the information from other wire planes. These relationships between times and positions are identified in the calibration process. Additionally, although chambers were physically leveled and aligned with one another in the mounting rack, there was no means for precise alignment of each wire plane. Fortunately PCDAQ provides "trim" parameters that allow for software alignment of wire planes.

Once plateau and efficiency testing had been completed for all 16 wire planes a calibration run was made before installation of the object platform. About 500,000 triggers were collected and these muons provided the dataset for calibration of the prototype. Due to his prior experience and familiarity with PCDAQ, Gary Hogan performed most of the calibration work with only minor assistance from the author. Highlights will be outlined below.

It is easy to see from Figure 5.2 why wire position is closely related to the time difference $T_a - T_b$. A histogram of muon frequency plotted against time difference for a single wire plane for a portion of the calibration run is shown in Figure 5.9. Each peak in the histogram represents a single anode wire. With ideal signal processing these peaks would be impulses, but signal dispersion broadens the peaks somewhat. A built in routine in PCDAQ locates the time difference corresponding to each peak and establishes time difference bins or windows that represent each wire location. This was done for each wire plane.

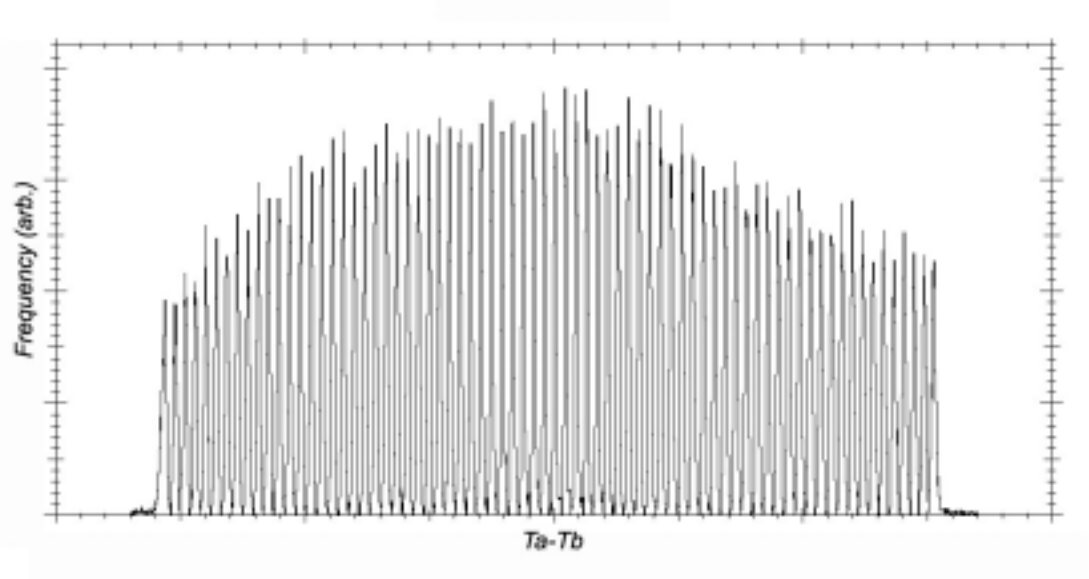

Figure 5.9 Typical histogram of muon frequency vs. time delay line signal time difference.

To establish the distance from a muon track to an anode wire, the relationship between drift time and drift distance must be established. In order to obtain this relationship a procedure described by Breskin [43] was used. The drift time is

$$t_s = T_a + T_b + T_{prop} \tag{5.2}$$

where T_{prop} is the common time required to propagate signals to the DAQ. Next assume that, on average, drift cells are uniformly populated with muons over the drift space s. In other words the distribution of particles in drift space is constant:

$$\frac{dN}{ds} = c \tag{5.3}$$

The distribution of particles in drift time may be expressed in the following expansion:

$$\frac{dN}{dt_s} = \frac{dN}{ds}\frac{ds}{dt_s} = c\frac{ds}{dt_s} \tag{5.4}$$

So

$$s(t_s) = \frac{1}{c}\int_0^{t_s} \frac{dN}{d\tau} d\tau \tag{5.5}$$

is an equation expressing the relationship between drift distance and drift time.

A typical histogram of muon frequency vs. the sum of time delay line signals appears in Figure 5.10. A lookup table of drift distances versus drift times was generated by numerically integrating this histogram and using Eq. (5.5). Of course this procedure relies on the longest measured drift time corresponding to the longest possible drift distance. Close examination of Figure 5.10 reveals a long tail on the right side of the distribution, corresponding to a few events with impractically long drift times / distances. Some data reduction and empirical fine tuning of the drift time inversion was performed by Gary Hogan during the calibration process.

Finally, the left / right ambiguity in track position was addressed by taking the information from all wire planes (above or below the object area) and choosing the combination of left/right decision which provided the lowest RMS error in fitting a straight line to resultant positions. This process was also used to fine tune the drift time inversion and wire position parameters.

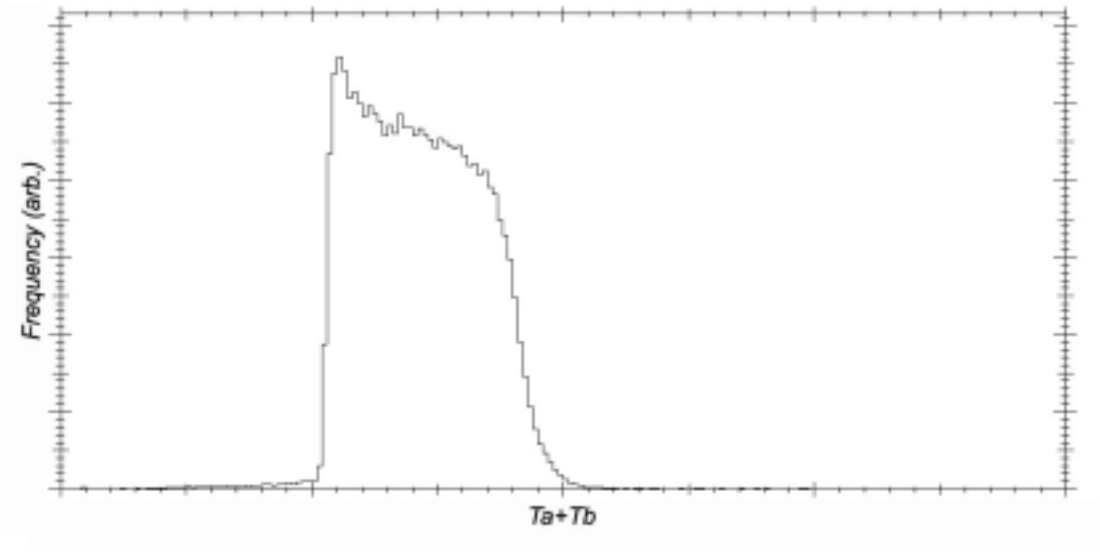

Figure 5.10 Typical histogram of muon frequency versus time delay line signal time sum.

As mentioned above, numerous other minor calibrations were required, including establishing (x, y, z) position of all wire planes and chambers relative to one another, correction for rotations of chambers relative to one another, etc.

5.2.3 Chamber Resolution Estimation

The resolution of each wire plane was estimated by fitting a straight line to positions determined by all other planes, leaving out the plane to be analyzed, and comparing the position of that line projected to the plane location to the position indicated by the plane itself. Via this process an average position resolution of about 220 μm RMS for a single wire plane was obtained. Since the average of two wire planes are used to express position for each wire chamber z location, a position resolution of about $220/\sqrt{2} \cong 160$ μm RMS is expected. With a 27 cm chamber spacing, this position resolution should translate into $\tan^{-1}\left(.0160\sqrt{2}/27\right) \cong 0.8$

milliradians resolution on incoming and exiting muon angle, or $0.8\sqrt{2} \cong 1.1$ milliradian RMS resolution on individual muon scattering angle.

5.2.4 Trigger Rate

The $(30\ \text{cm})^2 = 900\ \text{cm}^2$ scintillator area was the limiting factor in the system, and using the nominal muon flux rate of 10,000 muons$\cdot m^{-2} \cdot min^{-1}$, the muon rate through the scintillators should be around 900 muons per minute at sea level, and as much as 40% higher, or 1260 muons per minute, at the Los Alamos altitude of about 2100 meters [13] . The system trigger, as described in Section 5.1.2.2, demanded coincidence between the top and bottommost wire chambers and the scintillators, reducing the acceptance angle of the instrument to a degree dependant on the placement of the scintillators. With the scintillator pair placed in the object area the measured trigger rate was about 750 counts per minute. With the scintillators placed about 140 cm below the topmost wire chamber the count rate was about 200 counts per minute, illustrating the dramatic effect of solid acceptance angle on the trigger rate. The later position was used for the radiography of the test objects detailed below.

5.3 Experimental Radiography Results

Results for three test objects will be presented in this section. Results from the first test object, a tungsten cylinder, were analyzed to confirm expectation from theory. Because of the complexities of the geometry of the prototype, validation of the results purely against theory was difficult. Instead, a computerized simulation of the system was developed by Konstantin Borozdin, one of the author's LANL colleagues. The geometry of the detectors and object platform in the prototype and the

size and composition of the test object were reproduced in the simulation. The cosmic ray muon momentum and angular flux were reproduced by use of the Blanpied muon generator [14]. The passage of these muons was tracked through the system with multiple Coulomb scattering simulated as muons passed through simulated material. The output of the simulation was muon position at the z midpoint of each of the four detector locations. For analysis, those positions were "blurred" by adding a Gaussian random variable with zero mean and a standard deviation of 0.016 cm, reproducing the measured position resolution of the experimental unit (see Section 5.2.3). The experiment and the simulation were "cross validated" against one another. More details on the simulation are presented in publications by the collaboration [2, 7, 35, 44]. The validation and reconstruction results presented in the subsequent sections are the work of the author.

5.3.1 Tungsten Cylinder Test Object

5.3.1.1 Scattering Analysis and Simulation Cross-Validation

The first test object to be radiographed was a tungsten cylinder, 11 cm in diameter and 5.7 cm in height. This object appears in the schematic and photograph of Figure 5.4. Tungsten has a radiation length L_{rad} of about .35 cm, about the same as that of uranium (.32 cm). The object was placed in the prototype and data from about 100,000 triggers was gathered. Some reduction was applied to this dataset. Events with scattering angle of greater than 250 milliradians were discarded. Events wherein the distance of closest approach between incoming and outgoing rays was greater than 5 cm were discarded. Both of these cuts correspond to physically improbable events,

potentially caused by near simultaneous muons, very low energy cosmic ray electrons, or electrons released from objects via the passage of muons. In any event, these two cuts removed only a fraction of a percent of the data.

In the first attempt to visualize results, another angle cut was applied. Rays with less than 10 milliradians of scattering (in space) were discarded, and the incoming tracks of the remaining rays were projected to the z location of the midpoint of the tungsten cylinder. Then a histogram was made of the $x - y$ locations of these rays. One would expect a predominance of the highly scattered rays to pass through the tungsten object. An image of the histogram, with $(1\text{ cm})^2$ position bins, appears in Figure 5.11. The tungsten cylinder is clearly visible. The beams that support the plastic object platform may also be seen. This hazy image was the first experimental confirmation that multiple scattering muon radiography worked and was the source of a great deal of excitement.

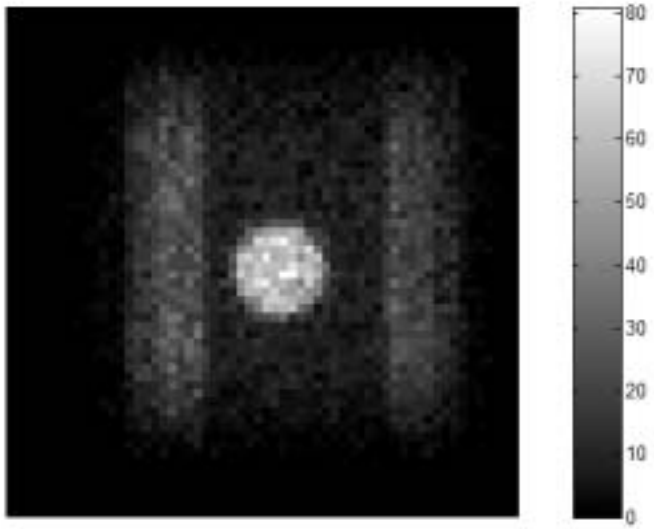

Figure 5.11 First image of experimental radiography of tungsten block test object (see text).

The intensity of Figure 5.11 does not directly represent object scattering density, only the density of rays which scattered more than 10 milliradians. As mentioned above, to validate the actual scattering distributions through the object and the background the Borozdin simulation was used. A simulated run of 100,000 muons was made. At the projected plane at the center of the tungsten cylinder three regions were defined, as illustrated in Figure 5.12: T) a region representing rays passing through the tungsten, S) an thin strip representing rays passing through the left steel beam, and B) an region representing background scattering. Rays passing through each of these regions in both experimental and simulated runs were tagged.

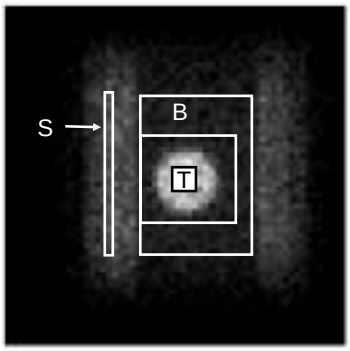

Figure 5.12 Regions defining T) tungsten, S) steel beam, and B) background scattering for analysis

Histograms of scattering into x and y planes (combined) for rays passing through each region for the experiment and simulation are shown in Figure 5.13. The distributions from experiment and simulation are qualitatively quite similar for all three regions. The experimental distributions show somewhat heavier tails, particularly in the background distribution. This may be due to the presence of lower momenta muons than were generated by the Blanpied generator, which does not generate muons with momenta lower than 300 MeV. As has been previously discussed, the true multiple scattering distribution is expected to have heavier tails than a Gaussian distribution, but not to the extent seen in this data. The cause and effect of these tails is an item of future research. For the purposes of this document these results were taken as successful cross-validation of experimental and simulated methods.

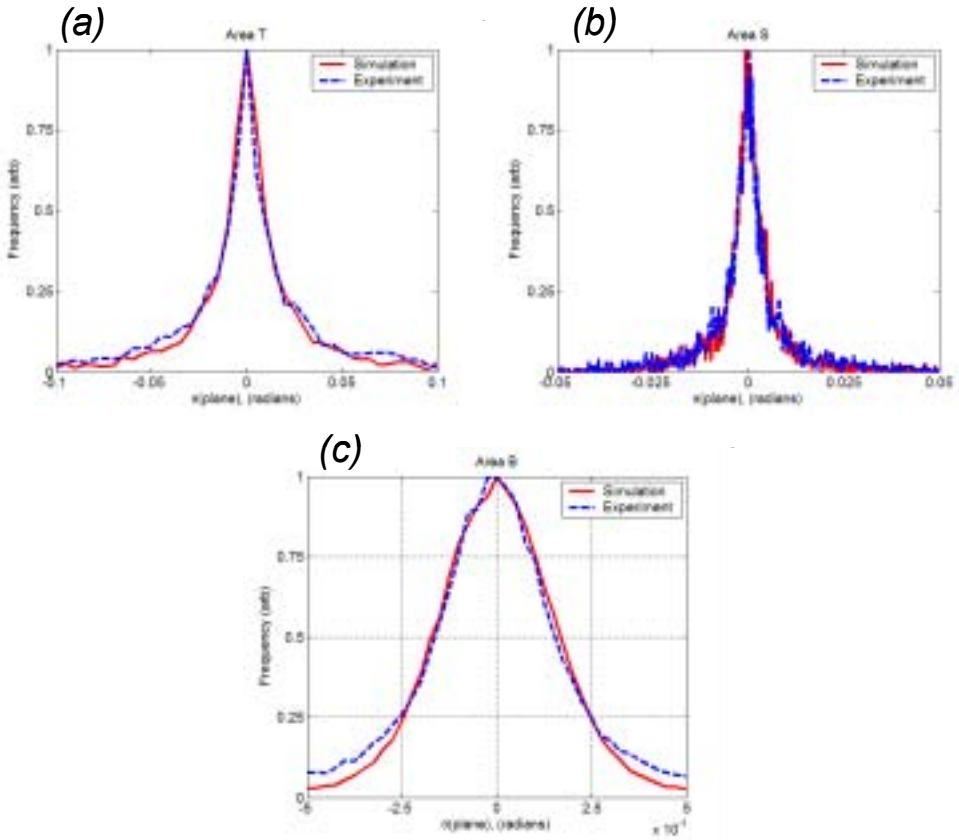

Figure 5.13 Ray scattering distributions for rays passing through region T (a), region S (b), and region B (c).

5.3.1.2 PoCA Reconstruction

In Chapter 4 the Point of Closest Approach (PoCA) reconstruction method was presented. The discussion and simulated examples of Chapter 4 were made assuming voxel sizes of $(10\text{ cm})^3$ and one minute exposure resulting in about 100 muons passing through each voxel. Knowledge of muon momentum was also assumed. These factors allowed for the segregation of high, medium, and low Z materials from one another. For the experiment and object described in this chapter a smaller voxel size is required to resolve any detail in the objects. A voxel size of $(1\text{ cm})^3$ was used for reconstruction of the tungsten cylinder data for an object volume with (x, y, z)

dimensions of 60 x 60 x 30 cm. Even 100,000 muons results in less than 30 muons passing through each voxel[6]. With such sparse sampling and no knowledge of momentum the quantified radiography of Chapter 4 is not possible. Nonetheless, it will be shown that reconstruction showing the structure of objects and their relative scattering densities is possible.

The 3D PoCA algorithm described in Section 4.2.4 was applied to the experimental dataset. Since muon momentum varied but was not known, step 2.3 of the algorithm, the calculation of the signal from each ray, was modified per the discussion in Section 3.3.2. The signal was calculated as

$$s = \frac{1}{2}\left(\theta_x^2 + \theta_y^2\right)\left(\frac{\hat{p}}{p_0}\right)^2 \tag{3.7}$$

where θ_x and θ_y are the plane scattering angles of the ray and p_0 is the nominal muon momentum of 3000 MeV. The muon momentum estimate $\hat{p}$ was set to the constant value of 1427 MeV determined in the Section 3.3.2 analysis to provide unbiased scattering density estimates using the Blanpied muon generator.

Due to the large number of voxels a different method of visualizing results was used. Whereas in Chapter 4 voxels were colored according to the level of reconstructed scattering density, this method of visualization is too cluttered with a large number of voxels. Instead, 3D isosurfaces were drawn about volumes containing groups of voxels at various scattering density levels. Using the scattering

[6] This experiment was actually performed before the analyses of Chapters 3 and 4 were complete to the extent that the effect of number of particles on material segregation was known.

density levels defined in Chapter 4, volumes with a scattering density of 30 or greater were classified as high Z material, medium Z material was indicated by a scattering density of $5 < \lambda \leq 30$, and low Z material by a scattering density of $.5 < \lambda \leq 5$. A three dimensional perspective view of isosurfaces for the PoCA reconstruction are shown in Figure 5.14.

The shape of the tungsten cylinder and steel supporting beams are remarkably well reconstructed. At first glance it might appear that object classification was also fairly accurate. However, the steel beams were of I-beam construction with only a 3 mm wall thickness, whereas they appear as large medium Z beams with hints of high Z material in the center in the reconstruction. There is also a haze of low-Z material appearing between the beams, around the tungsten cylinder. However, with such sparse sampling and no momentum knowledge these results were quite encouraging.

A reconstruction of the simulated radiography of the tungsten cylinder appears in Figure 5.15. Results are similar to that of the experiment, though less noisy and with more accurate reconstruction of beam composition. The similarity in distribution widths in Figure 5.13 would suggest that the greater noise level in the experimental reconstruction is caused by the heavy tails. Again, this is a item for future research.

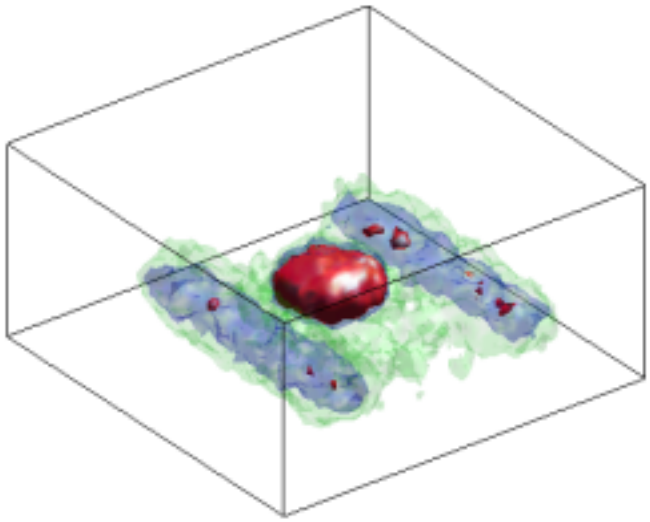

Figure 5.14 PoCA reconstruction of the tungsten cylinder (experimental data). Red (darkest) areas indicate high Z material, blue (medium shading) indicates medium Z material, and green (lightest shading) low Z material.

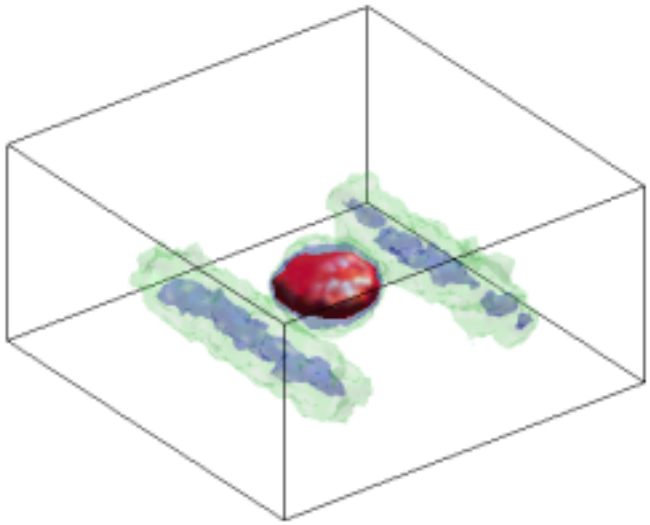

Figure 5.15 PoCA reconstruction of the tungsten cylinder (simulation).

5.3.1.2 PoCA Reconstruction Optimized for Visual Appearance

Purely for demonstration purposes, some heuristic fine tuning of the PoCA algorithm and visualization procedure was performed. To highlight the structure of the higher Z objects and remove background haze an angle cut was applied where only rays scattering to more than 5 milliradians (in space) were processed. A smoothing process developed by Bill Priedhorsky, a LANL colleague of the author's, was applied [7]. This smoothing process spread each ray signal over voxels according to the uncertainty in calculating the point of closest approach given the detector position resolution. The data was visualized using 11 isosurfaces with color value decreasing and transparency increasing with decreasing isosurface level. Application of these heuristics prohibits any sort of quantified radiography, but produced visually impressive reconstructions. Reconstructions so enhanced for aesthetic appearance are shown Figure 5.16.

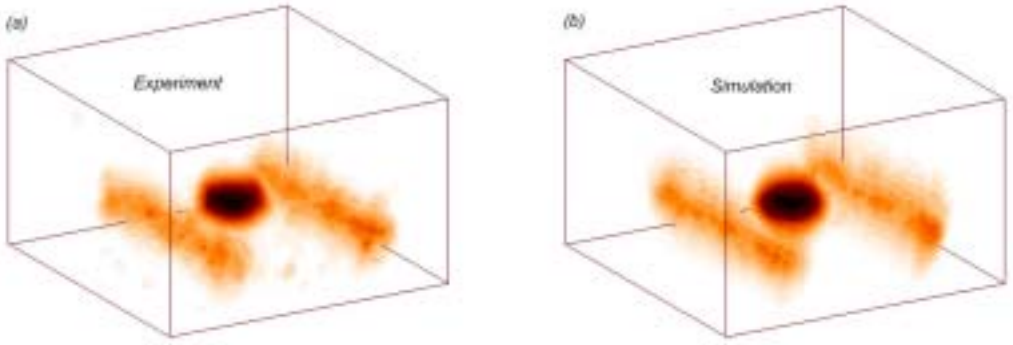

Figure 5.16 PoCA Reconstructions of tungsten cylinder; experiment (a) and simulation (b), with heuristic modification to improve appearance (see text).

5.3.2 Additional Test Objects

Experimental radiographs were produced of two more test objects. The first was a small steel c-clamp, and the second was the letters "LANL" built from 1 inch square

lead stock. To reproduce the fine detail in these objects, the voxel size was reduced to $(0.5\ \text{cm})^3$. Once again, data from 100,000 muons was gathered. No attempt was made at quantified radiography or simulation of these small objects. A reconstruction (with heuristic enhancements) and photograph of the c-clamp object appears in Figure 5.17. The accuracy of the object detail in the reconstruction is remarkable. The intensity levels in this radiography are only relative, not absolute as in Figures 5.14 and 5.15. Hence, the c-clamp and steel beams, which are of similar composition and thickness, have similar intensity in the image.

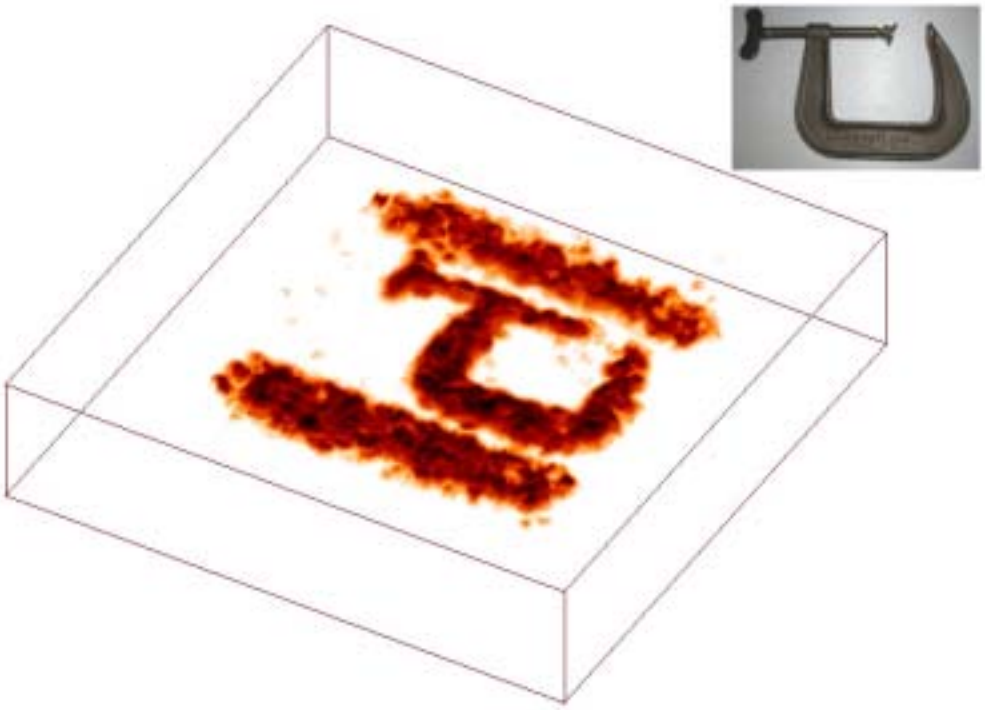

Figure 5.17 Aesthetically enhanced PoCA reconstruction of a c-clamp, made from 100,000 experimentally gathered muons.

A reconstruction of the LANL test object is shown in Figure 5.18. Once again, the detail in this heuristically enhanced reconstruction is impressive. Because the

letters are made of high-Z material they show up with relatively greater intensity than the thin medium Z beams in the image.

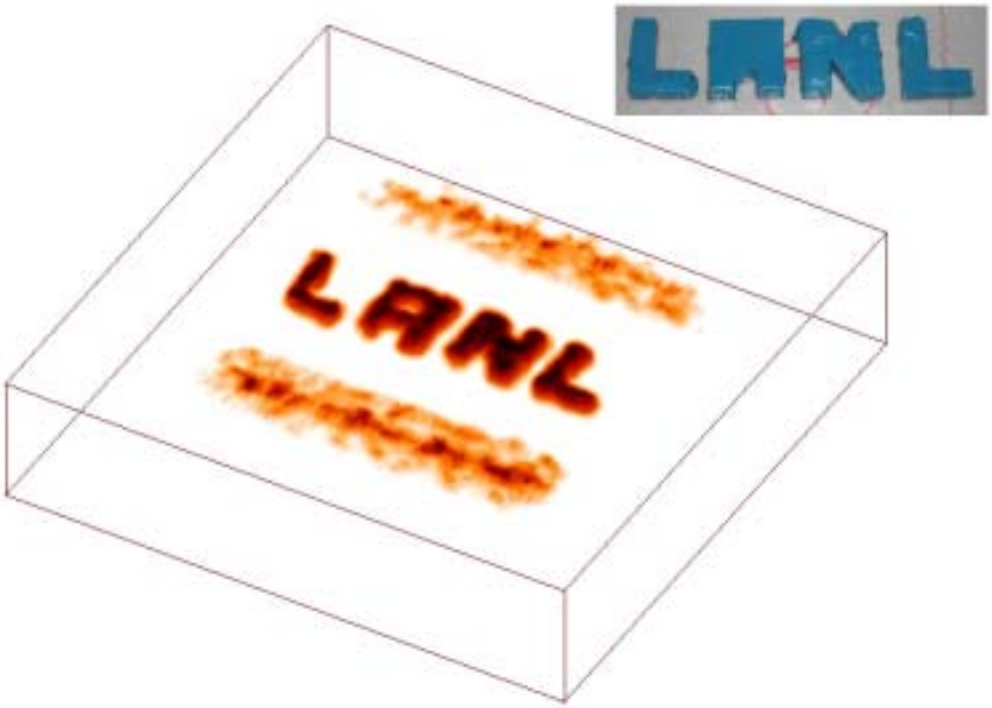

Figure 5.18 Aesthetically enhanced PoCA reconstruction of the letters "LANL" constructed of 1" lead stock, made from 100,000 experimentally gathered muons.

5.4 Summary

The primary objective of the experimental prototype was to prove the basic validity of the cosmic ray muon radiography concept. As has been stated, limited funding was available for this effort, so some concepts, such as muon momentum measurement by multiple scattering, were not implemented. The lack of momentum knowledge, coupled with the small size of the detectors, prohibits validation of the "one-minute material discrimination" referred to in previous chapters. However, these experimental results do serve to prove that the basic concept is valid, that the multiple

scattering of cosmic ray muons is a viable information source for radiography, and that the PoCA reconstruction method works for identifying the location, structure, and relative Z-level of objects.

CHAPTER 6
MAXIMUM LIKELIHOOD RECONSTRUCTION

In Chapters 2 and 4 the framework for algebraic or iterative tomographic reconstruction was examined. It was shown that direct application of these methods is not possible due to the inherently stochastic nature of the multiple scattering information source. However, by marrying the algebraic framework with a statistical model of the information source and applying maximum likelihood methods, a fully tomographic reconstruction algorithm for cosmic ray muon multiple scattering radiography was developed. That development and results from the algorithms are presented in this chapter.

6.1 Maximum Likelihood Tomographic Reconstruction using Scattering Angle Information

In this section a tomographic algorithm using ray scattering as an information source will be developed, based on the method of maximum likelihood. This algorithm will be termed the MLS (Maximum Likelihood Scattering) algorithm.

6.1.1 The MLS Reconstruction Framework

In Section 4.1.1 a framework for discrete tomographic reconstruction for deterministic ray signals was presented. This concluded with a system of linear equations:

$$\mathbf{s} = \mathbf{W}\hat{\mathbf{f}} \tag{6.1}$$

where $\hat{\mathbf{f}}$ is a vector of estimates of a discrete version of an object characteristic function, $\mathbf{W}$ is a matrix of weights that describe the estimated path of rays through an object area, and $\mathbf{s}$ is a vector containing measured signal values of the rays. In Section 4.1.2 a framework for tomographic reconstruction for the stochastic multiple Coulomb scattering (MCS) signal was started. It was shown that, for a given ray i with nominal momentum:

$$\sigma_{s_i}^2 = \sum_{j=1}^{N} L_{ij}\lambda_j \tag{6.2}$$

where the ray signal s_i is the scattering angle of ray, L_{ij} is the estimated path length of the ray within the j^{th} of N cells, and λ_j is the scattering density of material within cell j. Scattering density was defined in Chapter 3 as the mean square scattering angle expected for rays passing through a unit depth of material. Therefore Eq. (6.2) is an expression for the variance of the approximately normally distributed, zero mean ray signal s_i. For notational simplicity define $v_i = \sigma_{s_i}^2$, and Eq. (6.2) may be rewritten as a system of linear equations in terms of scattering density estimates:

$$\hat{\mathbf{v}} = \mathbf{L}\hat{\boldsymbol{\lambda}} \tag{6.3}$$

where $\mathbf{L}$ is a matrix whose i^{th} row contains the ray cell path lengths for the i^{th} ray. Eq. (6.3) is of similar form to Eq. (6.1), but in Eq. (6.3) the left side of the equation represents the *variance of ray signals* (for a given scattering density estimate $\hat{\boldsymbol{\lambda}}$) rather than the *ray signals themselves*.

In order to seek a reconstruction for the scattering density vector, an expression which relates the ray signals to the variances of Eq. (6.3) is required. This may be

accomplished by writing the conditional probability of the signal for the i^{th} ray in terms of the variance estimate:

$$P\left(s_i|\hat{v}_i\right)=\frac{1}{\sqrt{2\pi\hat{v}_i}}\exp\left(-\frac{s_i^2}{2\hat{v}_i}\right) \tag{6.4}$$

The higher this probability, the more congruent the scattering density estimate is with the signal of the i^{th} ray. Each ray is independent, so for the entire data set of M rays:

$$P\left(\mathbf{s}|\hat{\mathbf{v}}\right)=\prod_{i=1}^{M}P\left(s_i|\hat{v}_i\right) \tag{6.5}$$

and the higher this probability, the greater the congruency between the scattering density estimate and the aggregate measured ray signals. Using the method of maximum likelihood, an optimal estimate in the sense of maximizing that congruency might be expressed as

$$\hat{\boldsymbol{\lambda}}^{*}=\underset{\hat{\boldsymbol{\lambda}}}{\arg\max}\,P\left(\hat{\boldsymbol{\lambda}}\middle|\mathbf{s}\right) \tag{6.6}$$

Using Bayes Law of Conditional Probability

$$\hat{\boldsymbol{\lambda}}^{*}=\underset{\hat{\boldsymbol{\lambda}}}{\arg\max}\,\frac{P\left(\mathbf{s}|\hat{\boldsymbol{\lambda}}\right)P\left(\hat{\boldsymbol{\lambda}}\right)}{P\left(\mathbf{s}\right)} \tag{6.7}$$

The probability of the given measured dataset, $P(\mathbf{s})$, is 1. If some prior knowledge of the nature of objects were assumed, that knowledge could be incorporated through some expression for $P\left(\hat{\boldsymbol{\lambda}}\right)$, but for now all objects will be assumed to be equally probable, and the optimal estimate reduces to:

$$\hat{\boldsymbol{\lambda}}^{*}=\underset{\hat{\boldsymbol{\lambda}}}{\arg\max}\,P\left(\mathbf{s}|\hat{\boldsymbol{\lambda}}\right)=\underset{\hat{\boldsymbol{\lambda}}}{\arg\max}\,P\left[\mathbf{s}|\mathbf{v}\left(\hat{\boldsymbol{\lambda}}\right)\right] \tag{6.8}$$

To obtain this optimal scattering density estimate, one may proceed by taking the log of both sides of Eq. (6.5).

$$LP \equiv \ln\left[P\left(\mathbf{s}|\hat{\mathbf{v}}\right)\right] = \sum_{i=1}^{M} \ln\left[P\left(s_i|\hat{v}_i\right)\right] \tag{6.9}$$

$$LP = \sum_{i=1}^{M}\left[-\frac{1}{2}\ln\left(2\pi\right) - \frac{1}{2}\ln\left(\hat{v}_i\right) - \frac{s_i^2}{2\hat{v}_i}\right] \tag{6.10}$$

$$LP = -\frac{1}{2}M\ln\left(2\pi\right) - \frac{1}{2}\sum_{i=1}^{M}\left[\ln\left(\hat{v}_i\right) + \frac{s_i^2}{\hat{v}_i}\right] \tag{6.11}$$

Maximization of the log probability will result in maximization of probability. Only the right term in Eq. (6.11) varies with the scattering density estimate. Maximizing LP is equivalent to minimizing this right hand term. The optimization problem may thus be defined as:

$$\hat{\boldsymbol{\lambda}}^{*} = \underset{\hat{\boldsymbol{\lambda}}}{\arg\min} \sum_{i=1}^{M}\left[\ln\left(\hat{v}_i\right) + \frac{s_i^2}{\hat{v}_i}\right] = \underset{\hat{\boldsymbol{\lambda}}}{\arg\min} \sum_{i=1}^{M}\left[\ln\left(\mathbf{L}_\mathbf{i}\hat{\boldsymbol{\lambda}}\right) + \frac{s_i^2}{\mathbf{L}_\mathbf{i}\hat{\boldsymbol{\lambda}}}\right] \tag{6.12}$$

where $\mathbf{L}_\mathbf{i}$ denotes the i^{th} row of the path length matrix $\mathbf{L}$.

For a realistic solution some constraint must be imposed on the solution of Eq. (6.12). Negative values for scattering density make no physical sense, so the solution must have non-negative values. In fact, it is reasonable to impose the constraint that the scattering strength vector contain no elements with a value less than that of the scattering density of air. With this constraint the minimization problem may be written:

$$\hat{\boldsymbol{\lambda}}^{*} = \underset{\hat{\boldsymbol{\lambda}}}{\arg\min} \sum_{i=1}^{M}\left[\ln\left(\mathbf{L}_\mathbf{i}\hat{\boldsymbol{\lambda}}\right) + \frac{s_i^2}{\mathbf{L}_\mathbf{i}\hat{\boldsymbol{\lambda}}}\right] \quad \text{such that } \hat{\lambda}_j \geq \lambda_{air} \text{ for all } j \tag{6.13}$$

6.1.2 The 2D MLS Reconstruction Algorithm

Eq. (6.13) is the constrained minimization problem to be solved for stochastic tomographic reconstruction. Normalizing for ray count, the cost function for a given scattering density estimate $\hat{\boldsymbol{\lambda}}$ may be written as:

$$F\left(\hat{\boldsymbol{\lambda}}\right)=\frac{1}{M}\sum_{i=1}^{M}\left[\ln\left(\mathbf{L}_i\hat{\boldsymbol{\lambda}}\right)+\frac{s_i^2}{\mathbf{L}_i\hat{\boldsymbol{\lambda}}}\right] \tag{6.14}$$

Any suitable minimization routine may be used to find a solution which minimizes this cost function[7]. For the examples reported in this chapter the large scale algorithm embedded into the MATLAB constrained minimization function *fmincon* was used [45]. This algorithm is a Newton method and so makes use of the Jacobian (gradient) and Hessian (second derivatives) of the function to be minimized. Derivation of the Jacobian and Hessian matrices may be found in Appendix C. Most of the work is done by the minimization algorithm, but the steps of the 2D MLS algorithm are outlined below.

2D MLS Algorithm

1. Establish an NxN grid of LxL sized pixels over the object area. Establish a Cartesian coordinate system with x horizontal, y vertical. Measured data is $\left(x_{in}, y_{in}, \theta_{in}, x_{out}, y_{out}, \theta_{out}\right)$ for each of M rays.
2. For $i := 1$ to M % loop over rays
   2.1. $\left(x_{in}, y_{in}, \theta_{in}, x_{out}, y_{out}, \theta_{out}\right) := \left(x_{in}, y_{in}, \theta_{in}, x_{out}, y_{out}, \theta_{out}\right)_i$ % Get ray data
   2.2. $\mathbf{s}(i) := \left(\theta_{out} - \theta_{in}\right)$ % Compute ray signal
   2.3. $\mathbf{L}(i,:) := raysum2D\left(x_{in}, y_{in}, \theta_{in}, x_{out}, y_{out}, \theta_{out}\right)$ % Compute the estimated ray path lengths through each pixel.
3. Next i

[7] Of course in a practical application the computational efficiency of the solution algorithm may be of utmost significance, but will not be investigated herein.

4. $\hat{\boldsymbol{\lambda}}_0 := \lambda_{air}$ % Initialize scattering density vector to the value for air (the PoCA solution may also be used as a starting point)
5. $C_0 := fcst\left(\hat{\boldsymbol{\lambda}}_0, \mathbf{L}\right)$ % Compute initial cost, where $fcst(\cdot)$ is the Eq. (6.14) cost function
6. $C_l := 1x10^{-9}$ % Set cost function reduction limit (other values might be used).
7. Do
   7.1. $[C_1, \hat{\boldsymbol{\lambda}}_1] := fmincon\left(fcst\left(\hat{\boldsymbol{\lambda}}_0, \mathbf{L}\right), \lambda_{air}\right)$ % Compute new scattering density estimate, from start point $\hat{\boldsymbol{\lambda}}_0$ with lower bound λ_{air} on all elements.
   7.2. $C_d := C_1 - C_0$ % Compute reduction in cost function
   7.3. $\hat{\boldsymbol{\lambda}}_0 := \hat{\boldsymbol{\lambda}}_1$ % Update scattering strength estimate
   7.4. $C_0 := C_1$ % Update cost function
8. While $\left(C_d > C_l\right)$ % Loop while cost function reduction is greater than limit
9. $\hat{\boldsymbol{\lambda}}_{opt} := \hat{\boldsymbol{\lambda}}_0$ % Save last estimate as optimal estimate

6.1.3 Numerical Tests of the 2D MLS Reconstruction Algorithm

The same simulation that was described in Section 4.2.2 for testing of the PoCA algorithm was used to test the 2D MLS algorithm. Test case #1 consisting of horizontally placed (10 cm)^2 blocks of uranium, iron, and concrete was used for the first test case. Starting with an object area filled with air, the MLS algorithm required 49 iterations to find a solution. Results are shown in Figure 6.1, with PoCA algorithm results included for comparison. All three objects were correctly classified by the MLS algorithm with no reconstruction artifacts. The reconstructed scattering strength values were 88, 14, and 2 milliradians/cm^2 for the uranium, iron, and concrete blocks whose true values were 78, 14 and 2, respectively.

Results for test case #2, with the three blocks oriented vertically, are shown in Figure 6.2. 56 iterations were required to achieve the MLS solution, with all objects correctly classified with no reconstruction artifacts. The reconstructed scattering

density values were 89, 14, and 3 for the uranium, iron, and concrete blocks, respectively.

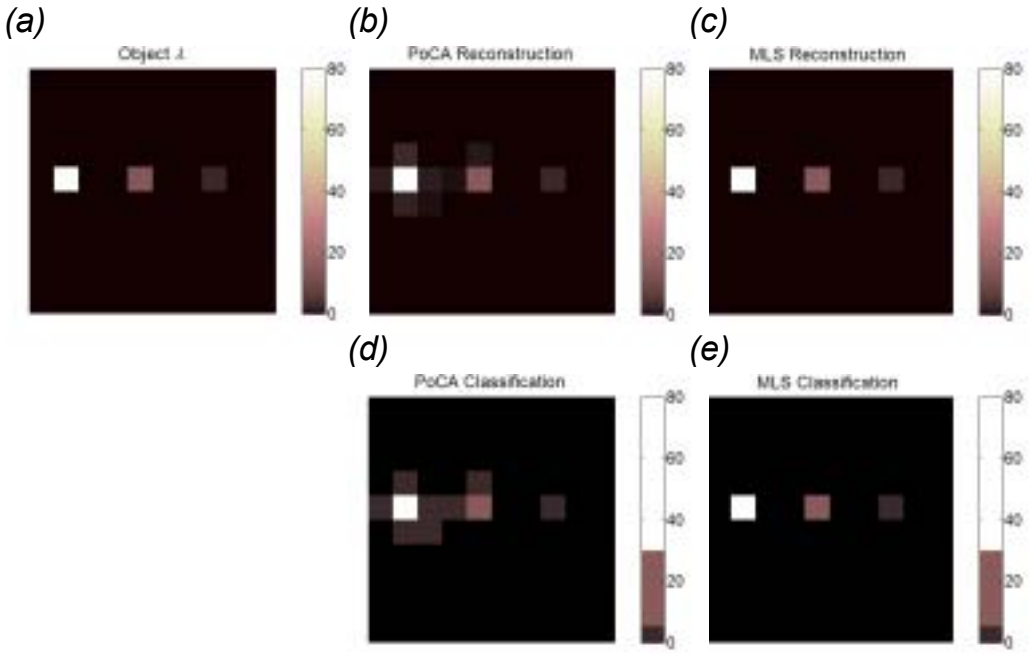

Figure 6.1 Results for test case #1. The simulated object scattering densities (a), the PoCA reconstruction (b), the MLS reconstruction (c), the PoCA classification (d), and the MLS classification (e).

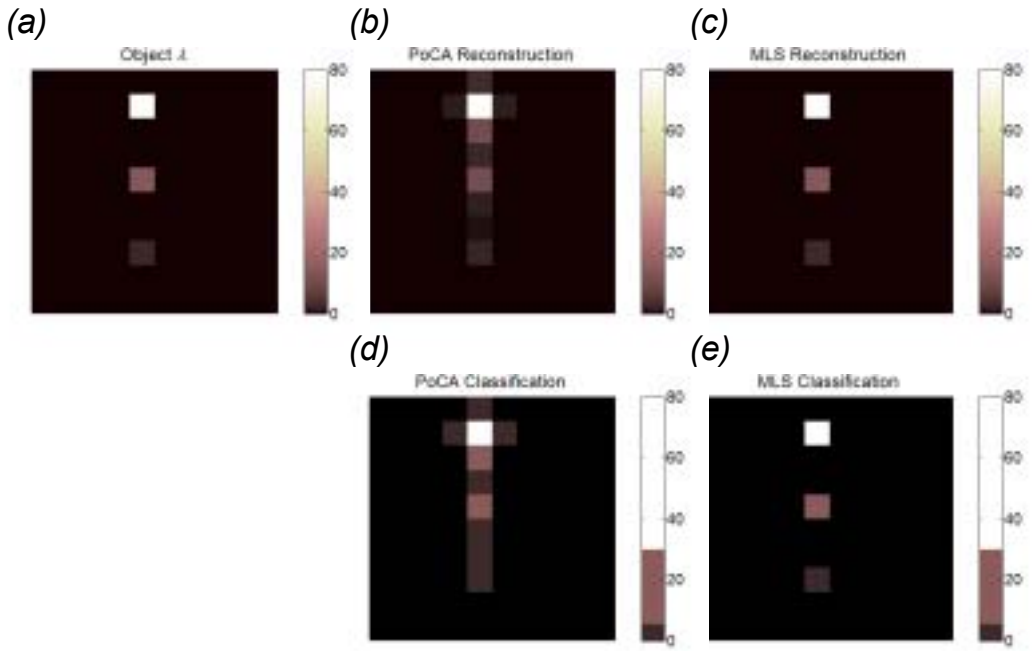

Figure 6.2 Results for test case #2. The simulated object scattering densities (a), the PoCA reconstruction (b), the MLS reconstruction (c), the PoCA classification (d), and the MLS classification (e).

Clearly application of tomographic methods is beneficial in the reconstruction process. This is particularly noticeable in test case #2. Rays that pass between the cubes and scatter little provide information indicating that no material exists there. The PoCA algorithm is unable to make use of this information except to the extent that low signal rays bring down the mean scattering density of cells through which they pass. The MLS algorithm seeks congruence between the scattering density estimate and the scattering of ALL rays, even those with very low scattering.

To examine the performance of the algorithm in a more tomographically ambiguous situation, a new test case #6 was defined (test cases 3-5 were defined in Chapter 4). For this case a central block of uranium is surrounded by a box of iron. This case is tomographically ambiguous since no rays pass horizontally through the

object – the most oblique rays are at 45 degrees from vertical. The object setup and reconstruction results are shown in Figure 6.3, where the MLS reconstruction was achieved in 57 iterations. The PoCA reconstruction is predictably blurred. The MLS reconstruction is better, but the effect of the ambiguity is apparent. The horizontal walls of the iron box are not well resolved, though the central uranium block is correctly classified.

An enhancement to the MLS framework and algorithm may be made to improve performance for such tomographically ambiguous cases, as will be discussed in the next section.

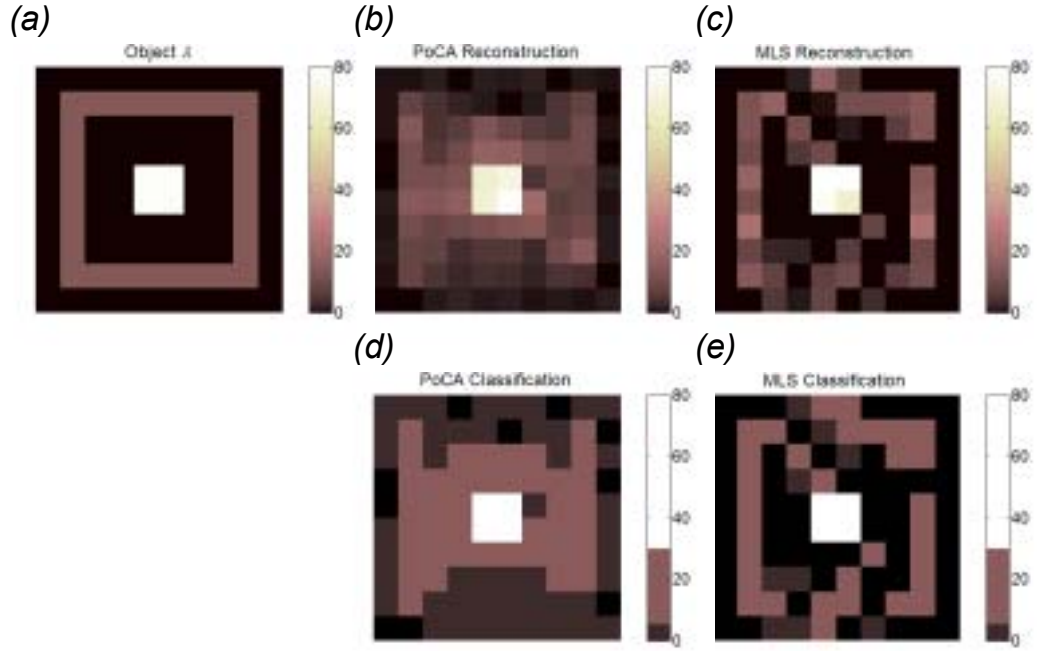

Figure 6.3 Results for test case #6. The simulated object scattering densities (a), the PoCA reconstruction (b), the MLS reconstruction (c), the PoCA classification (d), and the MLS classification (e).

6.2 Maximum Likelihood Tomographic Reconstruction using Scattering Angle and Ray Displacement Information

An intriguing feature of the PoCA algorithm is its ability to identify the approximate position of an object along the path of a ray. In traditional tomography no such localization is possible. In Chapter 4 the problems that such localization can cause were examined, and the MLS algorithm of the previous section was shown to provide improved performance for some cases. However, the calculation of the point of closest approach relies on the displacement of rays as well as their scattering. The ray displacement information can be incorporated into the maximum likelihood framework. The resultant algorithm, to be discussed in this section, will be called the MLSD (Maximum Likelihood Scattering and Displacement) algorithm.

6.2.1 The 2D MLSD Reconstruction Framework

Referring back to Figure 2.4, a charged particle passing through a material will experience both scattering and displacement. As has been previously discussed, the scattering angle may be approximated as a normally distributed random variable with zero mean and variance:

$$\sigma_{\Delta\theta}^2 = L\lambda \tag{6.15}$$

The ray displacement may also be approximated as a normally distributed random variable with zero mean and variance [1]:

$$\sigma_{\Delta x}^2 = \frac{L^2}{3}\sigma_{\Delta\theta}^2 = \frac{L^3}{3}\lambda \tag{6.16}$$

and the covariance between the ray scattering angle and displacement is:

$$\sigma_{\Delta\theta x} = \frac{L}{2}\sigma_{\Delta\theta}^2 = \frac{L^2}{2}\lambda \tag{6.17}$$

Ray scattering and displacement may thus be (approximately) described as distributed jointly Gaussian. In order to develop a tomographic algorithm that incorporates this information, expressions must be developed to describe the parameters of the distribution of rays passing through cells containing different materials.

Figure 6.4 illustrates the passage of a ray through 3 layers of material and provides expressions for the aggregate scattering and displacement as a function of scattering and displacement in each layer.

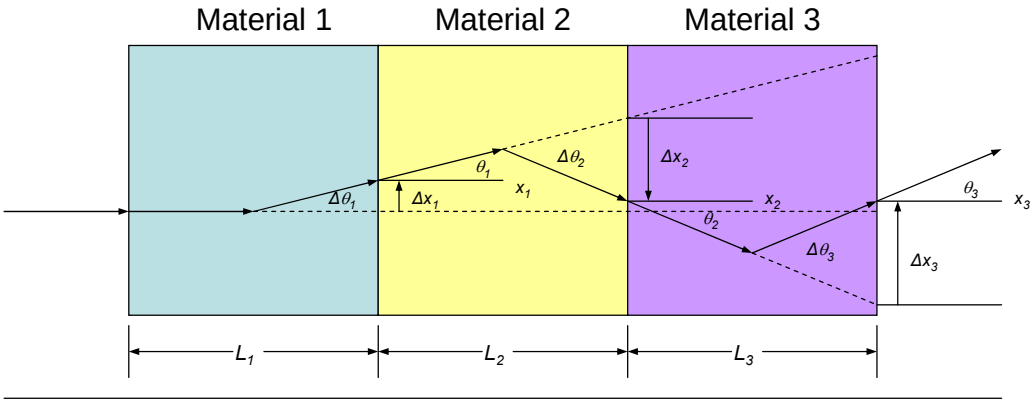

$$\text{assume } \Delta x_i << L_i$$

$$x_3 = x_2 + L_3 \cdot \tan(\theta_2) + \Delta x_3 \qquad \theta_3 = \theta_2 + \Delta\theta_3$$

$$x_2 = x_1 + L_2 \cdot \tan(\theta_1) + \Delta x_2 \qquad \theta_2 = \theta_1 + \Delta\theta_2$$

$$x_1 = \Delta x_1 \qquad \theta_1 = \Delta\theta_1$$

$$\theta_3 = \Delta\theta_1 + \Delta\theta_2 + \Delta\theta_3$$

$$x_3 = \Delta x_1 + L_2 \cdot \tan(\theta_1) + \Delta x_2 + L_3 \cdot \tan(\theta_2) + \Delta x_3$$

$$x_3 = \Delta x_1 + L_2 \cdot \tan(\Delta\theta_1) + \Delta x_2 + L_3 \cdot \tan(\Delta\theta_1 + \Delta\theta_2) + \Delta x_3$$

$$\text{assume small angles}$$

$$x_3 = \Delta x_1 + \Delta x_2 + \Delta x_3 + \Delta\theta_1(L_2 + L_3) + \Delta\theta_2(L_3)$$

Figure 6.4 Calculation of ray scattering and displacement for multiple layers of material

The expressions in Figure 6.4 may be generalized to N layers of material:

$$\Delta\theta = \sum_{j=1}^{N} \Delta\theta_j \tag{6.18}$$

$$\Delta x = \sum_{j=1}^{N} \left[\Delta x_j + T_j \cdot \Delta\theta_j \right] \tag{6.19}$$

where

$$T_j = \sum_{k=j+1}^{N} L_k \quad , j < N \qquad \text{and } T_N = 0 \tag{6.20}$$

Using Eq. (6.16-18) an expression for the variance in ray displacement may be developed:

$$V(\Delta x) = E(\Delta x \cdot \Delta x) - E(\Delta x) \cdot E(\Delta x) \tag{6.21}$$

But $E(\Delta x) = 0$, so

$$V(\Delta x) = E\left\{ \sum_{j=1}^{N} \left[\Delta x_j + T_j \cdot \Delta\theta_j \right] \cdot \sum_{k=1}^{N} \left[\Delta x_k + T_k \cdot \Delta\theta_k \right] \right\} \tag{6.22}$$

$$V(\Delta x) = \sum_{j=1}^{N} \sum_{k=1}^{N} \left[\begin{array}{l} E(\Delta x_j \cdot \Delta x_k) + T_j \cdot E(\Delta\theta_j \cdot \Delta x_k) \\ + T_k \cdot E(\Delta\theta_k \cdot \Delta x_j) + T_j \cdot T_k \cdot E(\Delta\theta_j \cdot \Delta\theta_k) \end{array} \right] \tag{6.23}$$

Since displacement and scattering in each layer are independent of displacement and scattering in other layers, and $E(\Delta\theta_j) = E(\Delta x_j) = 0$, all terms vanish for $j \neq k$.

$$V(\Delta x) = \sum_{j=1}^{N} \left[E(\Delta x_j \cdot \Delta x_j) + 2T_j \cdot E(\Delta\theta_j \cdot \Delta x_j) + T_j^2 \cdot E(\Delta\theta_j \cdot \Delta\theta_j) \right] \tag{6.24}$$

Substituting the terms of Eq. (6.13-15) into Eq. (6.22),

$$V(\Delta x) = \sum_{j=1}^{N} \left[\frac{L_j^3}{3} \lambda_j + 2T_j \cdot \frac{L_j^2}{2} \lambda_j + T_j^2 \cdot L_j \lambda_j \right] \tag{6.25}$$

$$\sigma_{\Delta x}^2 = \sum_{j=1}^{N}\left[\left(\frac{L_j^3}{3} + T_j L_j^2 + T_j^2 L_j\right)\lambda_j\right] \tag{6.26}$$

Eq. (6.26) is the desired result, an expression for the ray displacement variance in terms of layer path lengths and cell scattering densities. Proceeding in a similar fashion to develop an expression for the covariance term:

$$E(\Delta\theta \cdot \Delta x) = E\left\{\sum_{j=1}^{N}\Delta\theta_j \cdot \sum_{k=1}^{N}\left[\Delta x_k + T_k \cdot \Delta\theta_k\right]\right\} \tag{6.27}$$

$$E(\Delta\theta \cdot \Delta x) = E\left\{\sum_{j=1}^{N}\sum_{k=1}^{N}\left[\Delta\theta_j \cdot \Delta x_k + T_k \cdot \Delta\theta_j \cdot \Delta\theta_k\right]\right\} \tag{6.28}$$

$$E(\Delta\theta \cdot \Delta x) = \sum_{j=1}^{N}\sum_{k=1}^{N}\left[E\left(\Delta\theta_j \cdot \Delta x_k\right) + T_k \cdot E\left(\Delta\theta_j \cdot \Delta\theta_k\right)\right] \tag{6.29}$$

Again all terms vanish for $j \neq k$.

$$E(\Delta\theta \cdot \Delta x) = \sum_{j=1}^{N}\left[E\left(\Delta\theta_j \cdot \Delta x_j\right) + T_j \cdot E\left(\Delta\theta_j \cdot \Delta\theta_j\right)\right] \tag{6.30}$$

$$E(\Delta\theta \cdot \Delta x) = \sum_{j=1}^{N}\left[\frac{L_i^2}{2}\lambda_j + T_j L_j \lambda_j\right] \tag{6.31}$$

$$\sigma_{\Delta\theta x} = \sum_{j=1}^{N}\left[\left(\frac{L_j^2}{2} + L_j T_j\right)\lambda_j\right] \tag{6.32}$$

Eq. (6.32) expresses the covariance in terms of layer path lengths and cell scattering densities. Finally, per the MLS development,

$$\sigma_{\Delta\theta}^2 = \sum_{j=1}^{N} L_j \lambda_j \tag{6.33}$$

Eqs. (6.26,32,33) express the parameters of the jointly Gaussian scattering / displacement distribution in terms of layer path lengths. The form of these equations is unchanged if the layers become cells or pixels. However, the T terms will not be calculated according to Eq. (6.20). Instead, each T_j term is calculated to be the sum of cell path lengths *downstream* from cell j along ray path. For a cell grid containing N^2 cells, the following weighting vectors may then be assigned for a given ray i:

$$\mathbf{W}_{\boldsymbol{\theta} i} = \begin{bmatrix} L_{i1} & L_{i2} & \dots & L_{iN^2} \end{bmatrix} \tag{6.34}$$

$$\mathbf{W}_{\boldsymbol{\theta}\mathbf{x} i} = \begin{bmatrix} L_{i1}^2/2 + L_{i1}T_{i1} & L_{i2}^2/2 + L_{i2}T_{i2} & \dots & L_{iN^2}^2/2 + L_{iN^2}T_{iN^2} \end{bmatrix} \tag{6.35}$$

$$\mathbf{W}_{\mathbf{x} i} = \begin{bmatrix} L_{i1}^3/3 + T_{i1}L_{i1}^2 + T_{i1}^2 L_{i1} \\ L_{i2}^3/3 + T_{i2}L_{i2}^2 + T_{i2}^2 L_{i2} \\ \dots \\ L_{iN^2}^3/3 + T_{iN^2}L_{iN^2}^2 + T_{iN^2}^2 L_{iN^2} \end{bmatrix}^T \tag{6.36}$$

where L_{ij} represents the ray path length of ray i in cell j and T_{ij} the sum of ray i path lengths over cells downstream of cell j along the ray path. The parameters of the jointly Gaussian scattering / displacement distributions for ray i in terms of the weighting vectors and scattering density estimates are then

$$\hat{v}_{\theta i} = \mathbf{W}_{\boldsymbol{\theta} i}\hat{\boldsymbol{\lambda}} \tag{6.37}$$

$$\hat{s}_{\theta x i} = \mathbf{W}_{\boldsymbol{\theta}\mathbf{x} i}\hat{\boldsymbol{\lambda}} \tag{6.38}$$

$$\hat{v}_{x i} = \mathbf{W}_{\mathbf{x} i}\hat{\boldsymbol{\lambda}} \tag{6.39}$$

The covariance matrix of the estimated distribution is:

$$\hat{\boldsymbol{\Sigma}}_i = \begin{bmatrix} \hat{v}_{\theta i} & \hat{s}_{\theta x i} \\ \hat{s}_{\theta x i} & \hat{v}_{x i} \end{bmatrix} \tag{6.40}$$

The incoming and outgoing angle θ_{in} and θ_{out} and position x_{in} and x_{out} of each ray are measured. The scattering signal is simply the difference in angles:

$$\Delta\theta_i = \theta_{out,i} - \theta_{in,i} \tag{6.41}$$

Some calculation is necessary to compute ray displacement. First the non-scattered position $x_{proj,i}$ is calculated by projecting the incoming ray track to the bottom of the cell grid (detector position). This measured position difference must be projected onto a line perpendicular to the mean ray path:

$$\Delta x_i = \left(x_{out,i} - x_{proj,i}\right) \Big/ \cos\left(\frac{\theta_{out} + \theta_{in}}{2}\right) \tag{6.42}$$

The data vector for ray i is defined to be:

$$\mathbf{d}_i = \begin{bmatrix} \Delta\theta_i \\ \Delta x_i \end{bmatrix} \tag{6.43}$$

To perform tomographic reconstruction, congruency between these measured values and the distribution with the covariance matrix of Eq. (6.40) is sought. The method of maximum likelihood employed in the MLS algorithm may be used in this case as well. The probability of the data vector $\mathbf{d}_i$ given $\boldsymbol{\Sigma}_i$ is:

$$P\left(\mathbf{d}_i \middle| \hat{\boldsymbol{\Sigma}}_i\right) = \frac{1}{2\pi\left|\hat{\boldsymbol{\Sigma}}_i\right|^{1/2}} \exp\left(-\frac{1}{2}\mathbf{d}_i^{\mathrm{T}}\hat{\boldsymbol{\Sigma}}_i^{-1}\mathbf{d}_i\right) \tag{6.44}$$

Proceeding in a fashion similar to that used for the MLS algorithm, an estimate $\hat{\boldsymbol{\lambda}}^*$ that maximizes probability may be written.

$$\hat{\boldsymbol{\lambda}}^* = \arg\min_{\hat{\boldsymbol{\lambda}}}\left\{\sum_{i=1}^{M}\left[\ln\left(\left|\hat{\boldsymbol{\Sigma}}_i\right|\right) + \mathbf{d}_i^{\mathrm{T}}\hat{\boldsymbol{\Sigma}}_i^{-1}\mathbf{d}_i\right]\right\} \quad \text{such that } \hat{\lambda}_j \geq \lambda_{air} \text{ for all } j \tag{6.45}$$

6.2.2 The 2D MLSD Reconstruction Algorithm

The cost function for the minimization problem may be written as:

$$F\left(\hat{\boldsymbol{\lambda}}\right)=\frac{1}{M}\sum_{i=1}^{M}\left[\ln\left(\left|\hat{\boldsymbol{\Sigma}}_i\right|\right)+\mathbf{d}_i^{\mathrm{T}}\hat{\boldsymbol{\Sigma}}_i^{-1}\mathbf{d}_i\right] \tag{6.46}$$

The MLSD algorithm is very similar to the MLS algorithm, with a few extra steps required to setup the data and weight matrices, as outlined below. Derivation of the Jacobian and Hessian matrices is somewhat more complex, as outlined in Appendix C, and more computationally expensive.

2D MLSD Algorithm

1. Establish an NxN grid of LxL sized pixels over the object area. Establish a Cartesian coordinate system with x horizontal, y vertical. Measured data is $\left(x_{in}, y_{in}, \theta_{in}, x_{out}, y_{out}, \theta_{out}\right)$ for each of M rays.
2. For $i := 1 \text{ to } M$ % loop over rays
   - 2.1. $\left(x_{in}, y_{in}, \theta_{in}, x_{out}, y_{out}, \theta_{out}\right) := \left(x_{in}, y_{in}, \theta_{in}, x_{out}, y_{out}, \theta_{out}\right)_i$ % Get ray data
   - 2.2. $\theta := \left(\theta_{out} - \theta_{in}\right)$ % Compute scattering signal
   - 2.3. $\bar{\theta} := \left(\theta_{in} + \theta_{out}\right)/2$ % Compute average ray angle
   - 2.4. $x_{proj} := x_{in} + \tan\left(\theta_{in}\right)\cdot\left(y_{out} - y_{in}\right)$ % Compute projected un-deflected position
   - 2.5. $x := \left(x_{out} - x_{proj}\right)\cdot\cos\left(\bar{\theta}\right)$ % Compute displacement signal
   - 2.6. $d\left(i,:\right) = \left[\theta \quad x\right]$ % Establish data vector for ray
   - 2.7. $\left[\mathbf{L}, \mathbf{T}\right] := raysum2D\left(x_{in}, y_{in}, \theta_{in}, x_{out}, y_{out}, \theta_{out}\right)$ % Compute the estimated ray path lengths through each pixel.
   - 2.8. $\mathbf{W_\theta}\left(i,:\right) := \mathbf{L}$ % Compute row of angle weights
   - 2.9. $\mathbf{W_{\theta x}}\left(i,:\right) := \left[L_1^2/2 + L_1T_1 \quad L_2^2/2 + L_2T_2 \quad \ldots \quad L_{N^2}^2/2 + L_{N^2}T_{N^2}\right]$ % Compute row of angle/displacement weights
   - 2.10. $\mathbf{W_x}\left(i,:\right) := \left[L_1^3/3 + T_1L_1^2 + T_1^2L_1 \quad L_2^3/3 + T_2L_2^2 + T_2^2L_2 \quad \ldots \quad L_{N^2}^3/3 + T_{N^2}L_{N^2}^2 + T_{N^2}^2L_{N^2}\right]$ % Compute row of displacement weights
3. Next i

4. $\hat{\boldsymbol{\lambda}}_0 := \lambda_{air}$ % Initialize scattering density vector to the value for air (the PoCA solution may also be used as a starting point)
5. $C_0 := fcsttx\left(\hat{\boldsymbol{\lambda}}_0, \mathbf{W_\theta}, \mathbf{W_x}, \mathbf{W_{\theta x}}, \mathbf{d}\right)$ % Compute initial cost, where $fcsttx(\cdot)$ is the Eq. (6.46) cost function
6. $C_l := 1x10^{-9}$ % Set cost function reduction limit (other values might be used).
7. Do
   7.1. $[C_1, \hat{\boldsymbol{\lambda}}_1] := fmincon\left[fcsttx\left(\hat{\boldsymbol{\lambda}}_0, \mathbf{W_\theta}, \mathbf{W_x}, \mathbf{W_{\theta x}}, \mathbf{d}\right), \lambda_{air}\right]$ % Compute new scattering density estimate, from start point $\hat{\boldsymbol{\lambda}}_0$ with lower bound λ_{air} on all elements.
   7.2. $C_d := C_1 - C_0$ % Compute reduction in cost function
   7.3. $\hat{\boldsymbol{\lambda}}_0 := \hat{\boldsymbol{\lambda}}_1$ % Update scattering strength estimate
   7.4. $C_0 := C_1$ % Update cost function
8. While $(C_d > C_l)$ % Loop while cost function reduction is greater than limit
9. $\hat{\boldsymbol{\lambda}}_{opt} := \hat{\boldsymbol{\lambda}}_0$ % Save last estimate as optimal estimate

6.2.3 Numerical Tests of the 2D MLSD Reconstruction Algorithm

Given the good performance of the MLS algorithm on test cases #1 and #2, these cases should pose little difficulty for the MLSD algorithm. Reconstructions of the first two test cases are shown in Figure 6.5, where no reconstruction artifacts may be seen for either case. The reconstructed scattering densities for the uranium, iron, and concrete blocks were 76, 13, and 2 milliradians^2/cm, respectively, for case #1, and 79, 13, and 2 for case #2. True values were 78, 14, and 2. Computation time for these test cases using the MLSD algorithm was about 2.3 times that of the MLS algorithm.

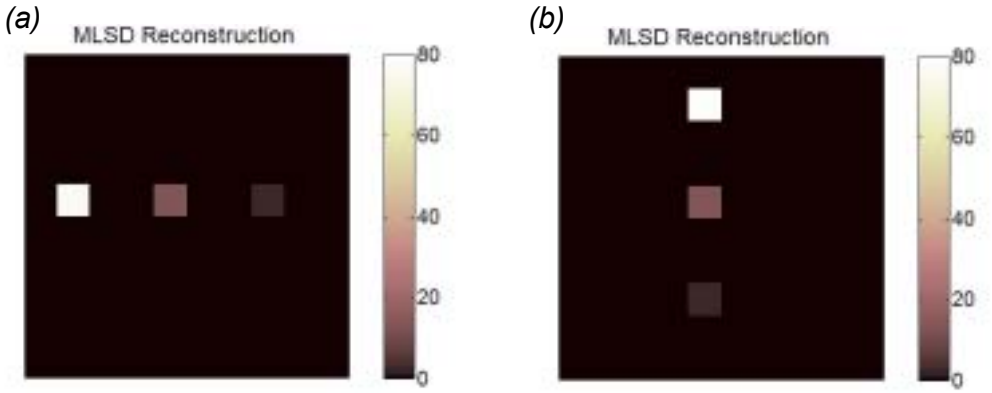

Figure 6.5 MLSD reconstructions of test case #1 (a), and test case #2 (b). Images of the actual objects are identical (see Figures 6.1 and 6.2).

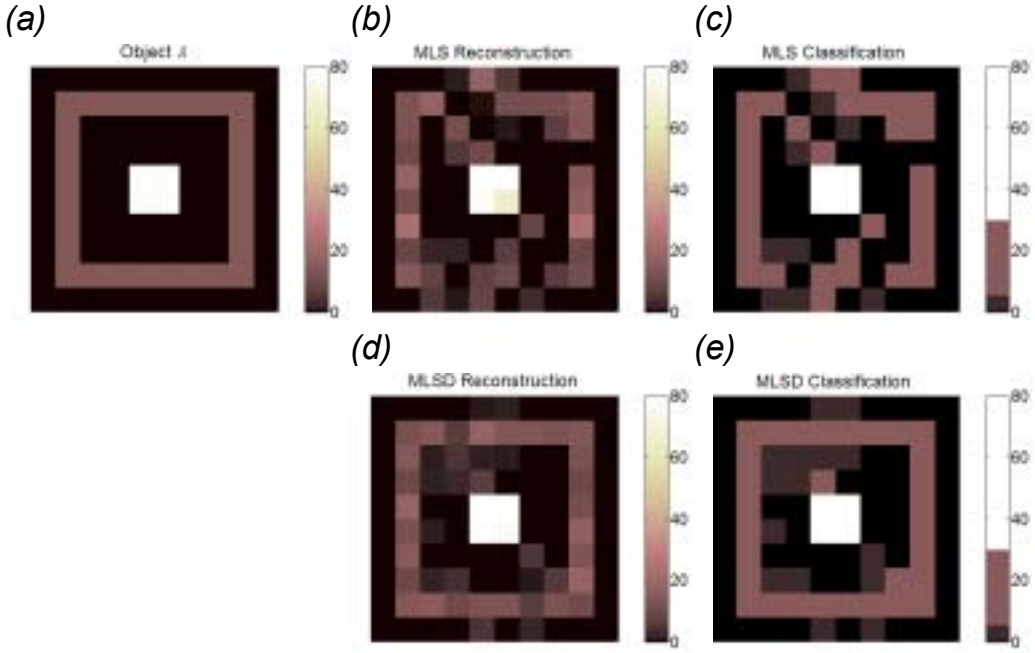

Figure 6.6 Results for test case #6. The objects (a), the MLS reconstruction (b) and classification (c), the MLSD reconstruction (d) and classification (e).

Results for test case #6 are shown in Figure 6.6, with MLSD and MLS results shown to allow comparison. The enhanced ability of the MLSD algorithm to deal with the tomographic ambiguity is apparent. Because artifacts do exist even in the

MLSD reconstruction, it is wise to introduce quantified performance indices, and this will be done shortly.

First, however, it is instructive to more clearly illustrate the value of incorporating displacement information. The simulation of test case #1 was repeated, but with all rays oriented absolutely vertical. Intuitively, and from the Fourier Slice Theorem discussion of Section 2.5.1, traditional tomography would be unable to identify any vertical structure in such a case. In other words, the blocks in test case #1 would be indistinguishable from vertical columns of equivalent distributed density. MLS and MLSD reconstructions of test case #1 using only vertical rays appear in Figure 6.7. The MLS reconstruction illustrates the ambiguity of the problem, but the MLSD reconstruction is indistinguishable from the actual scene. This is a remarkable result, and illustrates the fundamental difference between traditional tomography and scattering tomography making use of ray displacement[8].

[8] Actually, the MLS reconstruction is interesting. The slight localization of the signal (i.e., the reconstruction is not just vertical columns extending from top to bottom) may be due to a modest tomographic benefit due to *scattered* ray paths not remaining perfectly vertical.

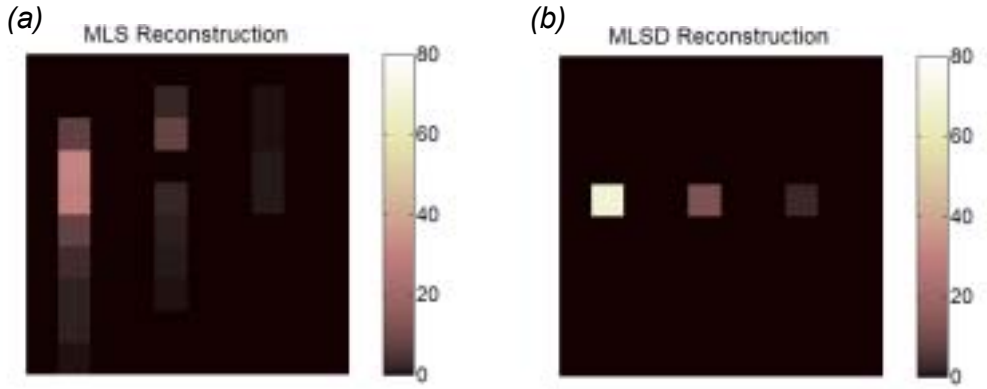

Figure 6.7 MLS (a) and MLSD (b) reconstructions of test case #1 with all interrogating rays oriented vertically, passing from top to bottom.

Test case #3, introduced in Chapter 4, consisted of a large block of iron, and illustrated the tendency of the PoCA algorithm to lump material into the middle of large block spanning multiple reconstruction cells. Results for the PoCA and MLSD reconstruction algorithms on test case #3 are illustrated in Figure 6.8. The outer boundary of the object is better reproduced by the MLSD algorithm than with the PoCA algorithm, but the reconstruction and classification of the interior of the object is arguably no better. However, the mechanisms producing the artifacts are different. In the MLSD algorithm, the artifacts can be empirically shown to be the caused by under sampling, while the "lumping" effect is inherent in the PoCA algorithm.

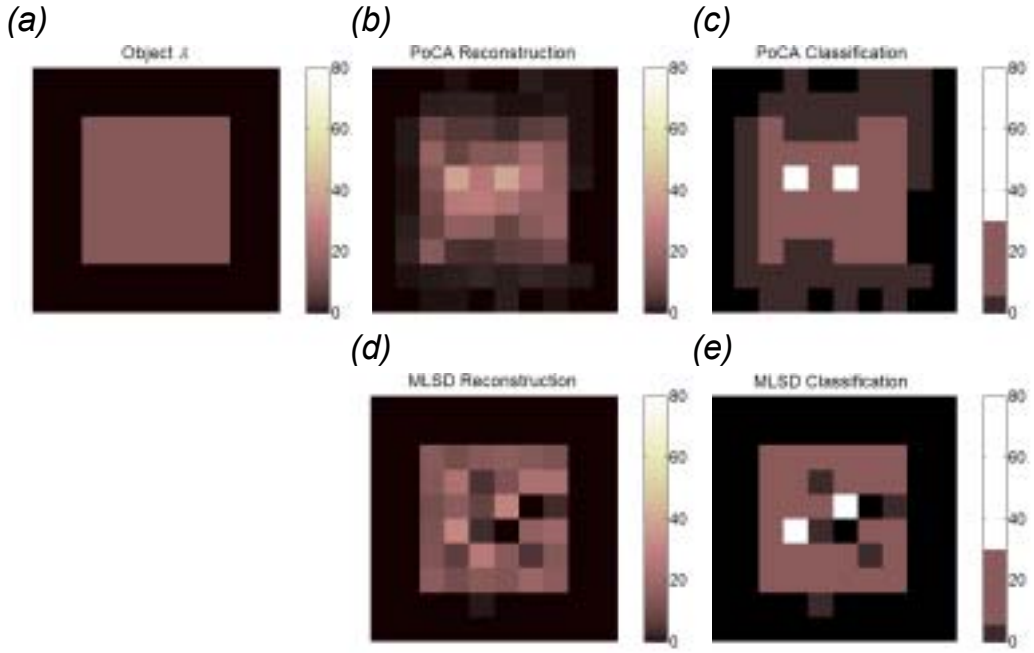

Figure 6.8 Results for test case #3, one minute simulated exposure. The objects (a), the PoCA reconstruction (b) and classification (c), the MLSD reconstruction (d) and classification (e).

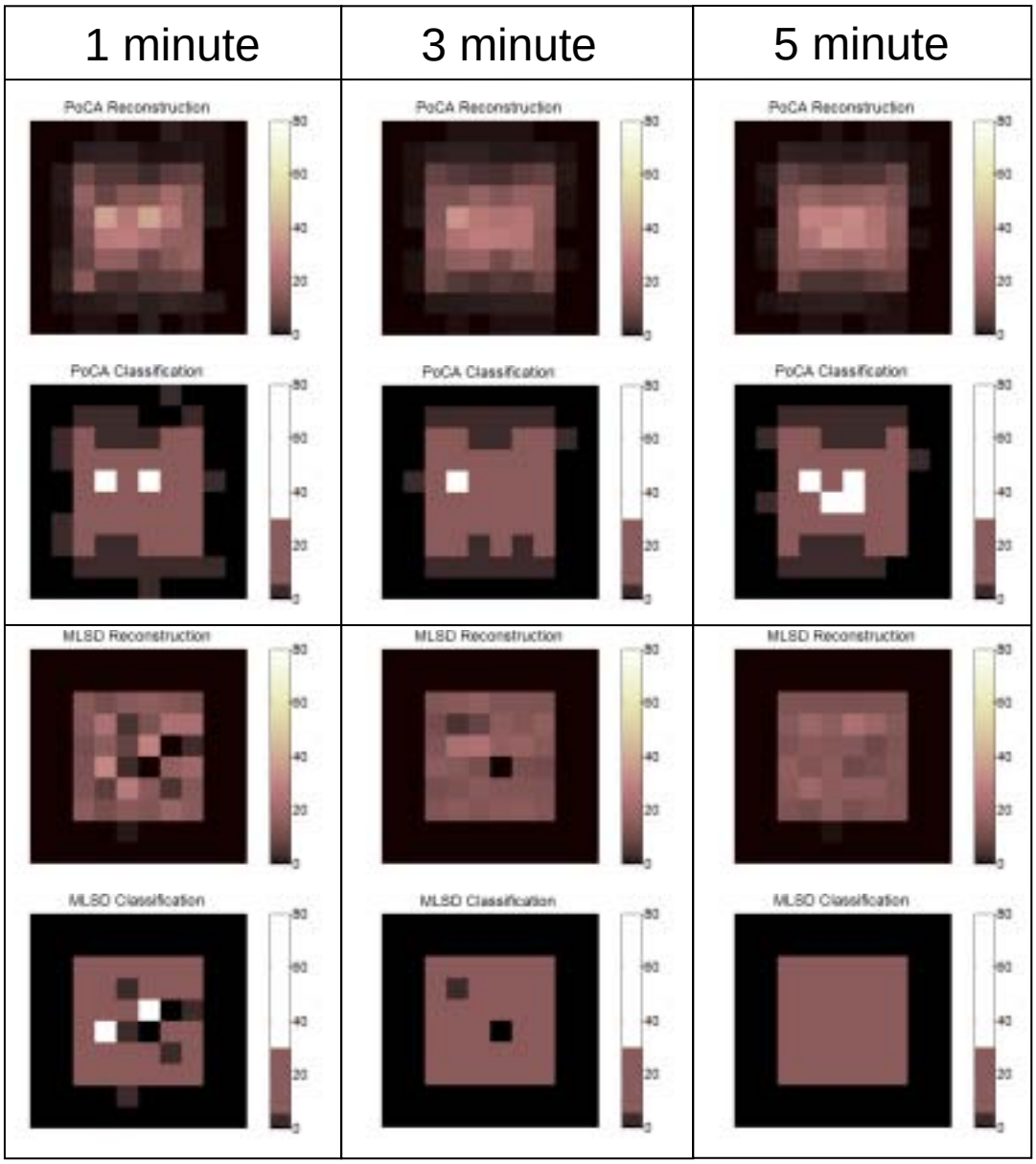

Figure 6.9 PoCA and MLSD results for test case #3 for 1, 3, and 5 minute simulated exposures.

Figure 6.9 shows that MLSD performance for test case #3 improves with exposure time, i.e., with more rays sampling the object, but not so for the PoCA algorithm. This suggests that the artifacts in the one minute MLSD reconstruction are related to under sampling of the object. The values of the cost function of Eq. (6.46) applied to the 1 minute exposure data using the scattering density vector of the actual

object, the MLSD reconstruction, and the PoCA reconstruction are -12.977, -11.800, and -12.993, respectively. Thus the measured ray data is almost equally probable given either the scattering density vector of the actual object or the MLSD reconstruction, though these vectors are quite different from each other. This observation suggests that regularization of the MLSD solution might prove useful. Though regularization is outside the scope of this dissertation, investigation is suggested as future work.

As a final example of the performance of the MLSD algorithm, results for test case #7, a scene with somewhat complex object structure, are presented.

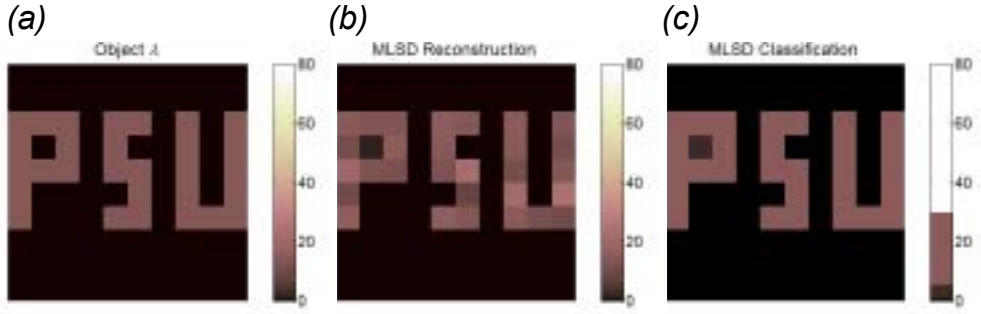

Figure 6.10 Test case #7 objects, the letters "PSU" made of iron (a), the one minute MLSD reconstruction (b) and classification (c).

6.2.4 Performance Indices and Algorithm Performance

Returning to the task of defining performance indices for the reconstructions, the first index will simply be the RMS difference between a reconstructed scattering density vector and the actual scattering density:

$$P_{rms} = \sqrt{\frac{1}{N^2}\sum_{j=1}^{N^2}\left(\lambda_{recon,j} - \lambda_{actual,j}\right)^2} \tag{6.47}$$

To compare classification performance, the classification of a cell is formally defined as:

$$C_j = \begin{cases} 0, & \lambda_j \le .5 & (air) \\ 1, & .5 < \lambda_j \le 5 & (low - Z) \\ 2, & 5 < \lambda_j \le 30 & (medium - Z) \\ 3, & 30 < \lambda_j & (high - Z) \end{cases} \tag{6.48}$$

and classification error is defined as the sum of absolute cell classification error:

$$P_c = \frac{1}{N^2} \sum_{j=1}^{N^2} \left| C_{recon,j} - C_{actual,j} \right| \tag{6.49}$$

Values for these indices are shown in Table 6.1. In all cases, the MLSD is the best performing algorithm.

Table 6.1 Performance Measurements for 2D Test Case Reconstructions

		P_{rms}			P_c		
Test Case	Exposure Time	PoCA	MLS	MLSD	PoCA	MLS	MLSD
1	1	1.08	0.99	0.25	0.05	0.00	0.00
2	1	1.32	1.07	0.13	0.07	0.00	0.00
3	1	5.56	7.88	4.56	0.28	0.32	0.11
3	2	5.77	5.63	3.61	0.29	0.21	0.02
3	3	4.88	4.16	2.51	0.27	0.16	0.03
3	4	5.32	5.11	2.71	0.27	0.13	0.01
3	5	5.28	3.69	1.76	0.27	0.11	0.00
6	1	7.76	5.53	2.54	0.93	0.36	0.19
7	1	4.77	4.62	1.94	0.48	0.19	0.01

6.2.5 Extensions to the 2D MLSD Algorithm

6.2.5.1 Measurement Error

The finite resolution of the muon detectors can affect reconstruction quality. Muon tracks and thus bend angles are computed from position information, as are ray displacements, of course. In the simulated examples presented so far in this chapter,

no position resolution effects were included. The wire chambers used for the experiment described in Chapter 5 exhibited a resolution measured at 0.016 cm RMS. With 27 cm detector spacing, this position resolution produces about a 0.8 milliradian RMS error in measuring track angles, and a 1.1 milliradian error in computed bend angles. It will be seen that such errors do produce artifacts in the baseline MLSD algorithm, but that these artifacts are substantially reduced if the position resolution is incorporated into the MLSD statistical model.

Position error was incorporated into the MLSD statistical model as follows. The RMS position error for any given measuring plane is denoted E_p, the spacing between the upper detector pair (or lower detector pair) is denoted dz_o, and the spacing between inner detectors dz_i. Detectors are labeled [*upper, in, out, lower*] from top to bottom. Incoming track angle is computed as:

$$\theta_{in} = \tan^{-1}\left(\frac{x_{in} - x_{upper}}{dz_o}\right) \tag{6.50}$$

Measured incoming angle, denoted with a tilde, is expressed as

$$\widetilde{\theta}_{in} = \tan^{-1}\left[\frac{\left(x_{in} + e_{p,in}\right) - \left(x_{upper} + e_{p,upper}\right)}{dz_o}\right] \tag{6.51}$$

where the e_p terms are samples from the Gaussian position error distribution. These terms are small, so using a small angle approximation:

$$\widetilde{\theta}_{in} \cong \theta_{in} + \frac{e_{p,in} - e_{p,upper}}{dz_o} \tag{6.52}$$

and since the two position errors are i.i.d., the mean square error in angle measurement is:

$$E_\theta^2 = V\left(\widetilde{\theta}_{in}\right) \cong \frac{2E_p^2}{dz_o^2} \tag{6.53}$$

Eq. (6.53) clearly applies to both incoming and outgoing angle measurement. The measured bend angle of a ray is the difference between these two independent angle measurements, so:

$$E_{\Delta\theta}^2 \cong \frac{4E_p^2}{dz_o^2} \tag{6.54}$$

The measured displacement of a ray is computed as:

$$\Delta\widetilde{x} = \widetilde{x}_{out} - \widetilde{x}_{proj,in} = \widetilde{x}_{out} - \left(\widetilde{x}_{in} + dz_i \tan\widetilde{\theta}_{in}\right) \tag{6.55}$$

where, for simplicity, the correction in Step 2.5 of the MLSD algorithm is omitted in this analysis. Expanding Eq. (6.55) to express measured quantities in terms actual quantities plus error:

$$\Delta\widetilde{x} = \left(x_{out} + e_{p,out}\right) - \left(x_{in} + e_{p,in} + dz_i \tan\left(\theta_{in} + \frac{e_{p,in} - e_{p,upper}}{dz_o}\right)\right) \tag{6.56}$$

Assuming small angles,

$$\Delta\widetilde{x} = x_{out} - \left(x_{in} + dz_i \tan\theta_{in}\right) + e_{p,out} - \left(e_{p,in} + \frac{dz_i}{dz_o}e_{p,in} - \frac{dz_i}{dz_o}e_{p,upper}\right) \tag{6.57}$$

$$\Delta\widetilde{x} = \Delta x + e_{p,out} - \left(1 + \frac{dz_i}{dz_o}\right)e_{p,in} + \frac{dz_i}{dz_o}e_{p,upper} \tag{6.58}$$

Taking the variance of the measured displacement,

$$V(\Delta\tilde{x}) = V(\Delta x) + E_p^2 + \left(1 + \frac{dz_i}{dz_o}\right)E_p^2 + \left(\frac{dz_i}{dz_o}\right)E_p^2 \tag{6.59}$$

From Eq. (6.59) the mean square displacement error may be established as:

$$E_{\Delta x}^2 = 2\left[1 + \frac{dz_i}{dz_o} + \left(\frac{dz_i}{dz_o}\right)^2\right]E_p^2 \tag{6.60}$$

To complete the derivation the covariance term must be computed:

$$E(\Delta\tilde{\theta}\Delta\tilde{x}) = E\begin{bmatrix}\left(\Delta\theta + \frac{e_{p,lower} - e_{p,out}}{dz_o} - \frac{e_{p,in} - e_{p,upper}}{dz_o}\right) \\ \left(\Delta x + e_{p,out} - \left(1 + \frac{dz_i}{dz_o}\right)e_{p,in} + \frac{dz_i}{dz_o}e_{p,upper}\right)\end{bmatrix} \tag{6.61}$$

$$E(\Delta\tilde{\theta}\Delta\tilde{x}) = E(\Delta\theta\Delta x) + E\left[\frac{dz_i}{dz_o^2}e_{p,upper}^2 + \left(\frac{1}{dz_o} + \frac{dz_i}{dz_o^2}\right)e_{p,in}^2 - \frac{1}{dz_o}e_{p,out}^2\right] \tag{6.62}$$

$$E(\Delta\tilde{\theta}\Delta\tilde{x}) = E(\Delta\theta\Delta x) + 2\frac{dz_i}{dz_o^2}E_p^2 \tag{6.63}$$

$$E_{\Delta\theta x} = 2\frac{dz_i}{dz_o^2}E_p^2 \tag{6.64}$$

Eqs. (6.54,60,64) represent the means to incorporate the effect of position resolution into the MLSD algorithm, accomplished by modifying Eqs. (6.37-39) to:

$$\hat{v}_{\theta i} = \mathbf{W}_{\boldsymbol{\theta i}}\hat{\boldsymbol{\lambda}} + E_{\Delta\theta}^2 \tag{6.65}$$

$$\hat{s}_{\theta xi} = \mathbf{W}_{\boldsymbol{\theta x i}}\hat{\boldsymbol{\lambda}} + E_{\Delta\theta x} \tag{6.66}$$

$$\hat{v}_{xi} = \mathbf{W}_{\mathbf{x}i}\hat{\boldsymbol{\lambda}} + E_{\Delta x}^2 \tag{6.67}$$

Figure 6.11 shows the effect of position measurement error. In the left frame is the MLSD reconstruction with no position error simulated. In the middle frame is a reconstruction with .016 cm RMS position error and 27 cm outer detector spacing simulated but unaccounted for in the reconstruction. Significant artifacts are apparent

in the corners of the image. The right frame shows the effect of accounting for the position error in the statistical model. No artifacts appear in the corrected reconstruction.

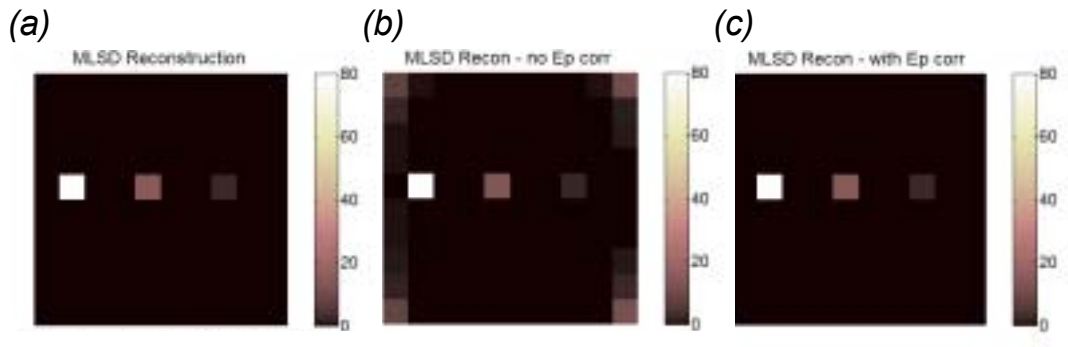

Figure 6.11 Effect of position measurement error. Test case #1 MLSD reconstruction with no position error simulated (a), with position error simulated but unaccounted for in MLSD (b), and with error accounted for in MLSD algorithm (c).

Eqs. (6.54) and (6.60) show that the ratio of detector spacings strongly effect measurement uncertainties. For the example of Figure 6.10, the inner detector spacing was 100 cm and the outer was 27 cm, with a 0.016 cm RMS position error, resulting in about 1 milliradian RMS error in measuring bend angle, and about 1 mm RMS displacement error. Decreasing outer detector spacing to 5 cm, for example, with the same detector resolution results in 6 milliradians RMS angle error and 5 mm RMS displacement error. Unfortunately, increasing the outer detector spacing reduces the acceptance angle and so the number of muons available to sample the volume unless detector size is also increased. For design of a real instrument such effects will need to be carefully considered relative to the requirements of the task.

However, the ability of the MLSD algorithm to handle detector resolution in a principled manner is a major advantage relative to PoCA. Figure 6.12 shows PoCA

and MLSD reconstructions of the test case #1 scene using 5 cm outer detector spacing and .016 cm RMS detector resolution. The MLSD algorithm performs much better than PoCA when measurement error is substantial.

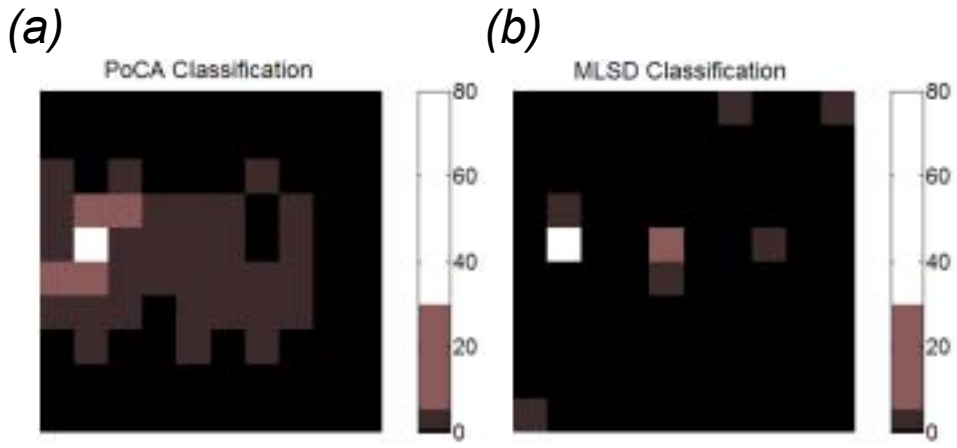

Figure 6.12 PoCA (a) and MLSD (b) classifications of test case #1 with more significant measurement error (dz_o = 5 cm).

6.2.5.2 Cosmic Ray Muon Momentum Spread

Prior examples in this chapter were produced by simulating the passage of nominal momentum muons through the object area. This was done to most clearly illustrate the relative performance of algorithms. As explained in Chapter 2, real cosmic ray muons arrive at the Earth's surface with varying momenta. When muon momentum varies, the scattering variance expression in Eq. (6.15) is not valid. For a muon with momentum p the scattering variance is instead:

$$\sigma_\theta^2 = L\left(\frac{15}{p}\right)^2 \frac{1}{L_{rad}} = L\left(\frac{p_0}{p}\right)^2 \left(\frac{15}{p_0}\right)^2 \frac{1}{L_{rad}} = L\left(\frac{p_0}{p}\right)^2 \lambda \tag{6.68}$$

If muon momentum is known, varying momenta can be handled by adjusting the statistical model. However, though the cosmic ray muon momentum distribution has

been studied and may be simulated through models such as the Blanpied generator described in Appendix A, the momentum of any individual muon is not known unless it is measured.

In Section 3.3.3 a method was introduced for estimating muon momentum by measuring muon scattering through fixed planes of material of known composition and thickness. If an estimate of the momentum of ray i is available, then that estimate might be used as a proxy for the real momentum in Eq. (6.68). However, since there is some uncertainty in the muon momentum estimate itself, this uncertainty must be accounted for. Details of the statistical implications of momentum measurement by scattering are presented in Appendix B. Based on that development, if a momentum estimate $\hat{p}_i$ is made, the equations describing the covariance matrix for ray i in the MLSD algorithm are modified to:

$$\hat{v}_{\theta i} = F_{pi}\mathbf{W}_{\boldsymbol{\theta} i}\hat{\boldsymbol{\lambda}} + E_{\Delta\theta}^2 \tag{6.69}$$

$$\hat{s}_{\theta xi} = F_{pi}\mathbf{W}_{\boldsymbol{\theta x} i}\hat{\boldsymbol{\lambda}} + E_{\Delta\theta x} \tag{6.70}$$

$$\hat{v}_{xi} = F_{pi}\mathbf{W}_{\mathbf{x}i}\hat{\boldsymbol{\lambda}} + E_{\Delta x}^2 \tag{6.71}$$

where the correction factor F_{pi} is computed as:

$$F_{pi} = M_{2p}\left(\frac{p_0}{\hat{p}_i}\right)^2 \tag{6.72}$$

M_{2p} is the second moment of the fractional error in the muon momentum estimate, and is required to produce unbiased $\hat{\lambda}$ reconstruction. As discussed in Appendix B, the second moment of the momentum error decreases as the number of momentum measuring planes is increased. The remainder of the MLSD algorithm is unchanged.

To illustrate the validity of this procedure, the simulation of test case #1 was repeated, but instead of monoenergetic muons the Blanpied generator [Blanpied] was used to produce muons drawn from the simulated cosmic ray muon spectrum. Simulation of passage of these muons through the object was performed with scattering values determined using the actual muon momenta. Then muon momenta were estimated by simulating the passage of the muons through 3 plates of 5 cm thick iron. Momenta estimates were then used in the MLSD algorithm. The standard detector parameters of .016 cm RMS position resolution and 27 cm outer detector spacing were used. Figure 6.13 shows PoCA and MLSD reconstructions. The better performance of the MLSD algorithm is clear. Though the MLSD reconstruction looks very good, the performance of the algorithm is deteriorated from the monoenergetic muon, no position error case (P_{rms}=1.09 versus the previous value of 0.25) as would be expected from the Section 3.3.3 discussion.

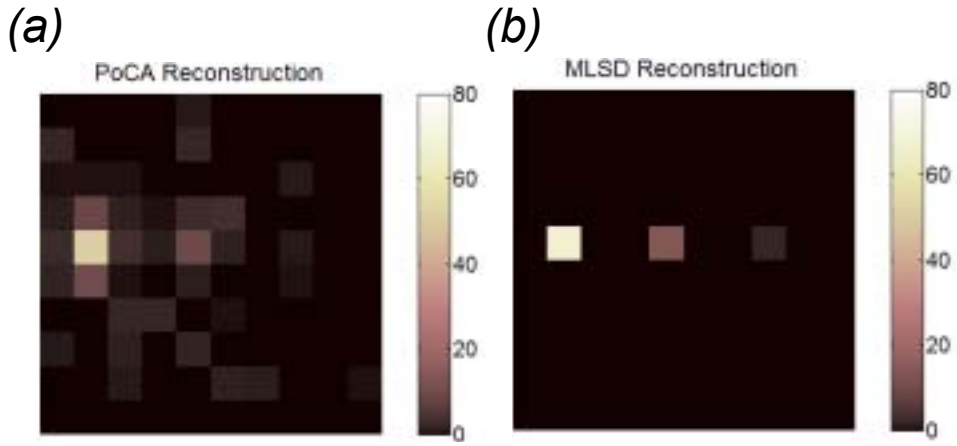

Figure 6.13 PoCA (a) and MLSD (b) reconstructions for test case #1 with varying muon momenta and nominal position error levels.

6.2.5.3 Convexity of the MLSD Cost Function

In some applications of maximum likelihood methods in medical imaging, reconstruction methods have been shown to be convex, which guarantees a global local minimum to the cost function with no local minima [46]. In the process of generating the results herein, local minima were not observed to be a problem. For many cases the algorithm was run from various different starting points (e.g., starting with homogenous air, starting from the PoCA reconstruction, starting with a randomly filled object area) and the same final reconstruction was obtained for these different seeds. However, the MLSD cost function is not a convex. This was shown numerically by observing, during the solution process, the eigenvalues of the Hessian matrix of the cost function. Though those eigenvalues are dominantly positive, there are negative eigenvalues as well, indicating directions of concave curvature. Therefore the existence of local minima cannot be ruled out.

6.2.5.4 Regularization

An investigation of regularization would be a significant effort, and application dependent, so is outside the scope of this dissertation. However, regularization should be effective when prior information about the nature of likely objects is known. For example, one heuristic regularization scheme would be to restrict the reconstructed scattering density to only the values corresponding to low, medium, or high Z material (and no material). More traditional regularization, such as total variation or square gradient methods, are also of interest. Any of these methods are easily incorporated into the MLSD framework by simply adding a weighted regularization term to the cost function. This is an item of suggested further research.

6.2.6 Summary of Extended 2D MLSD Algorithm Performance

The performance of the 2D PoCA and MLSD algorithms using variable muon momenta and nominal detector resolution were assessed by making 10 simulated runs of the each of the test cases previously discussed. The exposure time was one minute for all test cases except test case #3, where an exposure time of two minutes was used. Results are shown in Table 6.2. Performance of the MLSD algorithm, particularly in object classification, was superior in all cases.

Table 6.2 Performance Measurements for Extended 2D Test Case Reconstructions (10 runs for each case)

	P_{rms}				P_c			
	PoCA		MLSD		PoCA		MLSD	
Test Case	Mean	Std	Mean	Std	Mean	Std	Mean	Std
1	2.99	1.11	0.81	0.42	0.28	0.05	0.00	0.00
2	3.43	0.96	1.56	1.23	0.27	0.03	0.00	0.00
3	6.10	0.87	4.82	0.78	0.44	0.03	0.09	0.03
6	9.77	0.66	6.50	1.82	0.98	0.04	0.28	0.05
7	5.21	0.68	2.54	0.47	0.57	0.05	0.05	0.02

As another way to examine algorithm performance, the confidence intervals on reconstructed scattering density for the three objects of test case #1 were calculated. The true scattering densities of the uranium, iron, and concrete blocks were 78.1, 14.2, and 2.3, respectively. For the 10 MLSD runs, the ±2σ confidence intervals around the mean were [57.7, 75.2, 92.7] for the uranium block, [9.7, 13.0, 16.4] for the iron block, and [1.4, 2.1, 2.8] for the concrete block. Theory (see Appendix B) suggests that these confidence limits should be at best ±30%, so these results are as good as could be expected. For the PoCA algorithm, the values were [31.9, 62.6, 93.3], [5.7, 9.0, 12.3], and [0.1, 1.1, 2.1] for uranium, iron, and concrete, respectively.

6.3 The 3D MLSD Algorithm

6.3.1 The 3D MLSD Framework and Algorithm

The MLSD framework may be extended to 3D. The first step in expanding the 2D framework of Section 6.2.1 is to replace the 2D pixel grid covering the object area with a 3D voxel grid covering the object volume. Reconstruction of scattering density within each voxel is sought, expressed again as the vector $\hat{\boldsymbol{\lambda}}$. The ray pixel path length vectors $\mathbf{L}$ and $\mathbf{T}$ of the 2D framework are redefined to express ray path lengths through 3D voxels. As discussed in Section 3.2, scattering into two orthogonal planes may be measured for each ray: $\Delta\theta_x$ and $\Delta\theta_y$. Scattering into the y plane is i.i.d. to scattering into the x plane. Two i.i.d. measurements of displacement, Δx and Δy, are also be made. The statistical development of Section 6.2.1 applies to the 3D problem, and the covariance matrix expressed in Eqs. (6.37-40) applies to both the x plane and y plane measurements. One approach would be to simply double the size of the problem by treating the two plane measurements separately. However, if the two plane measurements are combined by defining, for ray i:

$$\Delta\theta_i^2 = \frac{\Delta\theta_{x,i}^2 + \Delta\theta_{y,i}^2}{2} \tag{6.73}$$

$$\Delta w_i^2 = \frac{\Delta x_i^2 + \Delta y_i^2}{2} \tag{6.74}$$

$$\Delta\theta w_i = \frac{\Delta\theta_{x,i}\Delta x_i + \Delta\theta_{y,i}\Delta y_i}{2} \tag{6.75}$$

then the cost function of Eq. (6.46) may be used after expanding to:

$$F\left(\hat{\boldsymbol{\lambda}}\right)=\frac{1}{M}\sum_{i=1}^{M}\left[\ln\left(\left|\hat{\boldsymbol{\Sigma}}_i\right|\right)+\frac{1}{\left|\hat{\boldsymbol{\Sigma}}_i\right|}\left(\Delta\theta_i^2 v_{w,i}-2\Delta\theta w_i s_{\theta w,i}+\Delta w_i^2 v_{\theta,i}\right)\right] \tag{6.76}$$

The 3D MLSD algorithm is listed below.

3D MLSD Algorithm

1. Establish an $NxNxN$ grid of $LxLxL$ sized voxels over the object volume. Establish a Cartesian coordinate system in three dimensions with z vertical. Measured data is $\left(x,y,z,\theta_x,\theta_y\right)_{in}$ and $\left(x,y,z,\theta_x,\theta_y\right)_{out}$ for each of M rays.
2. For $i:=1\text{ to }M$ % loop over rays
   - 2.1. $\left(\left(x,y,z,\theta_x,\theta_y\right)_{in}\right):=\left(\left(x,y,z,\theta_x,\theta_y\right)_{in}\right)_i$ % Get ray data
   - 2.2. $\left(\left(x,y,z,\theta_x,\theta_y\right)_{out}\right):=\left(\left(x,y,z,\theta_x,\theta_y\right)_{out}\right)_i$ % Get ray data
   - 2.3. $\Delta\theta_x:=\left(\theta_{x,out}-\theta_{x,in}\right)$ % Compute x scattering signal
   - 2.4. $\Delta\theta_y:=\left(\theta_{y,out}-\theta_{y,in}\right)$ % Compute y scattering signal
   - 2.5. $\bar{\theta}_x:=\left(\theta_{x,in}+\theta_{x,out}\right)/2$ % Compute average x ray angle
   - 2.6. $\bar{\theta}_y:=\left(\theta_{y,in}+\theta_{y,out}\right)/2$ % Compute average y ray angle
   - 2.7. $x_{proj}:=x_{in}+\tan\left(\theta_{x,in}\right)\cdot\left(z_{out}-z_{in}\right)$ % Compute projected un-deflected x position
   - 2.8. $y_{proj}:=y_{in}+\tan\left(\theta_{y,in}\right)\cdot\left(z_{out}-z_{in}\right)$ % Compute projected un-deflected y position
   - 2.9. $F_{xy}:=\tan^2\theta_{x,in}+\tan^2\theta_{y,in}+1$ % Compute xy adjustment factor
   - 2.10. $F_x:=\tan^2\theta_{x,in}+1$ % Compute x adjustment factor
   - 2.11. $F_y:=\tan^2\theta_{y,in}+1$ % Compute y adjustment factor
   - 2.12. $\Delta x:=\left(x_{out}-x_{proj}\right)\left(\sqrt{F_{xy}/F_x}\right)\cos\bar{\theta}_x$ % Compute x displacement
   - 2.13. $\Delta y:=\left(y_{out}-y_{proj}\right)\left(\sqrt{F_{xy}/F_y}\right)\cos\bar{\theta}_y$ % Compute y displacement
   - 2.14. $\boldsymbol{\Delta\theta}(i):=\left(\Delta\theta_x^2+\Delta\theta_y^2\right)/2$ % Compute scattering signal
   - 2.15. $\boldsymbol{\Delta w}(i):=\left(\Delta x^2+\Delta y^2\right)/2$ % Compute displacement signal
   - 2.16. $\boldsymbol{\Delta\theta w}(i):=\left(\Delta\theta_x\Delta x+\Delta\theta_y\Delta y\right)/2$ % Compute cross-term signal
   - 2.17. $[\mathbf{L},\mathbf{T}]:=raysum3D\left(x_{in},y_{in},z_{in},\theta_{x,in},\theta_{y,in},x_{out},y_{out},z_{out},\theta_{x,out},\theta_{y,out}\right)$ % Compute the estimated ray path lengths through each voxel.
   - 2.18. $\mathbf{W_\theta}(i,:):=\mathbf{L}$ % Compute row of angle weights

2.19. $\mathbf{W_{\theta x}}(i,:) := \left[L_1^2/2 + L_1 T_1 \quad L_2^2/2 + L_2 T_2 \quad \ldots \quad L_{N^2}^2/2 + L_{N^2} T_{N^2} \right]$
% Compute row of angle/displacement weights

2.20. $\mathbf{W_x}(i,:) := \left[L_1^3/3 + T_1 L_1^2 + T_1^2 L_1 \quad L_2^3/3 + T_2 L_2^2 + T_2^2 L_2 \quad \ldots \quad L_{N^2}^3/3 + T_{N^2} L_{N^2}^2 + T_{N^2}^2 L_{N^2} \right]$
% Compute row of displacement weights

3. Next i
4. $\hat{\boldsymbol{\lambda}}_0 := \lambda_{air}$ % Initialize scattering density vector to the value for air (the PoCA solution may also be used as a starting point)
5. $C_0 := fcsttx\left(\hat{\boldsymbol{\lambda}}_0, \mathbf{W_\theta}, \mathbf{W_x}, \mathbf{W_{\theta x}}, \mathbf{\Delta\theta}, \mathbf{\Delta w}, \mathbf{\Delta\theta w}\right)$ % Compute initial cost, where $fcsttx(\cdot)$ is the Eq. (6.76) cost function
6. $C_l := 1x10^{-9}$ % Set cost function reduction limit (other values might be used).
7. Do
   7.1. $[C_1, \hat{\boldsymbol{\lambda}}_1] := fmincon\left[fcsttx\left(\hat{\boldsymbol{\lambda}}_0, \mathbf{W_\theta}, \mathbf{W_x}, \mathbf{W_{\theta x}}, \mathbf{\Delta\theta}, \mathbf{\Delta w}, \mathbf{\Delta\theta w}\right), \lambda_{air} \right]$ % Compute new scattering density estimate, from start point $\hat{\boldsymbol{\lambda}}_\mathbf{0}$ with lower bound λ_{air} on all elements.
   7.2. $C_d := C_1 - C_0$ % Compute reduction in cost function
   7.3. $\hat{\boldsymbol{\lambda}}_\mathbf{0} := \hat{\boldsymbol{\lambda}}_\mathbf{1}$ % Update scattering strength estimate
   7.4. $C_0 := C_1$ % Update cost function
8. While $(C_d > C_l)$ % Loop while cost function reduction is greater than limit
9. $\hat{\boldsymbol{\lambda}}_{opt} := \hat{\boldsymbol{\lambda}}_0$ % Save last estimate as optimal estimate

6.3.2 Numerical Tests of the 3D MLSD Algorithm

In Section 4.2.4 two 3D test cases were developed for illustrating the 3D PoCA algorithm. The simulated object volume was a cube 100 cm on a side, for a total of 1000 (10 cm)^3 voxels. Monoenergetic muons were used in Section 4.2.4, but for comparison of the 3D PoCA and MLSD algorithms muon momenta were made variable, measured by 3 scattering planes as in 2D testing. Detector resolution of 0.016 cm RMS with an outer detector spacing of 100 cm was also simulated. To simulate 1 minute of exposure 100,000 muons were simulated, and about 20,000 passed through the object volume and were used for reconstruction.

Results for 3D test case #4 are shown in Figure 6.14. The upper left cube is made of concrete, the center cube of uranium, and the bottom right cube of iron. The PoCA results are deteriorated from those of Section 4.2.4 due to the addition of muon momenta spread and detector resolution. Two of the cubes were misclassified and many artifacts are apparent. The MLSD results are much better, with all cubes correctly classified and many fewer artifacts.

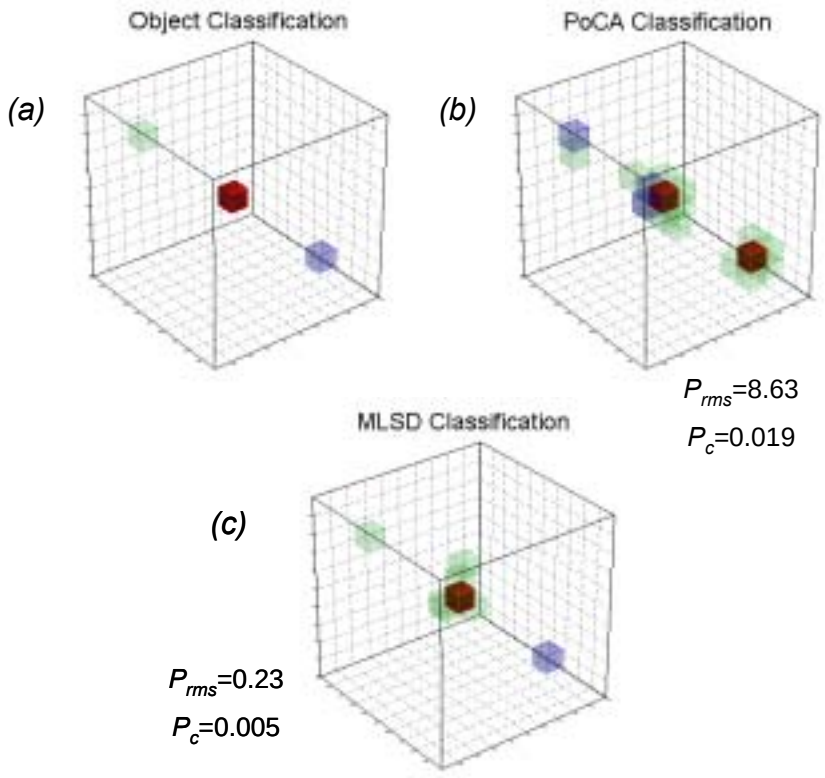

Figure 6.14 Results for 3D test case #4. The object classification (a), the PoCA classification (b), and the MLSD classification (c).

Results for 3D test case #5 are shown in Figure 6.15. This is a difficult case since the plates "shadow" one another given the vertical tending muon trajectories. The three plates are virtually indistinguishable in the PoCA reconstruction. The

MLSD reconstruction is much better, though some blurring between the plates is apparent.

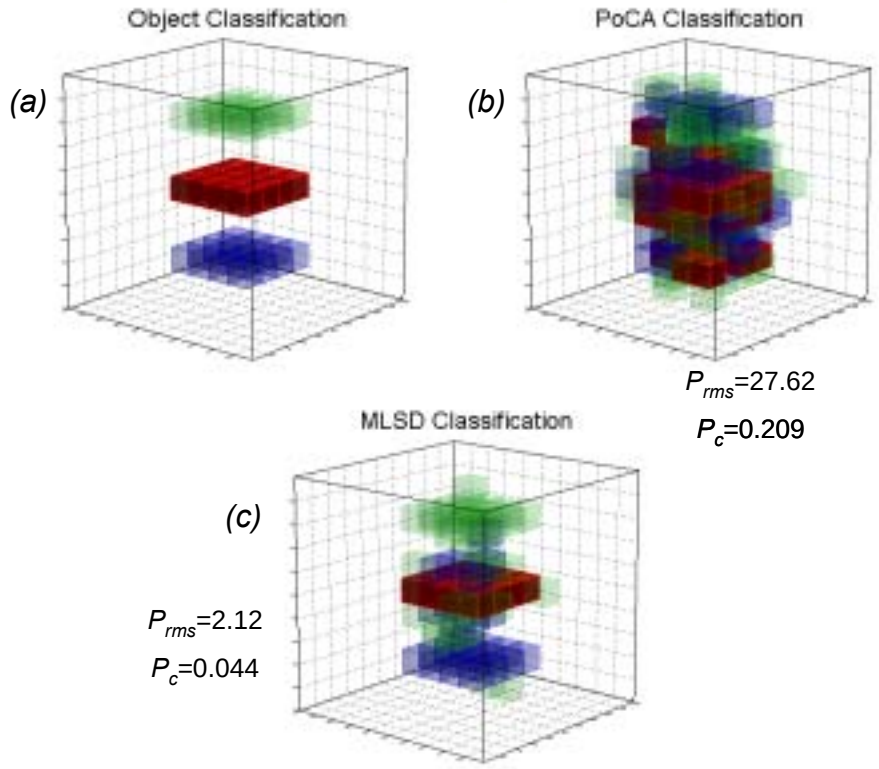

Figure 6.15 Results for 3D test case #5. The object classification (a), the PoCA classification (b), and the MLSD classification (c).

6.4 Application of MLSD to Experimental Data

Unfortunately the number of voxels and rays required to reconstruct the experimental data of Chapter 5 exceeds the memory and processing speed available in the current implementation of the MLS or MLSD algorithms in a MATLAB platform on a standard PC. The computational burden of the MLSD algorithm increases approximately proportional to the number of rays times the square of the number of voxels. The tests of the previous section involved about 20,000 rays and 1000 voxels, whereas reconstruction of the experimental data would require 100,000 rays and

several thousand voxels. Optimization of the MLSD algorithm and implementation in an appropriate platform will be required to handle this larger problem size. This is an item of future work.

6.5 Summary

In this chapter two new algorithms for the tomographic reconstruction of objects through use of the scattering of cosmic ray muons were presented. The performance of these algorithms was compared to and contrasted with the performance of the PoCA (Point of Closest Approach) algorithm of Chapter 4. The MLS (Maximum Likelihood Scattering) algorithm is a natural extension to traditional tomographic methods, and performs better than the PoCA method for simple scenes, but does not make use of all the information available from the muons, and should be considered to be primarily a pedagogical algorithm. The MLSD (Maximum Likelihood Scattering and Displacement) algorithm makes use of both muon scattering and displacement, and allows information to be localized along the path of a ray. This is of particular advantage in limited angle tomography (such as tomography using cosmic ray muons) where no horizontal views are obtainable. The MLSD algorithm was shown to perform better than the PoCA or MLS algorithms for a variety of test cases.

The iterative reconstruction framework allows for the inclusion of measurement error and other factors in the reconstruction process by folding those factors into the statistical model. The incorporation of detector resolution error and muon momentum spread into the algorithm was presented and illustrated. Regularization, though not investigated herein, could be easily incorporated into the algorithm.

A disadvantage of the MLSD algorithm relative to PoCA is that is much more consumptive of computational resources. For an application such as border crossing nuclear contraband detection effort will need to be devoted to accelerating the convergence speed of the algorithm. Using the PoCA algorithm to generate a starting condition for MLSD is appropriate, and determining a reasonable stopping condition will be important. Optimization of numerical methods, though outside the scope of this dissertation, could yield benefits. For other applications of cosmic ray muon radiography real time radiography may not be necessary, and the MLSD algorithm may be very appropriate for accurate reconstruction in such applications.

CHAPTER 7
CONCLUSION

7.1 Summary

This dissertation described key aspects of the development of an entirely new form of radiography using cosmic ray muons. Chapter 2 established the background for cosmic ray muon radiography by describing cosmic ray muons, how they are formed, how they interact, what has been previously attempted in this area, and how tomographic reconstruction works in general. In Chapter 3 the concept for multiple scattering radiography using cosmic ray muons was presented, and multiple scattering as an information source was analyzed. A new method for the measurement of muon momentum via multiple scattering was also presented (and fully analyzed in Appendix B). The tomographic framework was established in Chapter 4, and the PoCA (Point of Closest Approach) reconstruction method was presented and illustrated through simulated examples. In Chapter 5 the design of and results from an experimental proof of principle were presented. The PoCA reconstructions from experimental data presented in Chapter 5 represent the world's first cosmic ray muon radiographs made using multiple scattering. Finally, in Chapter 6 a fully tomographic reconstruction algorithm for cosmic ray muon radiography was developed. The MLSD (Maximum Likelihood Scattering and Displacement) algorithm expresses both the statistical nature of the scattering and displacement of muons and the measurement noise and

momentum uncertainty present in cosmic ray muon radiography. Results from the algorithm were presented and shown to be uniformly superior to those of PoCA.

7.2 Items for Future Research

7.2.1 Regularization

Regularization, or the incorporation of prior knowledge into the reconstruction process, is almost certain to improve reconstruction quality. Application of regularization is likely to be application specific. However, an investigation of some of the most generally effective methods of regularization would be interesting. The MLSD framework is easily extended to include regularization.

7.2.2 Application of MLSD to Nuclear Contraband Detection

The application for which much of this work was funded, as discussed briefly in Chapter 1, is the detection of nuclear contraband in vehicles and shipping containers. The size of this problem should challenge the computation efficiency of the MLSD algorithm and may demand extensive optimization of the method to obtain sufficient convergence speed.

7.2.3 MLSD with Adaptive Reconstruction Elements

For applications wherein small objects in large volumes are expected, it is a waste of resources to reconstruct many voxels that contain no material. If reconstruction elements were made adaptively resizable and locatable then fewer elements might be possible resulting in a lower computational load.

7.3 Final Remarks

The work presented herein is new and significant in two primary ways. Firstly, cosmic ray muon radiography represents a completely new mode of radiography. The

experimental radiographs in Chapter 5 are the first radiographs of small objects ever made with passive cosmic ray muons. Significant relevant applications for this technology exist. Though this development was a collaborative effort, the author's contributions to analysis and experimental proof of the concept, as detailed in this dissertation, were substantial.

Secondly, the MLSD algorithm, which is the completely individual work of the author, is a totally new tomographic reconstruction algorithm driven by the nature of multiple scattering. It is not yet known whether the principles of the MLSD algorithm might be applicable to other information sources, but that possibility exists.

LIST OF REFERENCES

[1] Hagiwara, K., et al., Particle Data Group, Review of Particle Physics, *Physical Review D* **66**(1) (2002).

[2] Borozdin, K., et al., "Radiographic Imaging with Cosmic Ray Muons", *Nature* **422**, p 277 (2003).

[3] Schwarzschild, B., "Cosmic-Ray Muons Might Help Thwart Transport of Concealed Fissile Material," *Physics Today*, **56**(5), pp 19-22 (2003).

[4] National Public Radio, "Detecting Nuclear Smugglers," *All Things Considered* radio broadcast of June 13, 2003, audio at http://discover.npr.org/features/feature.jhtml?efId=1297989 (2003).

[5] Roach, J., "Cosmic Particles could Detect Nuke Materials, Scientists Say," *National Geographic News* (March, 2003) http://news.nationalgeographic.com/news/2003/03/0319_030319_cosmicrays.html (2003).

[6] Weiss, P., "Muon Manna? Particle Shower may Spotlight Loose Nukes," *Science News Online* (March 2003), http://www.sciencenews.org/20030322/foc1.asp (2003).

[7] Priedhorsky, W., et al., "Detection of High-Z Objects Using Multiple Scattering of Cosmic Ray Muons," *Review of Scientific Instruments* **74**(10). pp 4294-7 (2003).

[8] Allkofer, O.C., and P.K.F. Grieder, "Cosmic Rays on Earth*," Fach-informations-zentrum Energie, Physik, Mathematik*, **Nr 25-1** (1984).

[9] Dar, A. "Atmospheric Neutrinos, Astrophysical Neutrons, and Proton-Decay Experiments," *Physical Review Letters* **51**(3), pp 227-230 (1983).

[10] Jokisch, H., et al., "Cosmic-ray Muon Spectrum up to 1 TeV at 75° Zenith Angle," *Physical Review D* **19**(5), pp 1368-1372 (1979).

[11] Rastin, B., "An Accurate Measurement of the Sea-Level Muon Spectrum within the Range 4 to 3000 GeV/c," *J. Phys. G: Nucl. Phys* **10**, pp 1609-1628 (1984).

[12] Motiki, M., et al., "Precise Measurement of Atmospheric Muon Fluxes at Sea Level," in *Proceedings of the ICRC 2001*, 927, Hamburg, Germany (2001).

[13] Sanuki, T., et al., "Atmospheric Muons at Various Altitudes," in *Proceedings of the ICRC 2001*, 950, Hamburg, Germany (2001).

[14] Blanpied, G., University of South Carolina, Department of Physics and Astronomy, personal communication, June, 2002.

[15] Rossi, B., *High Energy Particles*, Prentice-Hall, Inc., Englewood Cliffs, NJ (1952).

[16] George, E. P., "Cosmic Rays Measure Overburden of Tunnel," *Commonwealth Engineer*, July 1, 1955, pp 455-457 (1955).

[17] Alvarez, L.W., et al., "Search for Hidden Chambers in the Pyramids," *Science* **167,** pp 832-839 (1970).

[18] Minato, S., "Feasibility of Cosmic-Ray Radiography: A Case Study of a Temple Gate as a Testpiece," *Materials Evaluation* **46**, pp 1468-1470 (1988).

[19] Nagamine, K., "Geo-tomographic Observation of Inner-structure of Volcano with Cosmic-ray Muons," *Journal of Geography* **104**(7), pp 998-1007 (1995).

[20] Frlez, E., et al., “Cosmic Muon Tomography of Pure Cesium Iodide Calorimeter Crystals,” *Nuclear Instruments and Methods in Physics Research A* **440**, pp 57-85 (2000).

[21] King, N.S.P, et al., “An 800-MeV Proton Radiography Facility for Dynamic Experiments,” *Nuclear Instruments and Methods in Physics Research A* **424**, pp 84-91 (1999).

[22] Charpak, G., et al., “Applications of 3-D Nuclear Scattering Radiography in Technology and Medicine,” *Proceedings of the Society of Photo-optical Instrumentation Engineers* **312**, pp 156-163 (1983).

[23] Kak, A.C., and M. Slaney, *Principles of Computerized Tomographic Imaging*, SIAM, Philadelphia, PA (2001).

[24] Hounsfield, G.N., "A Method of and apparatus for examination of a body by radiation such as x-ray or gamma radiation", *British Patent Number 1283915* (1972).

[25] Vixie, K.R., Los Alamos National Laboratory, personal communication, January, 2003.

[26] Gordon, R., “A Tutorial on ART,” *IEEE Transactions on Nuclear Science*, **NS-21**, pp 78-93 (1974).

[27] Widrow, B., and S. D. Stearns, *Adaptive Signal Processing*, Prentice-Hall, Inc., Upper Saddle River, N.J. (1985).

[28] Haykin, S., *Adaptive Filter Theory*, Prentice-Hall, Inc., Upper Saddle River, NJ (1996).

[29] Moliere, G., “Theorie der Streuung Schneller Geladener Teilchen-II Mehrfachstreuung und Vielfachstreuung,” *Zeitschrift fur Naturcorschung Section A-A Journal of Physical Sciences* **3**(2), pp 78-97 (1948).

[30] Bethe, H.A., "Moliere's Theory of Multiple Scattering," *Physical Review* **89**(6), pp 1256-1266 (1953).

[31] Scott, W.T., "The Theory of Small-Angle Multiple Scattering of Fast Charged Particles," *Review of Modern Physics* **35**(2), pp 231-313 (1963).

[32] Lynch, G.R., and O.I. Dahl, "Approximations to Multiple Coulomb Scattering," *Nuclear Instruments and Methods in Physics Research B* **58**, pp 6-10 (1991).

[33] Papoulis, A., *Probability, Random Variables, and Stochastic Processes*, McGraw-Hill, Boston, MA (1991).

[34] Ambrosio, M., et al., "Muon Energy Estimate through Multiple Scattering with the MACRO detector," *Nuclear Instruments and Methods in Physics Research A* **492**, pp 376-386 (2002).

[35] Schultz, L.J., et al., "Image Reconstruction and Material Z Discrimination via Cosmic Ray Muon Radiography," *Nuclear Instruments and Methods in Physics Research A,* in press (2003).

[36] Lestone, J.P., "Challenges Associated with using Cosmic-ray Muons to Identify High-Z Material in 3-D Objects," Los Alamos National Laboratory Technical Report LA-UR-03-0091 (2003).

[37] Frauenfelder, H., and E. M. Henley, *Subatomic Physics*, Prentice-Hall, Inc., Upper Saddle River, N.J. (1991).

[38] Charpak, G., D. Rahm, and H. Steiner, "Some Developments in the Operation of Multiwire Proportional Chambers," *Nuclear Instruments and Methods* **80**, pp 13-34 (1970).

[39] Breskin, A., G. Charpak, and F. Sauli, "A Solution to the Right-Left Ambiguity in Drift Chambers," *Nuclear Instruments and Methods* **151**, pp 473-476 (1978).

[40] Morris, C. L., H. A. Thiessen, and G. W. Hoffman, "Position-Sensitive Gas Proportional Chambers," *IEEE Transactions on Nuclear Science*, **NS-25**(1), pp 141-143 (1978).

[41] Morris, C. L., Los Alamos National Laboratory, personal communication, September, 2003.

[42] Hogan, G. E., "PC DAQ : A Personal Computer Based Data Acquisition System," Los Alamos National Laboratory Technical Report LA-UR-98-4531 (1998).

[43] Breskin, A., "Further Results on the Operation of High-Accuracy Drift Chambers," *Nuclear Instruments and Methods* **119**, pp 9-28 (1974).

[44] Schultz, L.J., et al., "Cosmic Ray Muon Radiography for Contraband Detection," in *Proceedings of AccApp'03*, in press, San Diego, CA, June (2003).

[45] The Mathworks, *Optimization Toolbox User's Guide,* The Mathworks, Natick, MA (2003).

[46] Vardi, Y., L.A. Shepp, and L. Kaufman, "A Statistical Model for Positron Emission Tomography," *Journal of the American Statistical Association* **80**:389, pp 8-20 (1985).

APPENDIX A
BLANPIED MUON GENERATOR

The cosmic ray muon flux may be empirically described in terms of muon momentum[9] and arrival (zenith) angle, as introduced in Chapter 2. For Monte Carlo simulation of cosmic ray muon radiography, it is desirable to have the ability to randomly generate muons with momenta and arrival angle congruent with that spectrum. In support of the LANL muon radiography effort Gary Blanpied of the University of South Carolina developed a software muon generator [14]. The author participated in the testing and fine-tuning of this software. A summary of the generator and its validation appear in this appendix.

The generator is based on a model of pion→muon decay at an altitude of 15 km and survival rate of muons passing through the atmosphere to sea level. The physics were modeled after [9], with some empirical tweaking of parameters to match published muon flux data.

At the root of the model is the generation of a lookup table version of the differential spectrum $D(E,\theta)$ in [$cm^{-2}\cdot sr^{-1}\cdot sec^{-1}\cdot GeV^{-1}$]. Two major experimental datasets exist within the literature tabulating $D(E,\theta=0^0)$ [11] and $D(E,\theta=75^0)$ [10]. Figure A.1 shows the differential spectra from the Blanpied model against

[9] For cosmic ray muons, momentum and energy are virtually identical, and in this discussion energy will sometimes be used in place of momentum.

experimental data. The agreement is fairly good, although the under prediction at low energies is a bit disturbing, since muons from this low energy portion will scatter more. Improving the model at low energies is an item for future work.

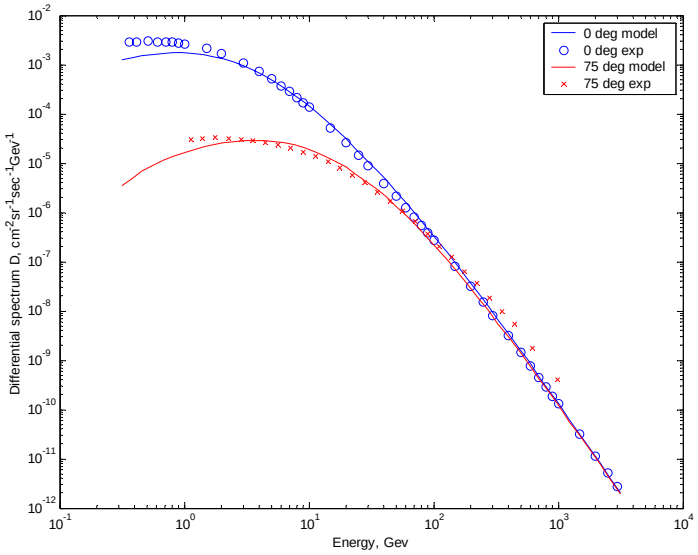

Figure A.1 Comparison of differential muon spectra from model with experimental data.

An oft quoted "rule of thumb" is that the spectra with respect to zenith angle is roughly proportional to $\cos^2(\theta)$ for energies near the mean (about 3-4 GeV). Plotted in Figure A.2 is the model generated differential spectrum against zenith angle for 4 GeV energy muons. Also shown is an appropriately weighted $\cos^2(\theta)$ curve, showing approximate agreement.

However, Figure A.2 does not represent the true spectrum for zenith angle in a spherical coordinate system due to solid angle effect. The zenith angle spectrum from the model, adjusted for solid angle, is shown in Figure A.3. Because of the solid angle effect, the mean zenith angle is about 35°, with no muons arriving at a 0° angle.

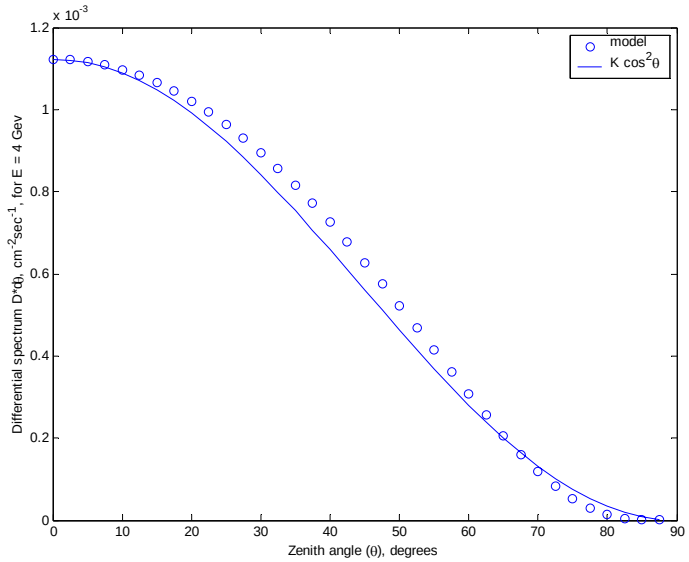

Figure A.2 Model differential muon spectrum wrt zenith angle for E = 4 GeV.

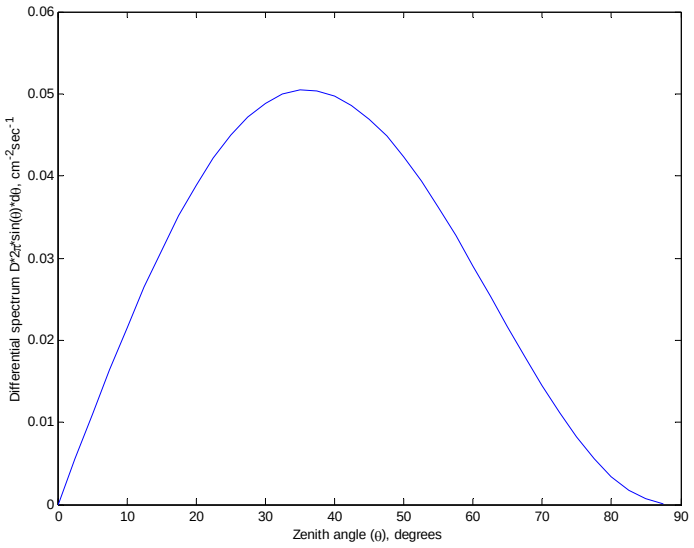

Figure A.3 Model differential muon spectrum wrt zenith angle, adjusted for solid angle.

To deal with the coupled distribution in generating muons, the model first selects a zenith angle θ, and then selects an energy E based on the selected θ. To do this, the differential spectrum is integrated across the total E range, and is then

multiplied by $2\pi\sin(\theta)$ to incorporate the effect of solid angle. This result is converted to a normalized table wherein a random number [0,1] is used to select a θ. To select E, the differential spectrum is integrated and normalized within each θ bin to produce an E selection table for each θ bin. After selecting θ, the appropriate E table is used to select E.

Previous plots have shown the differential spectrum from which muons are drawn. A dataset of 1 million muons was produced from the model. A distribution of energy of those muons is shown in Figure A.4. The distribution does not look like the one shown in Figure A.1, but does after adjusting for bin size, as shown in Figure A.5.

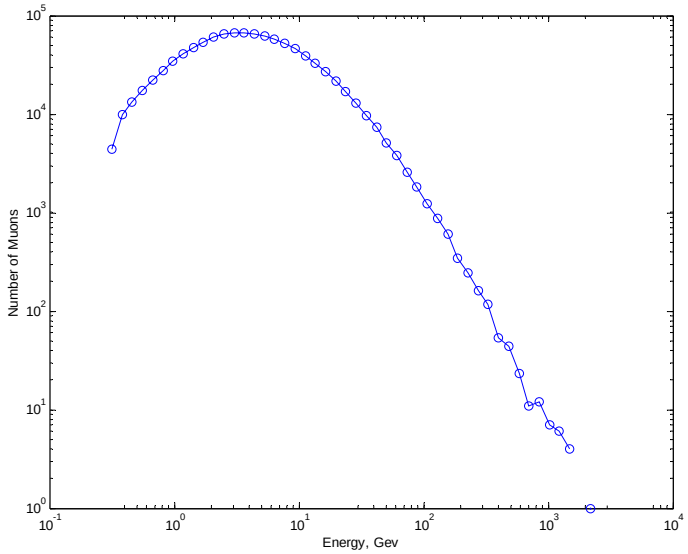

Figure A.4 Energy distribution of 1,000,000 muons drawn from generator.

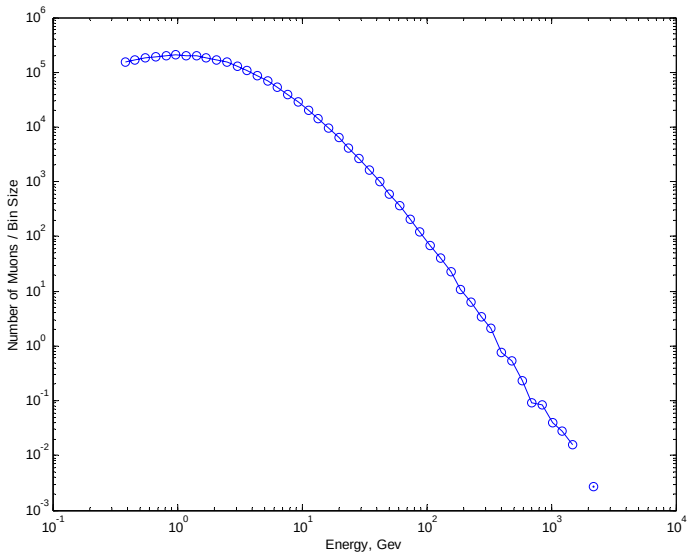

Figure A.5 Energy distribution of 1,000,000 muons, adjusted for bin size.

Finally, a histogram of zenith angles of the 1 million muons is shown in Figure A.6. This distribution matches that shown in Figure A.3.

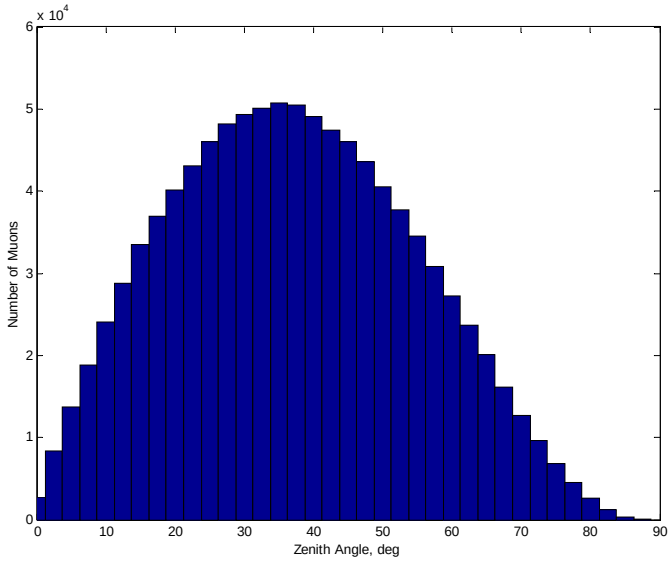

Figure A.6 Distribution of zenith angles of 1,000,000 muons drawn from generator.

In summary, the results from muons drawn from the Blanpied generator are congruent with the underlying differential spectra model. That model matches

experimental data fairly well, with modest under prediction of the rate of low energy (<1 GeV) muons. This problem at low energies should be investigated, but the results were judged to be adequate for use at the present time.

APPENDIX B
MUON MOMENTUM MEASUREMENT BY MULTIPLE SCATTERING

In Section 3.3.3 the idea of measuring muon momentum by measuring multiple scattering through a known piece of material was introduced. In this appendix the uncertainty in muon momentum measurement and the resultant uncertainty in measuring the scattering density of unknown material will be addressed.

B.1 Inferring Material via Scattering of Particles with Estimated Momentum.

Referring to Figure 2.4, let us pass N particles vertically through the material. For each particle we have θ_i, the plane scattering angle, and p_i, the particle momentum. Scattering is normally distributed with zero mean and standard deviation:

$$\sigma_{\theta_i} = \frac{15}{p_i}\sqrt{\frac{L}{L_{rad}}} \tag{B.1}$$

Assume that θ_i is measured perfectly, but estimates of momentum are made characterized as follows:

$\hat{p}_i$: Estimated particle momentum.
$\Delta p_i = \hat{p}_i - p_i$: Error in momentum estimate.
$\frac{\Delta p_i}{p_i}$: Fractional error of momentum estimate.
$\frac{\hat{p}_i}{p_i}$: Momentum estimate ratio.
E_p: RMS of fractional error of momentum estimates.
$E\left(\frac{\Delta p}{p}\right) = 0$: Momentum estimate is unbiased.

$$E\left[\left(\frac{\hat{p}}{p}\right)^n\right] \equiv M_{np} : n^{th} \text{ moment of momentum estimate ratio.}$$

$$E\left[\left(\frac{\Delta p}{p}\right)^2\right] = E\left[\left(\frac{\hat{p}}{p}\right)^2\right] - 1 = M_{2p} - 1 = E_p^2$$

Each scattering measurement will be normalized to account for varying particle momentum:

p_0 : Arbitrary "nominal" particle momentum

$\theta_{r,i} = \theta_i \frac{p_i}{p_0}$: "Real" normalized scattering (unobserved)

$\theta_{n,i} = \theta_i \frac{\hat{p}_i}{p_0}$: Estimated normalized scattering

Define the normalized scattering standard deviation:

$$\sigma_0 = \sigma_{\theta_r} = \left(\frac{15}{p_i}\sqrt{\frac{L}{L_{rad}}}\right)\frac{p_i}{p_0} = \frac{15}{p_0}\sqrt{\frac{L}{L_{rad}}} \tag{B.2}$$

We wish to infer normalized scattering tendency from measured scattering to infer material composition. Note that:

$$\theta_{n,i} = \theta_{r,i}\frac{\hat{p}_i}{p_i} \tag{B.3}$$

Define the signal to be

$$S = \frac{1}{N}\sum_{i=1}^{N}\theta_{n,i}^2 = \frac{1}{N}\sum_{i=1}^{N}\left(\theta_{r,i}^2\frac{\hat{p}_i^2}{p_i^2}\right) \tag{B.4}$$

What are the statistics of S? First deriving the mean:

$$E(S) = E\left[\frac{1}{N}\sum_{i=1}^{N}\left(\theta_{r,i}^2\frac{\hat{p}_i^2}{p_i^2}\right)\right] = \frac{1}{N}\sum_{i=1}^{N}E\left(\theta_{r,i}^2\frac{\hat{p}_i^2}{p_i^2}\right) \tag{B.5}$$

$$E(S)=\frac{1}{N}\sum_{i=1}^{N}\left[E\left(\theta_{r,i}^2\right)\cdot E\left(\frac{\hat{p}_i^{\,2}}{p_i^2}\right)\right]=\frac{1}{N}\sum_{i=1}^{N}\left[E\left(\theta_r^2\right)\cdot E\left(\frac{\hat{p}^2}{p^2}\right)\right] \tag{B.6}$$

$$E(S)=E\left(\theta_r^2\right)\cdot E\left(\frac{\hat{p}^2}{p^2}\right)=\sigma_0^2\cdot M_{2p} \tag{B.7}$$

So the signal S is a biased estimator of σ_0^2, and scattering and thus material density will be overestimated. To avoid this, redefine the signal as:

$$S=\frac{1}{M_{2p}N}\sum_{i=1}^{N}\theta_{n,i}^2 \tag{B.8}$$

which is an unbiased estimator of σ_0^2.

Next, derive the variance of this new signal:

$$V(S)=E\left(S^2\right)-E^2(S)=E\left(S^2\right)-\sigma_0^4 \tag{B.9}$$

$$E\left(S^2\right)=E\left(\left[\frac{1}{M_{2p}N}\sum_{i=1}^{N}\theta_{n,i}^2\right]^2\right)=\frac{1}{M_{2p}^2N^2}E\left(\left[\sum_{j=1}^{N}\theta_{n,j}^2\sum_{i=1}^{N}\theta_{n,i}^2\right]\right) \tag{B.10}$$

$$E\left(S^2\right)=\frac{1}{M_{2p}^2N^2}\sum_{j=1}^{N}\sum_{i=1}^{N}E\left(\theta_{n,j}^2\theta_{n,i}^2\right) \tag{B.11}$$

$$E\left(S^2\right)=\frac{1}{M_{2p}^2N^2}\left[\sum_{i=1}^{N}E\left(\theta_{n,i}^4\right)+N\sum_{i=1}^{N-1}E^2\left(\theta_{n,i}^2\right)\right] \tag{B.12}$$

$$E\left(S^2\right)=\frac{1}{M_{2p}^2N^2}\left[N\cdot E\left(\theta_r^4\frac{\hat{p}^4}{p^4}\right)+N(N-1)\cdot E^2\left(\theta_r^2\frac{\hat{p}^2}{p^2}\right)\right] \tag{B.13}$$

$$E\left(S^2\right)=\frac{1}{M_{2p}^2N}\left[E\left(\theta_r^4\right)E\left(\frac{\hat{p}^4}{p^4}\right)+(N-1)\cdot E^2\left(\theta_r^2\right)E^2\left(\frac{\hat{p}^2}{p^2}\right)\right] \tag{B.14}$$

$$E\left(S^2\right)=\frac{1}{M_{2p}^2N}\left[3\sigma_0^4M_{4p}+(N-1)\cdot\sigma_0^4M_{2p}^2\right] \tag{B.15}$$

$$E\left(S^2\right)=\frac{\sigma_0^4}{M_{2p}^2N}\left[3\cdot M_{4p}+(N-1)\cdot M_{2p}^2\right] \tag{B.16}$$

$$E\left(S^2\right)=\frac{3\sigma_0^4}{N}\frac{M_{4p}}{M_{2p}^2}+\frac{\sigma_0^4(N-1)}{N} \tag{B.17}$$

$$V(S) = \frac{3\sigma_0^4}{N}\frac{M_{4p}}{M_{2p}^2} + \frac{\sigma_0^4(N-1)}{N} - \sigma_0^4 \tag{B.18}$$

$$V(S) = \frac{3\sigma_0^4}{N}\frac{M_{4p}}{M_{2p}^2} - \frac{\sigma_0^4}{N} \tag{B.19}$$

$$V(S) = \frac{2\sigma_0^4}{N}\left[\frac{1}{2}\left(3\frac{M_{4p}}{M_{2p}^2} - 1\right)\right] \tag{B.20}$$

Finally, expressing the fractional precision of the signal estimate:

$$\frac{\Delta S}{S} = \frac{\sqrt{V(S)}}{E(S)} \tag{B.21}$$

$$\frac{\Delta S}{S} = \frac{\sqrt{V(S)}}{\sigma_0^2} \tag{B.22}$$

$$\frac{\Delta S}{S}_{general} = \sqrt{\frac{2}{N}} \cdot \sqrt{\frac{1}{2}\left(3\frac{M_{4p}}{M_{2p}^2} - 1\right)} \tag{B.23}$$

When momentum is known perfectly the expression under the second radical goes to one, resulting in the familiar expression:

$$\frac{\Delta S}{S}_{\hat{p}=p} = \sqrt{\frac{2}{N}} \tag{B.24}$$

B.2 Using Scattering to Estimate Momentum

If measurement of momentum is achieved by making M measurements of scattering of a single particle through a known piece of material, we may write

$$\sigma_\theta = \frac{K}{p} \tag{B.25}$$

$$p = \frac{K}{\sigma_\theta} \tag{B.26}$$

$$s = \sqrt{\sum_{i=1}^{M}\frac{\theta_i^2}{M}} \tag{B.27}$$

$$\hat{p} = \frac{K}{s} \tag{B.28}$$

Let

$$x = \frac{Ms^2}{\sigma_\theta^2} \tag{B.29}$$

The distribution of x is $\mathrm{X}^2(M)$ [33].

$$f_x(x) = \frac{1}{2^{M/2}\Gamma(M/2)} x^{M/2-1} e^{-x/2} u(x) \tag{B.30}$$

where $u(x)$ is the unit step, and the gamma function is defined as:

$$\Gamma(a) = \int_0^\infty y^{a-1} e^{-y} dy \tag{B.31}$$

Rewriting the momentum estimate in terms of x:

$$\hat{p} = \sqrt{\frac{MK^2}{x\sigma_\theta^2}} = p\sqrt{\frac{M}{x}} \tag{B.32}$$

For an unbiased estimate, $E(\hat{p}) = p$, so we check the expected value of the estimate.

$$E(\hat{p}) = \int_0^\infty p\sqrt{\frac{M}{x}} f_x(x) dx \tag{B.33}$$

$$E(\hat{p}) = \frac{p\sqrt{M}}{2^{M/2}\Gamma(M/2)} \int_0^\infty x^{-1/2} x^{M/2-1} e^{-x/2} dx \tag{B.34}$$

Let $z = x/2$ and substitute into Eq. (B.34):

$$E(\hat{p}) = \frac{2p\sqrt{M}\,2^{M/2-1/2-1}}{2^{M/2}\Gamma(M/2)} \int_0^\infty x^{M/2-1/2-1} e^{-z} dz \tag{B.35}$$

$$E(\hat{p}) = p\sqrt{\frac{M}{2}} \cdot \frac{\Gamma(M/2-1/2)}{\Gamma(M/2)} \tag{B.36}$$

So the momentum estimate is biased. Define the correction factor:

$$F = \frac{\Gamma(M/2)}{\Gamma(M/2-1/2)} \cdot \sqrt{\frac{2}{M}} \tag{B.37}$$

and redefine the momentum estimate to be unbiased as:

$$\hat{p} = F\frac{K}{s} = pF\sqrt{\frac{M}{x}} \tag{B.38}$$

For the unbiased estimator,

$$E\left(\frac{\Delta p}{p}\right) = 0 \tag{B.39}$$

To apply these results to the derivation of Section B.1, additional moments are required. The second moment is:

$$E\left[\left(\frac{\hat{p}}{p}\right)^2\right] = \int_0^\infty \frac{F^2 M}{x} f_x(x)dx \tag{B.40}$$

$$E\left[\left(\frac{\hat{p}}{p}\right)^2\right] = \frac{F^2 M}{2^{M/2}\Gamma(M/2)}\int_0^\infty x^{-1}x^{M/2-1}e^{-x/2}dx \tag{B.41}$$

$$E\left[\left(\frac{\hat{p}}{p}\right)^2\right] = \frac{2F^2 M 2^{M/2-2}}{2^{M/2}\Gamma(M/2)}\int_0^\infty z^{M/2-1-1}e^{-z}dz \tag{B.42}$$

$$E\left[\left(\frac{\hat{p}}{p}\right)^2\right] = F^2\frac{M}{2}\cdot\frac{\Gamma(M/2-1)}{\Gamma(M/2)} \tag{B.43}$$

Applying the identity $\Gamma(a+1) = a\cdot\Gamma(a)$,

$$E\left[\left(\frac{\hat{p}}{p}\right)^2\right] = F^2\frac{M}{2}\cdot\frac{1}{M/2-1} \tag{B.44}$$

$$E\left[\left(\frac{\hat{p}}{p}\right)^2\right] = F^2\frac{M}{M-2}, \qquad M > 2 \tag{B.45}$$

The fourth moment is:

$$E\left[\left(\frac{\hat{p}}{p}\right)^4\right] = F^4 M^2 \int_0^\infty x^{-2} f_x(x) dx \tag{B.46}$$

$$E\left[\left(\frac{\hat{p}}{p}\right)^4\right] = \frac{F^4 M^2}{2^{M/2}\Gamma(M/2)} \int_0^\infty x^{M/2-2-1} e^{-x/2} dx \tag{B.47}$$

$$E\left[\left(\frac{\hat{p}}{p}\right)^4\right] = \frac{2F^4 M^2 2^{M/2-2-1}}{2^{M/2}\Gamma(M/2)} \int_0^\infty z^{M/2-2-1} e^{-z} dz \tag{B.48}$$

$$E\left[\left(\frac{\hat{p}}{p}\right)^4\right] = \frac{F^4 M^2 2^{M/2-2}}{2^{M/2}\Gamma(M/2)} \int_0^\infty z^{M/2-2-1} e^{-z} dz \tag{B.49}$$

$$E\left[\left(\frac{\hat{p}}{p}\right)^4\right] = F^4 \frac{M^2}{2^2} \frac{\Gamma(M/2-2)}{\Gamma(M/2)} \tag{B.50}$$

$$E\left[\left(\frac{\hat{p}}{p}\right)^4\right] = F^4 \frac{M^2}{2^2} \frac{1}{(M/2-2)(M/2-1)} \tag{B.51}$$

$$E\left[\left(\frac{\hat{p}}{p}\right)^4\right] = F^4 \frac{M^2}{(M-4)(M-2)} \qquad M > 4 \tag{B.52}$$

B.3 Inferring Material via Scattering of Particles with Momentum also Estimated via Scattering

Inserting the result of section B.2 into the results from section B.1:

$$\frac{\Delta S}{S} = \sqrt{\frac{2}{N}} \cdot \sqrt{\frac{1}{2}\left(3\frac{M_{4p}}{M_{2p}^2} - 1\right)} \tag{B.53}$$

$$\frac{\Delta S}{S} = \sqrt{\frac{2}{N}} \cdot \sqrt{\frac{1}{2}\left(3\frac{F^4 \dfrac{M^2}{(M-4)(M-2)}}{\left(F^2 \dfrac{M}{M-2}\right)^2} - 1\right)} \tag{B.54}$$

$$\frac{\Delta S}{S} = \sqrt{\frac{2}{N}} \cdot \sqrt{\frac{1}{2}\left(3\frac{M-2}{M-4} - 1\right)} \tag{B.55}$$

$$\frac{\Delta S}{S} = \sqrt{\frac{2}{N}} \cdot \sqrt{\frac{M-1}{M-4}}, \qquad M > 4 \tag{B.56}$$

The final equation Eq. (B.56) represents the uncertainty in estimating material mean square scattering by making N scattering measurements of particles passing through the unknown material and normalizing with momentum estimated by making M scattering measurements of each particle through known material.

Eq. (B.8) requires a finite second moment of momentum uncertainty to remove bias from the scattering estimate. Eq. (B.45) shows that the adjustment factor is finite only when $M > 2$, so the methods discussed in this appendix require at least two scattering measurements for momentum inference. Eq. (B.56) shows that the signal uncertainty is finite only for $M > 4$. However, simulated tests show that reasonable results can be obtained using $M = 4$ if an upper bound is established for inferred momentum. Using an upper bound of 25 GeV $\Delta S/S_{M=4}$ was found to be about 1.5 times $\Delta S/S_{M=6}$.

APPENDIX C
DERIVATION OF JACOBIAN AND HESSIAN OF COST FUNCTIONS FOR MLS AND MLSD ALGORITHMS

In this appendix the derivation of Jacobian and Hessian matrices required for the Newton-type method minimization of MLS and MLSD algorithm cost functions will be presented.

C.1 Jacobian and Hessian for the MLS Cost Function

Consider a general cost function which is a sum of N elements, where each element is function of a differently weighted sum of elements in an M element parameter vector $\mathbf{x}$

$$C(\mathbf{x}) = \sum_{i=1}^{N} F(\mathbf{W_i} \cdot \mathbf{x}) \tag{C.1}$$

The Jacobian vector of $C(\mathbf{x})$ will be denoted $\mathbf{J}(\mathbf{x})$ and is defined as the vector of partial derivatives:

$$\mathbf{J}(\mathbf{x}) = \left[\frac{\partial C}{\partial x_1} \quad \frac{\partial C}{\partial x_2} \quad \ldots \quad \frac{\partial C}{\partial x_M} \right]^T \tag{C.2}$$

If τ is a scalar and $\mathbf{v}$ is an arbitrary M element direction vector, the directional derivative of $C(\mathbf{x}+\tau\mathbf{v})$ at $\mathbf{x}$ in the direction $\mathbf{v}$ is related to the Jacobian matrix as [Vogel]:

$$\frac{d}{d\tau} C(\mathbf{x}+\tau\mathbf{v})\Big|_{\tau=0} = \mathbf{J}(\mathbf{x}) \cdot \mathbf{v} \tag{C.3}$$

The left side of Eq. (C.3) is the directional derivative, and the right side is the inner product of the Jacobian vector and the direction vector. Expanding Eq. (C.1),

$$C(\mathbf{x}+\tau\mathbf{v}) = \sum_{i=1}^{N} F\left[\mathbf{W_i}\cdot(\mathbf{x}+\tau\mathbf{v})\right] \tag{C.4}$$

The directional derivative is:

$$\left.\frac{dC}{d\tau}(\mathbf{x}+\tau\mathbf{v})\right|_{\tau=0} = \sum_{i=1}^{N} F'(\mathbf{W_i}\cdot\mathbf{x})\mathbf{W_i}\cdot\mathbf{v} \tag{C.5}$$

where $F'(\tilde{z}) \equiv dF/dz\big|_{z=\tilde{z}}$. The right side of Eq. (C.5) may be placed in the form of the desired inner product by creating the matrix $\mathbf{W}$ whose i^{th} row is $\mathbf{W}_i^T$ and the vector $\mathbf{F'}$ whose i^{th} element is $F'(\mathbf{W}_1\cdot\mathbf{x})$ and proceeding as:

$$\left.\frac{dC}{d\tau}(\mathbf{x}+\tau\mathbf{v})\right|_{\tau=0} = \mathbf{F'^T}\,\mathbf{W}\mathbf{v} \tag{C.6}$$

$$\left.\frac{dC}{d\tau}(\mathbf{x}+\tau\mathbf{v})\right|_{\tau=0} = (\mathbf{W}^T\mathbf{F'})\cdot\mathbf{v} \tag{C.7}$$

From which the Jacobian vector may be extracted, using Eq. (C.3):

$$\mathbf{J(x)} = \mathbf{W}^T\mathbf{F'} \tag{C.8}$$

The Hessian matrix of $C(\mathbf{x})$ will be denoted $\mathbf{H}(\mathbf{x})$ and is an MxM matrix with elements defined as:

$$[\mathbf{H}(\mathbf{x})]_{ij} = \frac{\partial^2 C}{\partial x_i \partial x_j} \tag{C.9}$$

The Hessian may be expressed in terms of the second variation of $C(\mathbf{x})$ as [Vogel]:

$$\left.\frac{\partial^2 C}{\partial\tau\partial\xi}(\mathbf{x}+\tau\mathbf{v}+\xi\mathbf{w})\right|_{\tau,\xi=0} = [\mathbf{H}(\mathbf{x})\mathbf{v}]\cdot\mathbf{w} \tag{C.10}$$

Evaluating the second variation:

$$\frac{\partial^2 C}{\partial\tau\partial\xi}\left(\mathbf{x}+\tau\mathbf{v}+\xi\mathbf{w}\right)\Big|_{\tau,\xi=0} = \sum_{i=1}^{N} F''\left[\mathbf{W_i}\cdot\mathbf{x}\right]\left(\mathbf{W_i}\cdot\mathbf{v}\right)\left(\mathbf{W_i}\cdot\mathbf{w}\right) \tag{C.11}$$

where $F''(\tilde{z}) \equiv d^2F/dz^2\Big|_{z=\tilde{z}}$. Using the aggregate weight matrix $\mathbf{W}$ as previously, and defining the vector $\mathbf{F''}$ whose i^{th} element is $F''(\mathbf{W}_1\cdot\mathbf{x})$,

$$\frac{\partial^2 C}{\partial\tau\partial\xi}\left(\mathbf{x}+\tau\mathbf{v}+\xi\mathbf{w}\right)\Big|_{\tau,\xi=0} = \left(\mathbf{Ww}\right)^T diag(\mathbf{F''})\left(\mathbf{Wv}\right) \tag{C.12}$$

where $diag(\mathbf{F''})$ denotes the NxN diagonal matrix whose diagonal elements are the elements of $\mathbf{F''}$.

$$\frac{\partial^2 C}{\partial\tau\partial\xi}\left(\mathbf{x}+\tau\mathbf{v}+\xi\mathbf{w}\right)\Big|_{\tau,\xi=0} = \mathbf{w}^T\left(\mathbf{W}^T diag(\mathbf{F''})\mathbf{W}\right)\mathbf{v} \tag{C.13}$$

$$\frac{\partial^2 C}{\partial\tau\partial\xi}\left(\mathbf{x}+\tau\mathbf{v}+\xi\mathbf{w}\right)\Big|_{\tau,\xi=0} = \left[\left(\mathbf{W}^T diag(\mathbf{F''})\mathbf{W}\right)\mathbf{v}\right]\cdot\mathbf{w} \tag{C.14}$$

From Eq. (C.14) and Eq. (C.10), the Hessian matrix may be expressed as:

$$\mathbf{H}(\mathbf{x}) = \mathbf{W}^T diag(\mathbf{F''})\mathbf{W} \tag{C.15}$$

So the calculation of Jacobian and Hessian matrices is reduced simply to calculation of the $\mathbf{F'}$ and $\mathbf{F''}$ vectors for a particular function $F(\cdot)$ then using Eqs. (C.8,15).

The cost function for the MLS algorithm is:

$$C(\mathbf{x}) = \sum_{i=1}^{N}\left[\ln(\mathbf{W_i x}) + \frac{s_i^2}{\mathbf{W_i x}}\right] \tag{C.16}$$

The function $F(\cdot)$ is:

$$F(\mathbf{W_i x}) = \ln(\mathbf{W_i x}) + \frac{s_i^2}{\mathbf{W_i x}} \tag{C.17}$$

Expressions for the elements of the vectors $\mathbf{F'}$ and $\mathbf{F''}$ are simply calculated:

$$\mathbf{F'}_i = \frac{1}{\mathbf{W_i x}} - \frac{s_i^2}{(\mathbf{W_i x})^2} \tag{C.18}$$

$$\mathbf{F''}_i = -\frac{1}{(\mathbf{W_i x})^2} + \frac{2s_i^2}{(\mathbf{W_i x})^3} \tag{C.19}$$

Eqs. (C.8,18) define the Jacobian, and Eqs. (C.15,19) the Hessian for the MLS algorithm.

C.2 Jacobian and Hessian for the MLSD Algorithm

The cost function for the MLSD algorithm is of the form:

$$C(\mathbf{x}) = \sum_{i=1}^{N} \left[\ln\left(\left| \hat{\mathbf{\Sigma}}_i \right| \right) + \mathbf{d}_i^{\mathrm{T}} \hat{\mathbf{\Sigma}}_i^{-1} \mathbf{d}_i \right] \tag{C.20}$$

where $\mathbf{d}_i = \begin{bmatrix} \theta_i & x_i \end{bmatrix}^T$ is a data vector and

$$\hat{\mathbf{\Sigma}}_i = \begin{bmatrix} \hat{\mathbf{v}}_{\theta i} & \hat{\mathbf{s}}_{\theta x i} \\ \hat{\mathbf{s}}_{\theta x i} & \hat{\mathbf{v}}_{x i} \end{bmatrix} = \begin{bmatrix} \mathbf{W}_{\theta i} \cdot \mathbf{x} & \mathbf{W}_{\theta x i} \cdot \mathbf{x} \\ \mathbf{W}_{\theta x i} \cdot \mathbf{x} & \mathbf{W}_{x i} \cdot \mathbf{x} \end{bmatrix} \tag{C.21}$$

The cost function is thus a summation of a function of three different weighting of $\mathbf{x}$.

The Jacobian in this case is:

$$\mathbf{J(x)} = \mathbf{W}_\theta^T \mathbf{F}_\theta' + \mathbf{W}_{\theta x}^T \mathbf{F}_{\theta x}' + \mathbf{W}_x^T \mathbf{F}_x' \tag{C.22}$$

where $\mathbf{W}_\theta, \mathbf{W}_{\theta x}, \mathbf{W}_x$ are aggregate weight matrices constructed as was $\mathbf{W}$ in Section C.1. $\mathbf{F}_\theta'$ is a vector whose i^{th} element is $\partial F / \partial v_\theta \big|_{v_\theta = v_{\theta i}}$, $\mathbf{F}_{\theta x}'$ is a vector whose i^{th} element is $\partial F / \partial s_{\theta x} \big|_{s_{\theta x} = s_{\theta x i}}$, and $\mathbf{F}_x'$ is a vector whose i^{th} element is $\partial F / \partial v_x \big|_{v_x = v_{xi}}$.

The Hessian is:

$$\mathbf{H}(\mathbf{x}) = \begin{array}{c} \mathbf{W}_\theta^T diag(\mathbf{F}_{\theta\theta}'')\mathbf{W}_\theta + \mathbf{W}_\theta^T diag(\mathbf{F}_{\theta\theta x}'')\mathbf{W}_{\theta x} + \mathbf{W}_\theta^T diag(\mathbf{F}_{\theta x}'')\mathbf{W}_x \\ + \mathbf{W}_{\theta x}^T diag(\mathbf{F}_{\theta x\theta}'')\mathbf{W}_\theta + \mathbf{W}_{\theta x}^T diag(\mathbf{F}_{\theta x\theta x}'')\mathbf{W}_{\theta x} + \mathbf{W}_{\theta x}^T diag(\mathbf{F}_{\theta xx}'')\mathbf{W}_x \\ + \mathbf{W}_x^T diag(\mathbf{F}_{x\theta}'')\mathbf{W}_\theta + \mathbf{W}_x^T diag(\mathbf{F}_{x\theta x}'')\mathbf{W}_{\theta x} + \mathbf{W}_x^T diag(\mathbf{F}_{xx}'')\mathbf{W}_x \end{array} \quad \text{(C.23)}$$

where $\mathbf{F}_{\theta\theta}''$ is the vector whose i^{th} element is $\partial^2 F / \partial v_\theta^2 \big|_{v_\theta = v_{\theta i}}$, $\mathbf{F}_{\theta x}''$ is the vector whose i^{th} element is $\partial^2 F / \partial v_\theta \partial v_x \big|_{v_\theta = v_{\theta i}, v_x = v_{xi}}$, $\mathbf{F}_{\theta\theta x}''$ is the vector whose i^{th} element is $\partial^2 F / \partial v_\theta \partial s_{\theta x} \big|_{v_\theta = v_{\theta i}, s_{\theta x} = s_{\theta xi}}$, and so on.

Expanding the summed function:

$$F(v_{\theta i}, v_{xi}, s_{\theta xi}) = \left[\ln\left(v_\theta v_x - s_{\theta x}^2\right) + \frac{\theta^2 v_x - 2\theta x s_{\theta x} + x^2 v_\theta}{v_\theta v_x - s_{\theta x}^2} \right]_i \quad \text{(C.24)}$$

Working out the first derivates:

$$\mathbf{F}_\theta'_i = \left\{ -\left(-v_\theta v_x^2 + v_x s_{\theta x}^2 + s_{\theta x}^2 x^2 + \theta^2 v_x^2 - 2\theta x v_x s_{\theta x} \right) / \left(v_\theta v_x - s_{\theta x}^2 \right)^2 \right\}_i \quad \text{(C.25)}$$

$$\mathbf{F}_x'_i = \left\{ -\left(-v_x v_\theta^2 + v_\theta s_{\theta x}^2 + s_{\theta x}^2 \theta^2 + x^2 v_\theta^2 - 2\theta x v_\theta s_{\theta x} \right) / \left(v_\theta v_x - s_{\theta x}^2 \right)^2 \right\}_i \quad \text{(C.26)}$$

$$\mathbf{F}_{\theta x}'_i = \left\{ 2\left(-v_\theta v_x s_{\theta x} + s_{\theta x}^3 + \theta^2 v_x s_{\theta x} - \theta x v_\theta v_x - \theta x s_{\theta x}^2 + x^2 v_\theta s_{\theta x} \right) / \left(v_\theta v_x - s_{\theta x}^2 \right)^2 \right\}_i \quad \text{(C.27)}$$

And the second derivatives:

$$\mathbf{F}_{\theta\theta}''_i = \left\{ -v_x \left(-v_\theta v_x^2 + v_x s_{\theta x}^2 + 2 s_{\theta x}^2 x^2 + 2\theta^2 v_x^2 - 4\theta x v_x s_{\theta x} \right) / \left(v_\theta v_x - s_{\theta x}^2 \right)^3 \right\}_i \quad \text{(C.28)}$$

$$\mathbf{F}_{xx}''_i = \left\{ -v_\theta \left(-v_x v_\theta^2 + v_\theta s_{\theta x}^2 + 2 s_{\theta x}^2 \theta^2 + 2 x^2 v_\theta^2 - 4\theta x v_\theta s_{\theta x} \right) / \left(v_\theta v_x - s_{\theta x}^2 \right)^3 \right\}_i \quad \text{(C.29)}$$

$$\mathbf{F}_{\theta x\theta x}''_i = \left\{ -2 \begin{pmatrix} -v_\theta^2 v_x^2 + s_{\theta x}^4 + 6\theta x v_\theta v_x s_{\theta x} - 2\theta x s_{\theta x}^3 + \theta^2 v_\theta v_x^2 \\ + 3\theta^2 v_x s_{\theta x}^2 + x^2 v_x v_\theta^2 + 3 x^2 v_\theta s_{\theta x}^2 + x^2 v_x v_\theta^2 \end{pmatrix} \Big/ \left(v_\theta v_x - s_{\theta x}^2 \right)^3 \right\}_i \quad \text{(C.30)}$$

$$\mathbf{F}_{x\theta}''_i = \mathbf{F}_{\theta x}''_i = \left\{ -s_{\theta x} \begin{pmatrix} -v_\theta v_x s_{\theta x} + s_{\theta x}^3 + 2\theta^2 v_x s_{\theta x} \\ -2\theta x v_\theta v_x - 2\theta x s_{\theta x}^2 + 2x^2 v_\theta s_{\theta x} \end{pmatrix} \Big/ \left(v_\theta v_x - s_{\theta x}^2\right)^3 \right\}_i \tag{C.31}$$

$$\mathbf{F}_{\theta\theta x}''_i = \mathbf{F}_{\theta x\theta}''_i = \left\{ 2 \begin{pmatrix} -s_{\theta x} v_\theta v_x^2 + v_x s_{\theta x}^3 + x^2 v_\theta v_x s_{\theta x} + x^2 s_{\theta x}^3 \\ -\theta x v_\theta v_x^2 - 3\theta x v_x s_{\theta x}^2 + 2 s_{\theta x} \theta^2 v_x^2 \end{pmatrix} \Big/ \left(v_\theta v_x - s_{\theta x}^2\right)^3 \right\}_i \tag{C.32}$$

$$\mathbf{F}_{x\theta x}''_i = \mathbf{F}_{\theta xx}''_i = \left\{ 2 \begin{pmatrix} -s_{\theta x} v_x v_\theta^2 + v_\theta s_{\theta x}^3 + \theta^2 v_x v_\theta s_{\theta x} + \theta^2 s_{\theta x}^3 \\ -\theta x v_x v_\theta^2 - 3\theta x v_\theta s_{\theta x}^2 + 2 s_{\theta x} x^2 v_\theta^2 \end{pmatrix} \Big/ \left(v_\theta v_x - s_{\theta x}^2\right)^3 \right\}_i \tag{C.33}$$

These results complete the derivation.